Title
Development and Applications of 4D Real-Time Multi-Functional Spectral-Domain Optical Coherence Tomography

Permalink

Author
Wang, Yan

Publication Date
2013

Peer reviewed|Thesis/dissertation

UNIVERSITY OF CALIFORNIA
RIVERSIDE

Development and Applications of 4D Real-Time Multi-Functional Spectral-Domain Optical Coherence Tomography

A Dissertation submitted in partial satisfaction
of the requirements for the degree of

Doctor of Philosophy

in

Bioengineering

by

Yan Wang

June 2013

Dissertation Committee:
  Dr. B. Hyle Park, Chairperson
  Dr. Victor G.J. Rodgers
  Dr. Jiayu Liao

The Dissertation of Yan Wang is approved:

Committee Chairperson

University of California, Riverside

ACKNOWLEDGEMENTS

First and foremost, I would like to express the utmost gratitude to my advisor, Dr. B. Hyle Park, as this thesis work would not have been possible without his endless support and guidance. He has always been available and patient for any questions or problems I have had on research. His constant and steady guidance and support through my PhD research helped me to persevere even when I encountered the occasional and inevitable bottleneck. He constantly motivates me to pursue and achieve a higher degree of performance and it has been a great fortune and a lifetime benefit to have him as my PhD advisor and mentor.

I am sincerely thankful to my dissertation committee members: Dr. Victor G.J. Rodgers for his advice on my research and encouragement to strive for a better performance, and Dr. Jiayu Liao for his great support during my graduate studies and nice jokes every time I meet him. I would also like to sincerely express my acknowledgement to my candidacy committee members: Dr. Jerome Schultz, Dr. Valentine Vullev, Dr. Michael Adams and Dr. Maksim Bazhenov. Their insightful comments and constructive suggestions helped to shape and guide the research presented here.

I am very thankful to my lab members for both their great help with research and for their friendship that made my graduate life colorful. Special thanks go to Christian Oh and Shahidul Islam. I can never forget all the time we spent working together and how they helped make it seem less like work and more just enjoying time together. They helped me out as great lab mates as well as wonderful friends. I would also thank my other lab members Rezuanul Haque, Michael Oliveira, Koji Hirota, Jonathan Ma, Carissa Reynolds, Melissa Eberle, for their many years of assistance on research and warm hearted accompany in the laboratory. Jenny Szu and Mike Hsu from Dr. Devin Binder's lab in the Biomedical Sciences Program are also acknowledged for their assistance on animal protocol amendment and animal training. I would also like to express my acknowledgement to Hong Xu for her help and training on instruments, and both Denise Sanders and Crissy Reissing for their great help during my five-year study.

Last but not least, I am very much indebted to my dad, Zhenxue Wang and my mom ,Derong Li, for their unconditional love and limitless support to the dream I am pursuing. Finally, my boyfriend, Xiaoming Lu, has consistently supported me throughout life and encouraged me on with research.

The text of this dissertation, in part, is a reprint of the material as it appeared in Optics Express 2012, 20(14), page 14797-14813. As listed in the publication, Dr. B. Hyle Park supervised the research, which formed the basis for this dissertation.

Riverside, California, June 2013

Yan Wang

ABSTRACT OF THE DISSERTATION

Development and Applications of 4D Real-Time Multi-Functional Spectral-Domain Optical Coherence Tomography

by

Yan Wang

Doctor of Philosophy, Graduate Program Bioengineering
University of California, Riverside, June 2013
Dr. B. Hyle Park, Chairperson

Optical coherence tomography (OCT) is an optical imaging method based on low-coherence interferometry that is capable of high-resolution cross-sectional imaging of internal microstructure by measuring light backscattered from the sample. OCT has the capacity to perform non-contact *in vivo* imaging and has been applied in medical and scientific fields such as ophthalmology, dermatology, developmental biology, and cardiology. Extensions of OCT such as Doppler OCT and polarization-sensitive OCT (PS-OCT) provide additional information about biological tissues. However, the heavy computational load required to process the acquired data stream creates a limit in realization of real-time OCT. Performing multi-functional OCT imaging demands additional processing for reconstruction of functional images, further increasing the total processing time. Graphics processing unit (GPU) processing has been implemented into MRI, CT and ultrasound as well as intensity-only OCT systems to accelerate image processing using its inherent parallel computation architecture. In this thesis, the development and applications of a GPU accelerated real-time 4D multi-functional SD-OCT system was presented.

Chapter 1 describes the construction and characterization of a multi-functional SD-OCT system at 1300nm. The axial resolution, lateral resolution, imaging depth, signal sensitivity drop-off, spectrometer efficiency, phase noise, system noise, polarization noise, computation of phase retardation, optic axis and diattenuation were characterized. Multiple samples were imaged to demonstrate each imaging facet (intensity, polarization and flow) of the system.

In Chapter 2, GPU was included into the imaging system. CUDA C++ was implemented into the real-time data acquisition and processing program to realize real-time data processing and display. The hybrid GPU-CPU program can process all intensity, polarization and flow images 100 times faster than a comparable previous CPU program. The efficient line processing rate realized was 379kHz for all three image types simultaneously, and represents a computational speed 8 times faster than camera line acquisition rate.

In Chapter 3, volume ray casting using GPU was incorporated into the real-time data acquisition and processing program for real-time volume rendering of all intensity, polarization and flow volume images. Arterial pulsation flow was identified and differentiated from venal flow in flow volume images when imaging mouse femoral artery and vein *in vivo*. The real-time volume images allowed visualization of burn progression in a volume as well as identification of burn injury boundaries in chicken muscle tissue.

The application of PS-OCT for the study of peripheral nerve degeneration and regeneration post crush injury is described in Chapter 4. Results from a preliminary non-longitudinal study showed that axonal birefringence decreased post crush injury and then increased with nerve repair. A longitudinal study was initiated in order to reduce the variation caused by different animals. The facilitated visualization of the real-time 3D volume rendering program was used to rapidly identify the micro-suture markers used to demarcate the wound area in order to minimize operational time while ensuring the imaging region was consistent over repeated imaging sessions.

In Chapter 5, PS-OCT was applied on a study of human skin photo aging as a factor of age, gender. Thirty-seven volunteers were recruited in accordance with an approved protocol for skin imaging on sun exposed area (face) and sun protected area (inner upper arm). The results showed a significantly lower birefringence value in the older age group (>=55 years old) than that of younger age group (18-35 years old). There was no significant difference found between young male and young female as well as old male and old female groups.

Table of Contents

List of Tables

List of Figures

Introduction

Optical coherence tomography (OCT) is an optical imaging method based on low-coherence interferometry that is capable of high-resolution cross-sectional imaging of internal microstructure by measuring light backscattered from the sample [1]. Examination of the resolution and sub-surface penetration depth of various imaging modalities, as illustrated in Figure 1, shows that OCT occupies a gap between more traditional optical imaging methods, such as confocal microscopy, and medical imaging techniques, such as ultrasound and magnetic resonance imaging (MRI). The imaging depth of OCT is typically limited to a few millimeters; OCT cannot visualize structures as large as ultrasound, computed tomography (CT) and MRI. However, its resolution is orders of magnitude better than that of these other technologies [2].

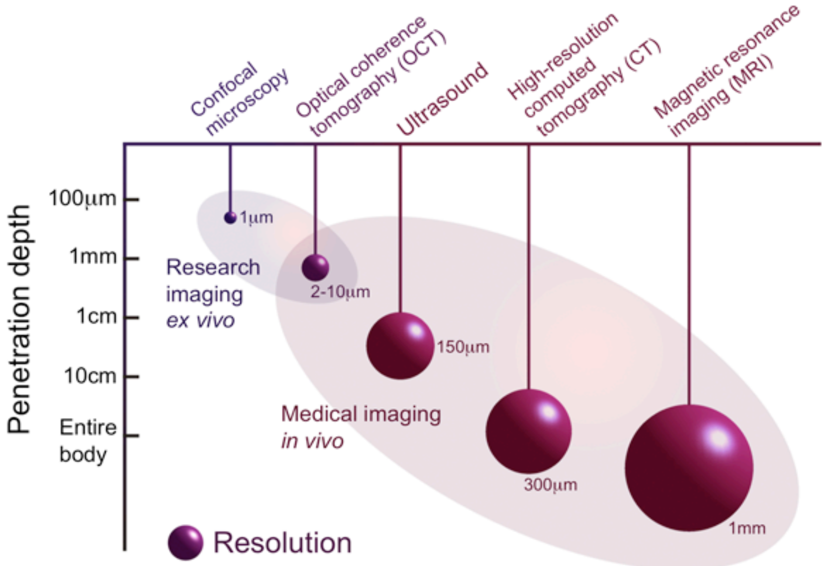

Figure 1. Compare image resolution and penetration depth of OCT with other imaging techniques [2]

Confocal microscopy and two photon microscopy have higher spatial resolution than OCT, however their measurable depth range and working distance is limited [3,4]. The gap between ultrasound and microscopy is filled by OCT, which provides an image axial resolution ranging from 1-15 microns and imaging depth of 2-3mm. It is of great utility that the size and geometry of OCT images are similar to histology images. In addition, it does not require physical contact with the sample, and may be used in air-filled hollow organs (unlike ultrasound). The cost of an OCT system is typically less 100k dollars, which is much less than the million plus cost of an MRI scanner. Furthermore, fiber optic technology has been significantly developed for telecommunication industry. Most optic fibers are manufactured for the three main application windows (850, 1310, 1550nm) to avoid high water absorption. Water is the main component in biological tissue that absorbs light in biological tissue so that it shares the same application windows with telecommunication in near infrared range. This makes it possible to implement fiber optics into OCT system for endoscopic and catheter-based imaging.

Evolution of OCT technology

The first generation of OCT system, termed time-domain OCT (TD-OCT), needs scanning the reference arm to obtain a depth profile [1]. The next generations of Fourier domain OCT (FD-OCT), including spectral-domain OCT (SD-OCT) [5-8] and swept-source OCT (SS-OCT, also known as optical frequency domain imaging) [9], obtain depth profiles by Fourier transform of the interference fringes that are spatially or temporally dispersed in wave number. SD-OCT spatially disperses and resolves the wavelength components of light by using diffraction grating and line scan camera. SS-OCT resolves the wavelength components temporally by using a rapidly tunable laser source. FD-OCT exhibits advantages of an enhanced signal-to-noise ratio (SNR) by dispersing wavelengths, as well as high imaging speed resulted from zero need of scanning reference arm [7].

A number of extensions of OCT have been developed for visualization of features in tissue physiology that are not evident in traditional intensity OCT. Doppler OCT, also named optical Doppler tomography (ODT), combines the Doppler principle with OCT to obtain high-resolution tomographic images of tissue structure and blood flow simultaneously [10-15]. Polarization sensitive OCT (PS-OCT) combines polarization sensitive detection with OCT to determine tissue birefringence [16-19]. These functional extensions of OCT provide clinically important information on tissue physiology, such as tissue blood perfusion, hemodynamics, and structural remodeling [20-24]. In this thesis, we focus on rapid real-time visualization of volumetric renderings of Doppler OCT and PS-OCT with intensity OCT image. The information of blood flow that can be extracted by Doppler OCT is of great interest. In addition, PS-OCT allows evaluation of the tissue birefringence change in the nerve and human skin, which will be discussed in Chapter 4 and Chapter 5. For these reasons, we are specifically interested in building a multi-functional OCT system that incorporates intensity, Doppler OCT and PS-OCT.

Current clinical applications of OCT

OCT has been applied in many fields because of its capacity for non-contact, non-invasive, in-vivo imaging. The main application thus far has been ophthalmology because transparency of the eye minimally attenuates light in the 800nm range. This makes it easy to access to the anterior segment as well as the retina. The first *in vivo* OCT imaging studies of the human retina were presented in 1993 [25]. This was followed by many studies on anterior eye imaging and retinal imaging, and also clinical applications on ophthalmology [26-31]. The first clinical OCT system was reported for ophthalmic use in 1996. The annual revenue on ophthalmology has increased from several million in 1996 to about 350 million dollars in 2012, as shown in Figure 2. [32]

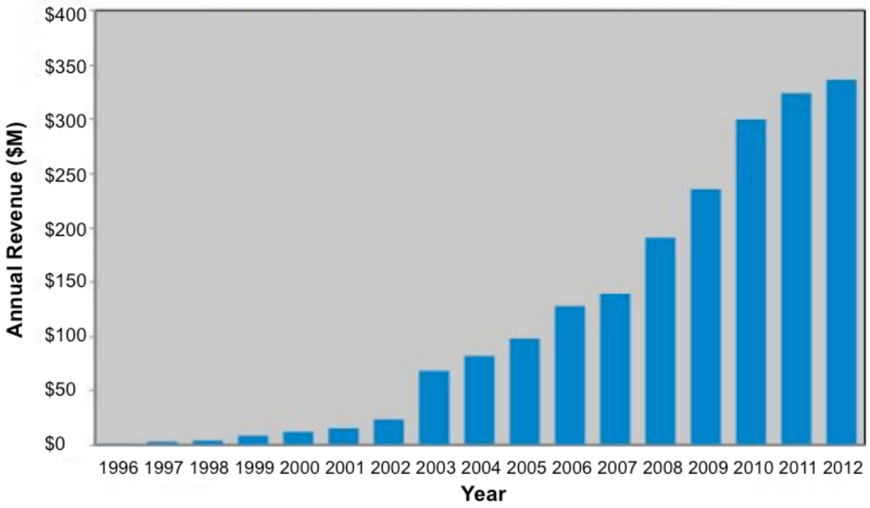

Figure 2. Annual ophthalmic OCT system market [32]

Current OCT technology enables non-transparent soft and hard tissues to be examined *in vivo*. Other applications include tissue engineering, developmental biology, and cardiology. The global optical imaging market valued $915.75 million in the year 2012, and OCT dominates the market with over 70% share. Figure 3 is a breakdown of clinical diagnostics market of OCT in 2012 in US [34]. The application to ophthalmology dominates almost half of the market by amount of funding, with the secondary applications in dentistry and thirdly on dermatology. Ongoing research studies have been investigating the potential application of OCT in neurology and oncology etc.

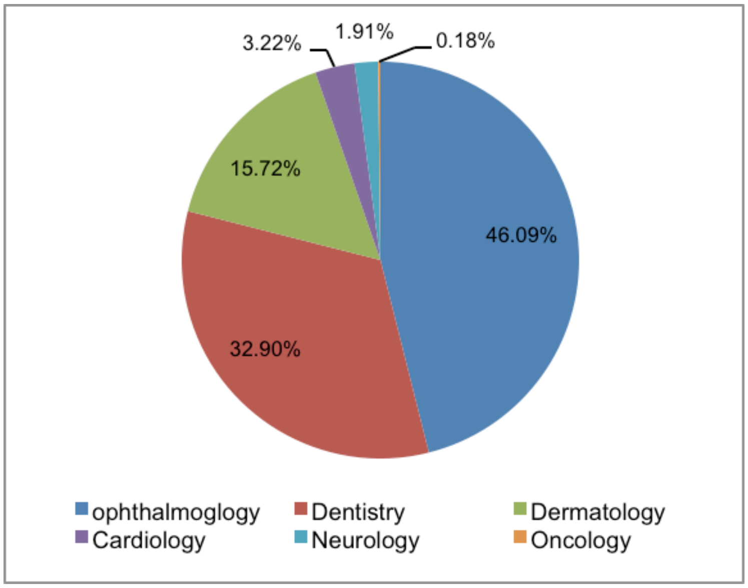

Figure 3. US OCT-clinical diagnostics market in 2012 by applications [33]

OCT from benchside to bedside

Fujimoto et al first published OCT technology in Science in 1991. With more than twenty years of development, OCT technology has been of significant merit in clinical setting. The technology was initially licensed by MIT to Carl Zeiss Meditec

Inc. (Dublin, CA) in 1996 and obtained Federal Drug Administration (FDA) clearance in 2002. Carl Zeiss Meditec has introduced three generations of retinal OCT scanners: OCT1, OCT2 and OCT3 (Stratus), and has sold more than 9000 of its Stratus OCT$^{\text{TM}}$ systems to date. Then Carl Zeiss Meditec introduced CIRRUS$^{\text{TM}}$ HD-OCT in 2007, the first to deliver high-definition 3D maps. OCT has been the only technology that can provide 3D image of eye with such high spatial resolution. There are over 36 OCT system companies in the market today [34].

Image processing and display

The images of the sample can be acquired by real-time processing or post-processing after data acquisition. However, visualization the sample images through post-processing makes it difficult to ensure that the sample is at focus and the region of imaging is of interest. Adjusting the scanning position or sample position by post-processed images not only elongates the whole image session, but also makes the whole procedure more complicated. A real-time data acquisition and processing program can allow visualization of sample images during imaging.

Most OCT systems do lateral point scanning except full field OCT. So the acquisition speed of an OCT system is best described by its maximum depth profile acquisition rate. The second generation of OCT, FD-OCT, is much faster than TD-OCT in terms of data acquisition [6]. A SS-OCT system acquisition speed is decided by laser light source sweeping speed [9]. A SD-OCT system acquisition speed is dependent on the line scan camera speed [7]. The data processing speed is usually dependent on CPU, which has limiting number of cores for data processing.

The slow image processing speed comparing to the relative faster acquisition speed creates a limit of real-time processing and displaying acquired data. This can slow down the overall image acquisition and display speed. Or processing part of the acquired data can cause missing information in the real-time display. For example, Carl Zeiss Meditech CIRRUS^{TM} HD-OCT 5000 is capable of acquiring data at line rate of 68kHz, while its processing speed is only at 25.6kHz. Thorlabs Hyperion can acquire data as fast as 110kHz. However, its data processing speed is only 28kHz. Bioptigen R2200,R2300, C2200, C2300 can acquire and display at 32kHz for 1024 pixel camera. The processing speed for 2048 pixel camera is only 20kHz for data acquisition speed of 70kHz. Survey results from many other companies show a line acquisition speed of 20kHz-53kHz, similarly, image process speed is either slower than acquisition speed or not stated.

This is a common issue in OCT systems developed for research too. There is good amount of journal papers publishing their work of accelerating the image processing in the real-time acquisition and processing program by either using field programmable gate array (FPGA) [35-38] or more widely by graphics processing unit (GPU) [39-43].

Development of real-time multi-functional SD-OCT system

The first multi-functional TD-OCT system that could simultaneously provide intensity, polarization and flow images was demonstrated by Pierce et al in 2002, the images were processed in post imaging session [44]. Park et al published the first demonstration of real-time acquisition, processing, and display of multi-functional TD-OCT systems in 2003 [45]. The data acquisition speed was 2048 A-scans/second limited by scanning of reference arm. The image update rate was 0.75 frame/second. A SD-OCT system uses a spectrometer to resolve different wavelengths and line scan camera to receive dispersing light. This does not require scanning of reference arm, thus largely increases data acquisition speed. The acquisition rate was 18kHz in the multi-functional SD-OCT system reported by Part et al in 2005. The multi-functional images update rate was 2-5 frames/second [46].

Most of the commercial systems provide intensity image only. Thorlabs incorporated Doppler computation in their CALLISTO systems. The only commercial PS-OCT system is Thorlabs PS-OCT module that is to be add-on for its 1300nm SS-OCT system. The development of a multi-functional OCT system not only requires additional hardware to be added in the system such as one more camera, a polarization modulator, polarization beam splitters etc [46]. The complexity in image processing also requires more technology. The additional requirements on the hardware and software bring extra cost on hardware as well as labor work. Lacking of available commercial multi-functional SD-OCT system motivates us to build a homemade system. The slow data processing speed in almost all OCT systems triggered us on development of real-time multi-functional SD-OCT system. As the powerful capability of 3D volume rendering to visualize volume image, this enables visualization of 3D information that not directly viewing from 2D images. Real-time volume rendering is described in Chapter 3, which is capable of providing volume change in a real-time manner.

Thesis structure

There are five chapters in this thesis, the first three chapters describe the hardware and software work of developing the real-time 4-dimensional multi-functional SD-OCT system, and last two chapters are the applications of using this system on neurology and dermatology. In chapter 1, the construction, calibration and characterization of the multi-functional OCT system was described. In Chapter 2, GPU computation was incorporated into the real-time data acquisition and processing program that accelerated the data processing and realized real-time image processing. In Chapter 3, real-time volume rendering was included into the program so that volume images were rendered and displayed in real-time manner. In Chapter 4, PS-OCT was applied on evaluation of peripheral nerve injury studies, a non-longitudinal study data was re-analyzed and a longitudinal study was initiated. Chapter 5 described using this system for a human skin photo aging study.

Chapter 1: Construction and characterization of a multi-functional spectral-domain optical coherence tomography system

Abstract

A multi-functional OCT system that incorporates Doppler OCT and PS-OCT allows simultaneous visualization of tissue structure, flow and birefringence from the same imaging sample. A multi-functional SD-OCT system at 1300nm was constructed and characterized. The spectrometer was calibrated using a cover slip to induce known phase modulation to the light that was received by the cameras. The system axial resolution, lateral resolution, imaging depth, spectrometer quantum efficiency, signal sensitivity drop-off and noise analysis were characterized. The computation of phase retardation, optic axis and diattenuation was characterized with imaging a quarter wave plate and polarizing films. Multiple samples were imaged using the system to get every facet of the image (intensity, flow and polarization). Then a mouse hind leg on the femoral region was imaged, the femoral artery, vein and nerve were identified in the intensity, flow and polarization images.

Introduction

Optical coherence tomography (OCT) is an optical imaging method based on low-coherence interferometry, which allows measurement of the magnitude and echo time delay of backscattered light. It has high sensitivity as the light scattered from the sample is amplified by the light from the reference arm. Light from the source can be expressed by electric field $E(\omega,t)$ as a complex exponential [47]:

$$E(\omega,t) = s(\omega)\exp\left[-i(\omega t + kz)\right] \tag{1}$$

where $s(\omega)$ is source field amplitude spectrum, ω is the frequency, t is time, k is wavenumber, and z is the optical distance along the propagation direction. The part in the square bracket simply accounts for phase accumulated throughout the interferometer. The input phase is arbitrary. The interferometer measures the relative output phase between the two optical paths. Thus the phase term can be dropped from the input electric field.

As shown in Figure 4, the light source is divided into reference $E_r(\omega,t)$ and sample beam $E_s(\omega,t)$. These two beams interfere and generate interference fringes. A detector measures the intensity of the output, which is proportional to the square of the total field [47]:

$$I(\omega,\Delta z) \sim \left|E_r(\omega,t)\right|^2 + \left|E_s(\omega,t)\right|^2 + 2E_r(\omega,t)E_s(\omega,t)\cos(2k\Delta L) \tag{2}$$

ΔL is the path length difference between the sample and reference arms of the interferometer. $\Delta L = \Delta t \cdot v$, where v is light speed in air, Δt is time difference traveling between two beams. The interference fringes will be generated as a function of time while scanning the reference path. The different wavelengths of light ($\lambda = 2\pi v / \omega$) are not resolved thus detected intensity is the sum of light from all wavelengths.

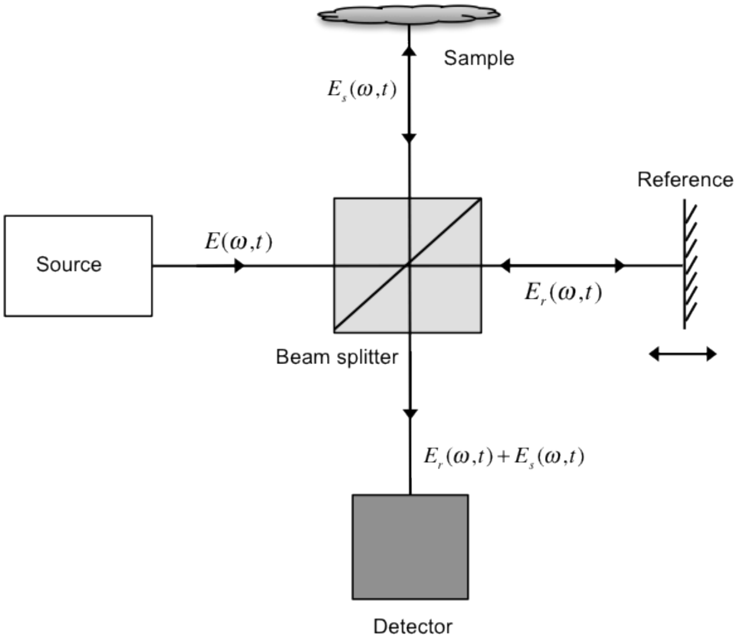

Figure 4. Diagram of time-domain OCT: source light is split into reference arm and sample arm. The combined reflected light from both arms generates fringes to be detected by a detector. [47]

The first generation of OCT, time-domain OCT system (Figure 4) requires scanning of reference arm to get one depth profile. By scanning the reference arm, the magnitude and echo time delay of light can be measured. A depth profile can be obtained by demodulating the interference signal at different depths. A time-domain OCT system detects the sum of all the wavelengths so that it does not resolve wavelengths.

The second-generation system, Fourier domain OCT (FD-OCT) including swept source type and spectral-domain [5-9], has the advantage that obtaining an axial scan does not need to move reference arm. FD-OCT allows for increases in both line acquisition rate and sensitivity by several orders of magnitude compared to their time-domain counterparts [7]. The depth profile of the sample structure is then obtained from Fourier transform. The detected intensity spectrum is [48]:

$$I(k) = I_r(k) + 2\sqrt{I_s(k)I_r(k)}\sum_n \alpha_n \cos(kz_n) + I_s(k) \tag{3}$$

where $I_r(k)$ and $I_s(k)$ are the wavelength-dependent intensities reflected from the reference and sample arms, respectively. k is the wave number, α_n is the square root of the sample reflectivity at depth z_n. Depth information is retrieved by performing Fourier transform of above equation, which yields the following convolution [48]:

$$\left|FT\left[I(k)\right]\right|^2 = \left\{\delta(0) + \sum_n \alpha_n^2 \delta(z - z_n) + \sum_n \alpha_n^2 \delta(z + z_n) + O\left[I_s^2 / I_r^2\right]\right\} \tag{4}$$

where $\delta(0)$ is the autocorrelation signal from the reference arm. The second and third terms in the braces are interference between light returning from reference and sample arms that form two images. The final term has magnitude on the order of I_s^2 / I_r^2, describing autocorrelation noise due to interference within the sample arm.

Doppler OCT

Doppler optical coherence tomography (DOCT), also called as optical Doppler tomography (ODT), is a combination of OCT and laser Doppler flowmetry [12].

Doppler OCT combines the Doppler principle with OCT to obtain high-resolution tomographic images of simultaneous tissue structure and blood flow [13-15]. The flow information was computed based on the Doppler effect in which the detected frequency of a wave changes for an observer moving relative to its source.

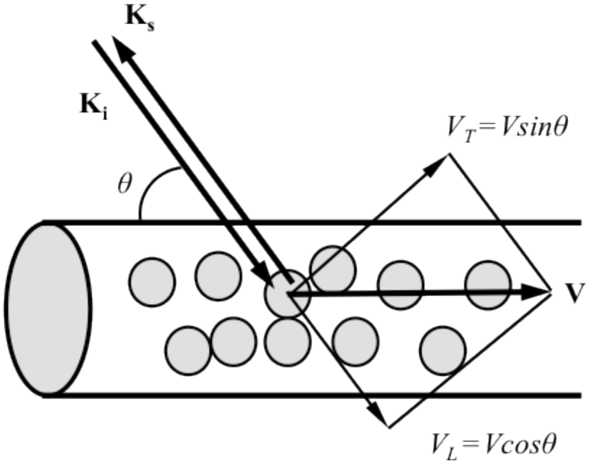

Figure 5. Illustration of Doppler flow [12]

Figure 5 is an illustration of Doppler flow with fluid flow velocity of **V**. The light backscattered from a moving particle interferes with the reference beam. The Doppler frequency shift f_D occurs in the interference fringes is $f_D = (\vec{k}_s - \vec{k}_i) \cdot \vec{v} / 2\pi$. Here $\vec{k}_i$ is the incoming light wave vector and $\vec{k}_s$ is the scattered light wave vector, and $\vec{v}$ is the velocity vector of the moving particle. If the angle between particle flow direction and sample beam is θ, the Doppler shift is thus $f_D = 2V_D n \cos\theta / \lambda_0$. λ_0 is the vacuum center wavelength of the light source, n is the refractive index in tissue, V_D is the flow fluid velocity.

The minimum detectable Doppler frequency shift (Δf_D) varies inversely with short-time Fourier transform window size (Δt_p) at each pixel ($\Delta f_D \approx 1/\Delta t_p$). A large pixel time-window size ($\Delta x_p = V\Delta t_p$) increases velocity sensitivity while decreases spatial resolution. Increasing the image frame rate also decreases velocity sensitivity.

Phase-resolved Doppler OCT overcomes the trade-off between velocity sensitivity and imaging speed by using the phase change between sequential scans to construct flow velocity images [49-50]. The phase information of the fringe signal can be determined from the complex analytical signal after Hilbert transform. In an SD-OCT system, the phase information of the complex signal is directly obtained after Fourier transform of the acquired interference spectrum. The flow information can be extracted by calculating the phase difference between two successive complex depth profiles. The relationship between fluid flow velocity V and phase difference $\Delta\phi$ is [49]:

$$V = \frac{\Delta\phi}{4\pi\cos\theta}\frac{\lambda_0}{T} \tag{5}$$

where T is the time period between two successive A-scans. The minimum detectable flow velocity is decided by the phase noise ($\Delta\phi$) of the system, light center wavelength (λ_0), angle between the light beam and fluid flow direction (θ), and time between successive A-scans (T). Doppler OCT has been applied on multiple situations, including but not limited to *in vivo* blood flow in retina and skin, drug delivery, developmental biology, cardiology etc [10-15, 49-50].

Polarization-sensitive OCT

PS-OCT uses depth-dependent polarization states to determine tissue properties that are not easily discernible using other existing optical diagnostics [18-19]. The main one of these that occurs in biological tissues is birefringence. Birefringence is the optical property that the refractive indices are different along the two orthogonal polarization components of light. As shown in Figure 6, the two polarization components of light propagate at different speed in a birefringent material caused by difference in refractive indices. Thus a phase retardation is generated between the two polarization states. The well-organized layered fibrous tissue exhibits birefringence, such as muscle, tendons, nerve, bone, cartilage, teeth etc [18].

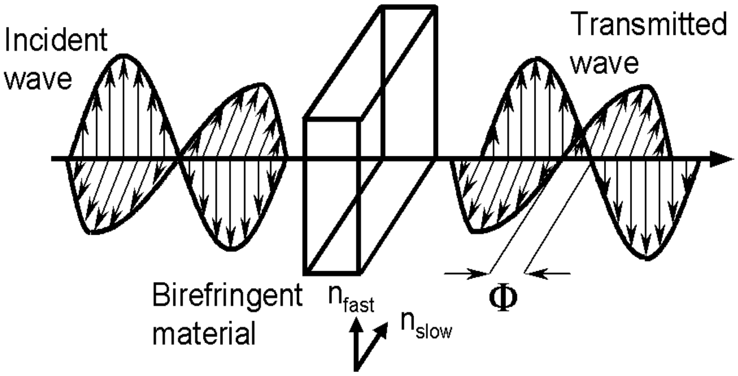

Figure 6. Birefringent material causes phase retardation to two orthogonal polarization states of light [51]

If the difference in refractive index is Δn, and the distance of light passing through the material is x, then the two beams will experience a cumulative phase retardation of [51]:

$$\eta = \frac{2\pi \Delta n x}{\lambda} \qquad (6)$$

In a bulk optics based PS-OCT system, the light polarization state onto the sample is known. By measuring the output polarization state of light back scattered from the sample, the sample phase retardation can be calculated [52-54]. In a fiber-based PS-OCT system, optic fibers cause unknown amount of birefringence resulting from manufacturing imperfection, mechanical bending, twisting or lateral pressure. This causes an unknown light polarization states incident onto the sample. Besides, the amount of phase retardation cannot be calculated when a linear incident polarized light has coincident optic axis with that of sample. Alternating the incident light between two orthogonal polarization states on a Poincare sphere representation would not only increase known terms for calculation. This also ensures that sample phase retardation can still be calculated from another polarization state if one linear polarized light has same optic axis with sample [45,55-57]. PS-OCT has been used in a wide variety of applications, including correlating burn depth with a decrease in birefringence [57-58], measuring the birefringence of the retinal nerve fiber layer [59-61], monitoring the onset and progression of caries lesions [62], and imaging dental structure etc [63].

A multi-functional OCT system that incorporates intensity, flow and polarization images can provide complementary information [44-46, 64]. Figure 7 is one example of multi-functional OCT images of a human fingertip [46]. The stratum corneum and granulosum were visible in the intensity image (top left). Venal flow was observed in the phase variance (top right) and bi-directional flow (bottom right) images. The derma-epidermal junction and the dermal papillae were visible in the phase retardation image (bottom left). The additional contrast information provided by a multi-functional SD-OCT system motivated the work described in this Chapter.

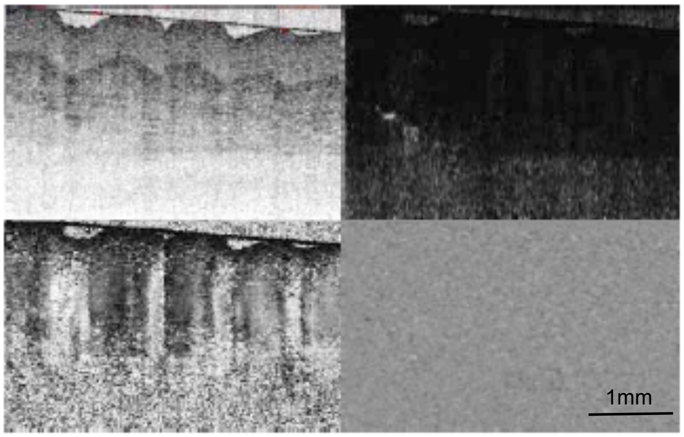

Figure 7. Multi-functional OCT images of a human fingertip [46]

Materials and Methods

A schematic of the multi-functional SD-OCT system is shown in Figure 8. The broadband light source is composed of two fiber-based super-luminescent diodes (SLD), one centered at 1295nm with a full-width at half maximum (FWHM) bandwith of 97nm (Thorlabs Inc.) and the other centered at 1350nm with a FWHM bandwidth of 48nm (Denselight Semiconductors Pte Ltd). The resulting source is centered at 1298nm with a 120 nm FWHM bandwidth and 16mW power. Light from the source is collimated and passes through a polarization beam splitter (pbs) and a polarization modulator (pm, Thorlabs Inc.).

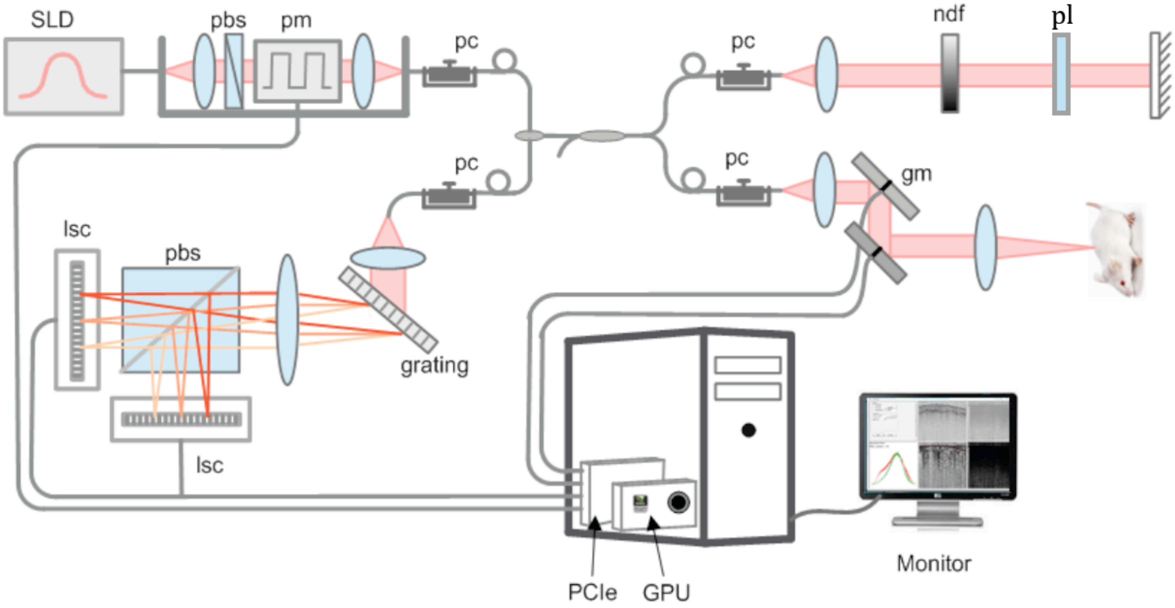

Figure 8. Schematic of multi-functional SD-OCT system [65]

The polarization modulator changes the light polarization states by changing the voltage applied on the LiNb crystal inside the box. This toggles the light between two orthogonal polarization states in a Poincare sphere representation. The polarized light is sent to a fiber circulator (Thorlabs Inc.) and an 80/20 fiber splitter (AC Photonics Inc) with a polarization controller (pc). In the reference arm, a neutral density filter (ndf) is used to adjust light reflecting from reference mirror, and a polarizer (pl) is used to insure uniformity of the reference polarization state. In the sample arm, galvanometer mounted mirrors in the hand-piece provide transverse scanning of a 10 micron diameter focused spot. Light from both arms is recombined at the splitter and passes through a transmission diffraction grating (1145 lines per mm, Wasatch Photonics) before being focused by a planoconvex lens. A polarization beam splitter is used to separate the two polarization states of light. Additional polarizers are added on the polarization beam splitter to increase the extinction ratio. The two polarization states are collected by two line scanning cameras (lsc, Goodrich SUI SU-LDH linear digital high speed InGaAs camera) separately with readout rates up to 46 kHz, which were fastest line scan cameras at 1300nm range when we started working on the system in the year of 2009. Output from the two cameras is digitized through two National Instruments boards (PCIe NI-1429). The synchronized trigger signals were sent via two BNC boards (BNC 2110 and 2120) and one data acquisition card (National Instrument PCIe 6259) to the two cameras, two-axis scanner, and the polarization modulator.

Computation of intensity

Different wavelengths of light in the spectrometer were spatially separated by the grating and then received by different pixels of the cameras. Calibrating the spectrum on each camera is critical in SD-OCT systems for intensity image processing. This is even more so for accurate calculation of phase retardation in PS-OCT. The initial wavelength assignments on the cameras were calculated from the spectrometer [46]. Next, a correction was applied on the initial guess by introducing a known modulation on the spectrum using a coverslip. Thus the calibrated wavelength assignments on the cameras were obtained. This will be discussed more in detail in the results section of this chapter. Raw data reading from the cameras was resampled uniformly in k-space using the calibrated wavelengths. A depth profile was obtained after a fast Fourier transform (FFT) of the spectrum. The combination of the two polarization channels, $H_n(z_m)$ and $V_n(z_m)$, contributed to the intensity image. H and V distinguish depth profiles from the two cameras respectively, n is the depth profile number, z is the depth into the tissue and m is the pixel number in the depth profile. The intensity was computed as [46]

$$I_n(z_m) = H_n(z_m) \cdot H_n^*(z_m) + V_n(z_m) \cdot V_n^*(z_m) \tag{7}$$

where * represents the complex conjugate. Then the intensity values were converted into logarithmic scale to compress the signal range. Finally, the image is displayed in gray scale.

Computation of flow

The flow information in SD-OCT system can be easily obtained by calculating the phase difference of two neighboring complex depth profiles after Fourier transform. Two kinds of flow information can be obtained, bi-directional flow and phase variance flow. Bi-directional flow was calculated as the weighted phase difference of two successive depth profiles at corresponding depths. Phase variance was calculated as the weighted square of this phase difference. Since there were two polarization states alternating in the source for neighboring depth profiles that causes different phase between two polarization states. Thus the phase difference at depth z_m was calculated as phase difference between A-lines having the same incident polarization state:

$$\Delta\phi_{H_n,V_n}(z_m) = \phi_{H_n,V_n}(z_m) - \phi_{H_{n-2},V_{n-2}}(z_m) \tag{8}$$

An averaged phase difference offset within one phase difference depth profile was calculated. This was subtracted from phase difference depth profile to remove the overall phase shift between depth profiles. The phase differences of the last two depth profiles were assumed to be zero. Bi-directional flow and phase variance flow are expressed as Eq. (9) and Eq. (10), respectively [46]:

$$\omega_n(z_m) = \frac{\left|H_n(z_m)\right|^2 \Delta\phi_{H_n}(z_m) + \left|V_n(z_m)\right|^2 \Delta\phi_{V_n}(z_m)}{\left|H_n(z_m)\right|^2 + \left|V_n(z_m)\right|^2} \tag{9}$$

$$\sigma_n^2(z_m) = \frac{\left|H_n(z_m)\right|^2 \Delta\phi^2{}_{H_n}(z_m) + \left|V_n(z_m)\right|^2 \Delta\phi^2{}_{V_n}(z_m)}{\left|H_n(z_m)\right|^2 + \left|V_n(z_m)\right|^2} \tag{10}$$

The measurement range of bi-directional flow is $-\pi$ to π, that indicates the relative flow direction from positive or negative flow values. Phase variance further strengthens the flow signal by calculating the square of phase difference, resulting in measured signal range of 0 to π^2. Thus phase variance flow image does not provide directionality information. Either bi-directional flow or phase variance, or both can be computed for flow images.

Computation of phase retardation

Two solutions of computing phase retardation from a fiber-based PS-OCT system are introduced as following. They are simplified Stokes vector-based method and Jones matrix-based method.

(a) Stokes vector based method

Phase retardation was calculated using the Stokes vector based method in the real-time processing program due to its relatively low computational load [46]. Stokes vectors, $S_n(z_m)$, were calculated from complex depth profiles after FFT, $H_n(z_m)$, $V_n(z_m)$, such that

$$\mathbf{S}_n(z_m)=\begin{bmatrix} Q_n(z_m) \\ U_n(z_m) \\ V_n(z_m) \end{bmatrix}=\begin{bmatrix} H_n(z_m)\cdot H_n^*(z_m)-V_n(z_m)\cdot V_n^*(z_m) \\ H_n(z_m)\cdot V_n^*(z_m)+H_n^*(z_m)\cdot V_n(z_m) \\ i(H_n(z_m)\cdot V_n^*(z_m)-H_n^*(z_m)\cdot V_n(z_m)) \end{bmatrix} \tag{11}$$

The position of the sample surface within each depth profile, s_n, was determined by thresholding the intensity depth profile. The cumulative sample relative optic axis, A_i, that simultaneously rotates a pair of surface polarization states to states at a particular depth, was determined by

$$\mathrm{A}_i(z_m)\,\|\,(\mathbf{S}_{2i}(s_{2i})-\mathbf{S}_{2i}(z_m))\times(\mathbf{S}_{2i+1}(s_{2i+1})-\mathbf{S}_{2i+1}(z_m)) \tag{12}$$

The phase retardation angle was calculated by the rotation angle from surface state to state at specific depth, which was given by

$$\theta_{2i}(z_m) = \cos^{-1}\left(\frac{\left|(\mathrm{A}_i(z_m)\times\mathbf{S}_{2i}(s_{2i}))\cdot(\mathrm{A}_i(z_m)\times\mathbf{S}_{2i}(z_m))\right|}{\left|(\mathrm{A}_i(z_m)\times\mathbf{S}_{2i}(s_{2i}))\right|\left|\mathrm{A}_i(z_m)\times\mathbf{S}_{2i}(z_m)\right|}\right) \tag{13}$$

$\theta_{2i+1}(z_m)$ can be obtained similarly. The overall phase retardation angle is calculated through a weighted average based on the intensities of the polarization states. Moreover, the effect of noise on the value of $\theta_{2i+1}(z_m)$ increases as the angle between the rotation axis $A_i(z_m)$ and either Stokes states $S_i(s_{2i})$ or $S_i(z_m)$ decreases. The angle between $A_i(z_m)$ and $S_i(s_{2i})$ can be calculated from:

$$\sin\theta_{\mathrm{A}_i(z_m),\mathbf{S}_{2i}(s_{2i})} = \frac{\left|\mathrm{A}_i(z_m)\times\mathbf{S}_{2i}(s_{2i})\right|}{\left|\mathrm{A}_i(z_m)\right|\left|\mathbf{S}_{2i}(s_{2i})\right|} \tag{14}$$

The angles between $A_i(z_m)$ with $S_{2i+1}(s_{2i+1})$ and $S_{2i+1}(z_m)$ can be calculated similarly. The overall weight factor can be determined as the product of the sines of the angles between the axis of rotation and the polarization states, which are:

$$W_{2i}(z_m) = I_{2i}(s_{2i})\sin\theta_{\mathrm{A}_i(z_m),\mathbf{S}_{2i}(s_{2i})} I_{2i}(z_m)\sin\theta_{\mathrm{A}_i(z_m),\mathbf{S}_{2i}(z_m)} \tag{15}$$

$$W_{2i+1}(z_m) = I_{2i+1}(s_{2i+1})\sin\theta_{\mathrm{A}_i(z_m),\mathbf{S}_{2i+1}(s_{2i+1})} I_{2i+1}(z_m)\sin\theta_{\mathrm{A}_i(z_m),\mathbf{S}_{2i+1}(z_m)} \tag{16}$$

The overall weighted averaged phase retardation angle was determined as:

$$\eta_i(z_m) = \frac{W_{2i}(z_m)\theta_{2i}(z_m) + W_{2i+1}(z_m)\theta_{2i+1}(z_m)}{W_{2i}(z_m) + W_{2i+1}(z_m)} \tag{17}$$

(b) Jones matrix-based method

Jones matrix-based approach has the advantage of determining relative optic axis, phase retardation, and diattenuation simultaneously for fiber-based PS-OCT [55]. The incident electric field can be expressed as:

$$\mathbf{E} = \begin{bmatrix} E_{\parallel} \\ E_{\perp} \end{bmatrix} \tag{18}$$

Optical elements can be expressed by Jones matrices. Transmitted polarization state of light can be expressed by a Jones matrix J acting on an incident polarization state $\mathbf{E}$.

$$\mathbf{E}' = \begin{bmatrix} E'_{\parallel} \\ E'_{\perp} \end{bmatrix} = e^{i\psi} \begin{bmatrix} J_{11} & J_{12} \\ J_{21} & J_{22} \end{bmatrix} \begin{bmatrix} E_{\parallel} \\ E_{\perp} \end{bmatrix} = e^{i\psi} \mathbf{J}\mathbf{E} \tag{19}$$

where ψ is some arbitrary phase. When there are several optical elements in the system, the overall Jones matrix is: $\mathbf{J} = \mathbf{J_n} \cdots \mathbf{J_2}\mathbf{J_1}$.

The Jonex matrix for a birefringent material that induces a phase retardation η between electric field components parallel and orthogonal to a polarization state characterized by an orientation angle θ and a circularity ϕ related to is given by:

$$\mathbf{J}_b = \begin{bmatrix} e^{i\eta/2}C_\theta^2 + e^{-i\eta/2}S_\theta^2 & (e^{i\eta/2} - e^{-i\eta/2})C_\theta S_\theta e^{-i\phi} \\ (e^{i\eta/2} - e^{-i\eta/2})C_\theta S_\theta e^{i\phi} & e^{i\eta/2}S_\theta^2 + e^{-i\eta/2}C_\theta^2 \end{bmatrix} \tag{20}$$

where $C_\theta = \cos\theta$ and $S_\theta = \sin\theta$. The Jones matrix of a dichroic material with attenuation ratios of P_1 and P_2 for electric field components parallel and orthogonal, respectively, to a polarization state given by an orientation angle Θ and Φ has the form:

$$\mathbf{J}_d = \begin{bmatrix} P_1 C_\Theta^2 + P_2 S_\Theta^2 & (P_1 - P_2) C_\Theta S_\Theta e^{-i\Phi} \\ (P_1 - P_2) C_\Theta S_\Theta e^{i\Phi} & P_1 S_\Theta^2 + P_2 C_\Theta^2 \end{bmatrix} \tag{21}$$

In the PS-OCT system, J_{in} is defined as the Jones matrix representing the optical path from the polarized light source to the sample surface, J_{out} as that going from the sample surface to the detectors, and J_s as the round-trip Jones matrix for light propagation through a sample. The electric field of light coming back from some depth within the tissue can be expressed as:

$$\mathbf{E}' = e^{i\Delta\psi} J_{out} J_S J_{in} \mathbf{E} = e^{i\Delta\psi} J_T \mathbf{E} \tag{22}$$

where $\mathbf{E}$ is the electric field of light coming back from sample surface. After more calculation, we can get one expression for J_T:

$$\begin{aligned} e^{i\Delta\psi_1} \begin{bmatrix} P_1 e^{i\eta/2} & 0 \\ 0 & P_2 e^{-i\eta/2} \end{bmatrix} &= \begin{bmatrix} C_\theta & S_\theta \\ -S_\theta & C_\theta \end{bmatrix} \begin{bmatrix} e^{-i\phi} & 0 \\ 0 & e^{i\phi} \end{bmatrix} \begin{bmatrix} H_1' & H_2' \\ V_1' & V_2' \end{bmatrix} \\ &\times \begin{bmatrix} H_1 & e^{i\alpha} H_2 \\ V_1 & e^{i\alpha} V_2 \end{bmatrix}^{-1} \begin{bmatrix} e^{i\phi} & 0 \\ 0 & e^{-i\phi} \end{bmatrix} \begin{bmatrix} C_\theta & -S_\theta \\ S_\theta & C_\theta \end{bmatrix} \end{aligned} \tag{23}$$

here, η is the birefringence. In principle, the parameters θ, ϕ, and α can be solved for the condition that the off-diagonal elements of the matrix product on the right side of equation are equal to zero. In practice, the parameters are optimized to minimize the sum of the magnitudes of the off-diagonal elements because of noise. η can be easily extracted from the phase difference between the resulting diagonal elements. With Jones matrix based method, another light polarization property called diattenuation can be also calculated by $d = (P_1^2 - P_2^2)/(P_1^2 + P_2^2)$. Diattenuation is the property that the two polarization components of light attenuate with different ratio.

Jones matrix method allows simultaneous measurement of optic axis, phase retardation, and diattenuation. This will be demonstrated by imaging a combined wave plate and polarizing film sample in Results section in this chapter. Simplified Stokes vector method assumes no sample diattenuation thus it only computes the optic axis and phase retardation. This assumption is reasonable as the diattenuation was measured less than one tenth of phase retardation in biological tissue [51]. Stokes vector based method is less computationally intensive thus was used in the real-time program for fast computation.

Results

Calibration of cameras

In SD-OCT system, the depth profile (A-line) is obtained by Fourier transform of the interference spectrum as measured by a spectrometer. Fourier transformation relates the physical distance (z) with the wave number ($k = 2\pi / \lambda$). A proper depth profile can be obtained only after accurate assessment of the wavelength corresponding to each spectral element for both cameras. Incorrect wavelength mapping generates a depth-dependent broadening of the coherent peak similar in appearance to dispersion in structural OCT images.

The calibration can be done by using a cover slip to induce a known phase modulation to the spectrum [61]. The light transmitting directly through the glass and the light double reflected first and then pass through the glass generate interference. This introduces extra modulation in terms of $\cos(2dnk)$ on the spectrum, where n is refractive index of the glass and d is the thickness of the coverslip. After Fourier transforming of the spectrum obtained, the peak generated by the coverslip is cut out using a band pass filter in k-space. The phase of the modulation caused by the coverslip should be linear to wavenumber k for perfect sinusoid. So the criterion of proper wavelength arrangement is minimization of the nonlinearity of the phase. Based on geometric optics as shown in Figure 9, an initial guess of the interpolation can be made as [46]:

$$\lambda_j = d\left[\sin\theta_i + \sin\left(\sin^{-1}\left(\frac{\lambda_c}{d} - \sin\theta_i\right) + \tan^{-1}\left(\frac{w \cdot j - x_c}{F}\right)\right)\right] \tag{24}$$

where d is groove spacing of the grating, x_c is the distance from the first pixel to the position of center wavelength, F is focal length of the lens, θ_i is the incident angle on the grating, θ_c is transmitted angle for center wavelength, w is the pixel width.

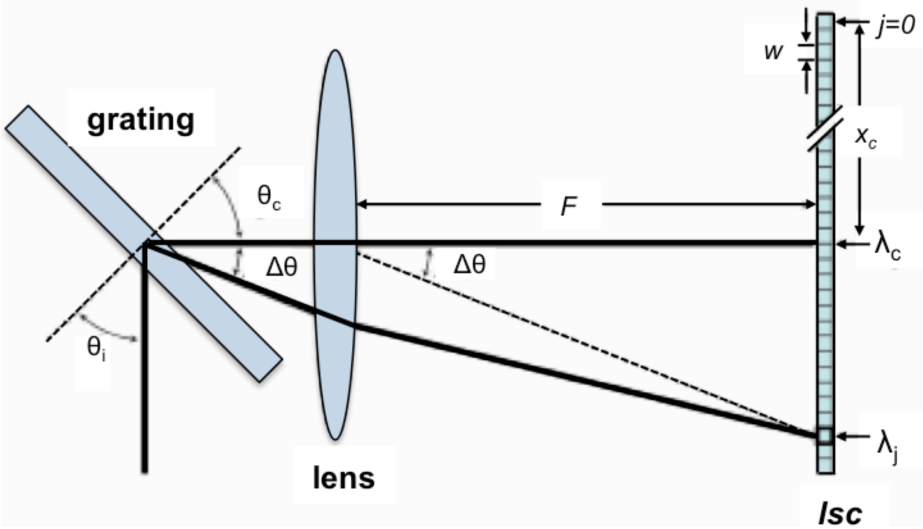

Figure 9. Diagram of light propagation through grating and les onto the line scan camera (lsc) [46]

Eq. (24) is initially used to interpolate the spectral interference fringes to equally spaced k values. Zero-padding is used to improve the interpolation process. The signal peak generated by cover slip is cut out using a band pass filter after obtaining the depth profile post Fourier transform. The signal peak is then converted into k-space by inverse Fourier transform. The phase of k-space interpolated spectrum was fit with first-order polynomial fit. The nonlinear error between the interpolated spectrum and the fit spectrum was calculated as $\sigma(k)$. The new wavenumber array k' is corrected by $k' = k + \sigma(k)/z(peak)$, where

$z(peak) = 2\pi Peak\_index(k_{\max} - k_{\min})$. $Peak\_index$ is the pixel number position corresponding to maximum value of signal peak by cover slip. The correction is applied iteratively till the phase nonlinearity is under the error tolerance of 0.0002. Wavelength array is finally resulted from $\lambda' = 2\pi / k'$.

After calibration, the wavelength is properly arranged on each pixel. The signal peak (indicated by arrow) becomes higher and sharper with better axial resolution, which is shown in Figure 10.

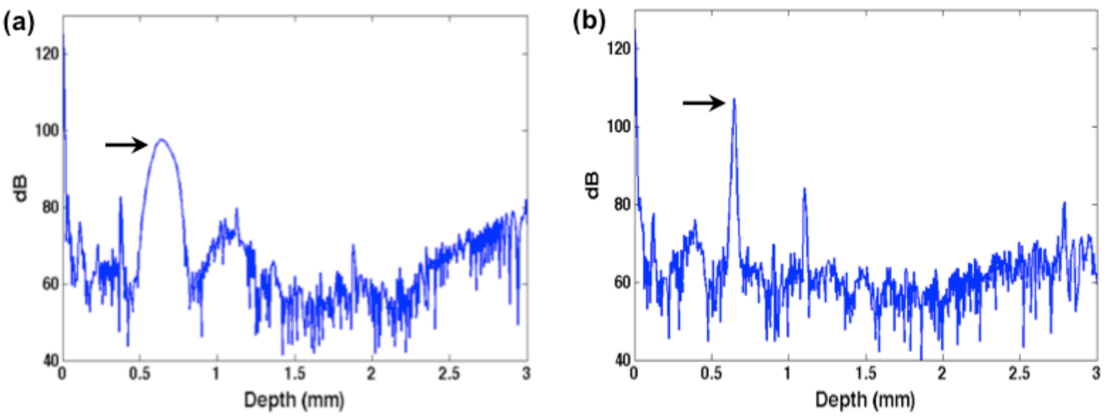

Figure 10. Signal peak of imaging a mirror (a) before and (b) after applying the calibration

The same method was applied to initial calibration of both cameras. In order to get correct PS-OCT images, there is one additional necessary step. The two cameras need to be aligned with each other so that these two cameras have exactly same imaging depths. Misalignment or inaccurate calibration can cause artificial birefringence. A mirror was imaged as the sample, the imaging depths of both cameras were ensured the same while moving sample from surface to depth of 2.5 mm.

System characterization

The system axial resolution, lateral resolution, imaging depth, SNR, sensitivity drop-off, spectrometer quantum efficiency etc were characterized and described as follow.

(a) Spectrometer quantum efficiency

Quantum efficiency of the spectrometer is mainly decided by the quantum efficiency of the cameras, efficiency of the grating as well as optical alignment. It decides how efficient the photons entering the spectrometer can be transferred into electrons generated on the cameras. The quantum efficiency was calculated by the percentage between the number of electrons generated on the camera and number of photons entering the spectrometer. The quantum efficiency for both cameras is 63%.

(b) SNR and signal sensitivity drop-off

The sample power signal to noise ratio (SNR) in a SD-OCT system in shot-noise limit is defined as [7]:

$$SNR_{SD} = \frac{\eta P_{sample} \tau}{h\nu} \tag{25}$$

where η is quantum efficiency of spectrometer which is 0.63, P_{sample} is the light power onto the sample which is 6mW, τ is the integration time which is 14 μs, h is Planck's constant which is 6.63×10^{-34} $J \cdot s$, ν is light frequency. Calculated sensitivity value is 115.4 dB.

A mirror was imaged as the sample to measure the system signal sensitivity drop-off. A neutral density filter was used to decrease the power to avoid signal saturation. The light power was kept the same in the sample arm, and reference arm was moved to vary imaging depth. Figure 11 shows the signal sensitivity drop-off with imaging depths. The signal sensitivity drop-off is less than 10 dB from surface to 1.5 mm. This problem can be ameliorated by either decreasing the pixel size of the camera or moving the interested region of the sample near surface, where reference and sample arms have shorter path difference.

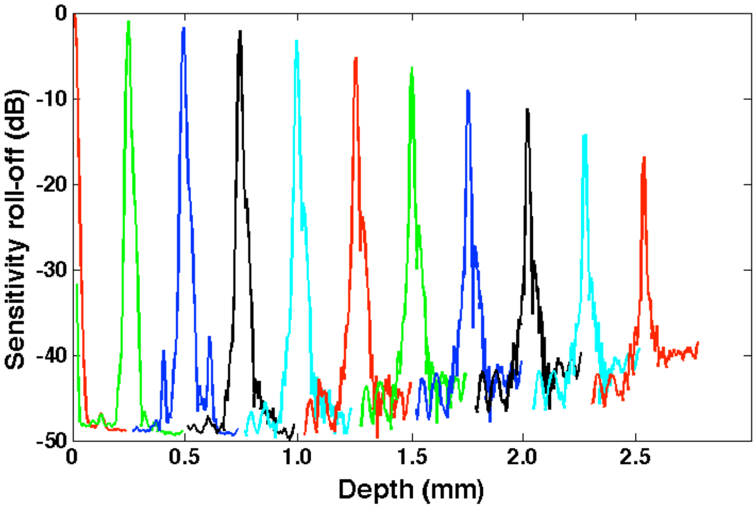

Figure 11. Signal sensitivity drop-off with imaging depth

Signal sensitivity drops as the path-length difference between reference and sample arms increases. The signal sensitivity drop-off can be described as the convolution of the spectral resolution function, which is a rect function of the finite pixel width of the CCD, with the interference signal in the frequency domain.

This problem can be ameliorated by either decreasing the pixel size of the CCD camera or moving the interested region of the sample near equal-pathlength point.

(c) Axial resolution

The theoretical axial resolution of SD-OCT system for the light source with a Gaussian spectrum is [66]:

$$\Delta z = 0.44\frac{\lambda^2}{\Delta\lambda} \tag{26}$$

A shorter wavelength or a wider bandwidth of the light source would result in a better axial resolution. The SLD used in this system has center wavelength of $\lambda_0 = 1298nm$, and the bandwidth of $\Delta\lambda = 120nm$. So the theoretical axial resolution is 6.2 μm for ideal Gaussian spectrum.

A mirror was imaged to characterize the axial resolution of the system on each camera. By moving the reference arm at different depths, the signal peaks were obtained as shown in Figure 11. The axial resolution was calculated as the FWHM of the signal peak in z-space, which is full width at -3dB of the peak. The axial resolution changes from 8 μm at the surface to 10 μm at depth of 2.6mm for both cameras. The measured axial resolution from the system is not as good as theoretical resolution calculated because the real spectrum of the laser source is not ideal Gaussian.

(d) Lateral resolution

The spot size at the focus point decides the lateral resolution of the system. Spot size can be calculated from the waist beam width of a focusing Gaussian beam. The theoretical lateral resolution of OCT system is [66]:

$$\Delta x = \frac{4\lambda}{\pi}\frac{f}{d} \tag{27}$$

where λ is the center wavelength which is 1298nm, f is the focal length of last lens which is 50mm here, d is the spot size on the objective lens which is 5mm, so the calculated lateral resolution is 16μm. To measure the lateral resolution of the system, an air force target was imaged. The FWHM of the peak obtained from the derivative of the image along the black lines is the lateral resolution. The lateral resolution is about 22 μm on both cameras. Better transverse resolution can be achieved by using focusing lens with larger numerical aperture that focuses the beam to a small spot size. The transverse resolution is also related to the depth of field b, which is two times the Rayleigh range [66]:

$$b = 2z_R = \frac{\pi \Delta x^2}{\lambda} \tag{28}$$

There is trade-off between transverse resolution and depth of field. Higher NA focusing limit achieves fine transverse resolution, but reduces the depth of field.

(e) Imaging depth

According to Nyquist theorem, the theoretical maximum imaging depth $z_{\max}$ is determined by [66]

$$z_{\max} = \frac{1}{4n_{ave}} \frac{\lambda_0^2}{\Delta\lambda} N \tag{29}$$

where λ_0 is center wavelength which is 1298nm, $\Delta\lambda$ is the FWHM of the light source which is 120nm, n_{ave} is averaged refractive index in the sample which is 1 in air, and N is number of pixels on the camera which is 1024 here. So the maximum imaging depth is calculated as 3.5mm in the air.

A mirror was imaged as the sample, while reference arm was moved to increase the path difference between two arms. The depth from surface to the peak position at the bottom of the image window is the imaging depth. The imaging depth of both cameras was measured as 2.95mm, which is smaller than that of calculated imaging depth. The theoretical computation is based on the Nyquist theorem that a minimum sampling rate was assumed to be two times of signal frequency. The interference signal can be resolved or sampled better with more number of camera pixels to receive the signal. However, the interference spectrum did not fully cover all the pixels on the camera. This caused under sampling of the spectrum thus a smaller imaging depth.

(f) System noise analysis

The noises in an OCT system include read-out and dark noise, shot noise and relative intensity noise (RIN). Read-out noise exists because the camera does not always yield the same result of converting photons into charge. Dark noise is the charge measured even there are no photons hitting on the camera. Both read-out noise and dark noise keep the same and cannot be removed. Shot noise is the electronic noise that originates from different number of photons hitting on the same pixel of the camera. Shot noise is proportional to square root of light intensity. RIN can be generated from cavity vibration, fluctuations in the laser gain medium or from transferred intensity noise from a pump source. RIN is proportional to the intensity. It improves the SNR with increasing laser power when it is limited by shot noise. Their contribution to the overall noise in electrons squared per read out cycle and per detector element are given by [6-7]:

$$\sigma_{noise}^2 = \sigma_{r+d}^2 + \frac{\eta e^2 P_{ref} \tau_i}{E_v} + \left(\frac{\eta e P_{ref}}{E_v} \right)^2 \tau_i \tau_{coh} [e^2] \tag{30}$$

where sample arm power was assumed to be much smaller than the reference arm power. σ_{r+d}^2 is the sum of read-out noise and dark noise. $\tau_{coh} = \sqrt{2 \ln 2 / \pi} \lambda_0^2 / c\delta\lambda$ is the coherence time. The optimal signal to noise performance is achieved when shot noise dominates both read-out noise and relative intensity noise (RIN). When $\eta e^2 P_{ref} \tau_i / \sigma_{r+d}^2 E_v > 1$, shot noise dominates read-out noise and dark noise. When $E_v / \eta P_{ref} \tau_{coh} > 1$, shot noise dominates RIN.

The optimal reference arm power is when read-out noise and dark noise are equal to the RIN. Thus when a system is operated close to shot-noise-limited performance, shot noise should dominate thermal and RIN noise at the optimal reference arm power [7]:

$$P_{ref} = \frac{\sigma_{r+d} E_{\upsilon}}{\eta e \sqrt{\tau_i \tau_{coh}}} \tag{31}$$

There are two SLDs in our system that one SLD contribute to 80% of the total power and the other contributing to 20%. In order to keep a high amplification from reference arm while not getting saturation signal, the reference light was put as 80% of the saturation power. The curve of standard deviation vs. average power on each pixel was obtained by taking the reference spectrum, shown in Figure 12 (a) and (b). The SLD with lower power makes the system work at shot-noise limit while the SLD with higher power is not.

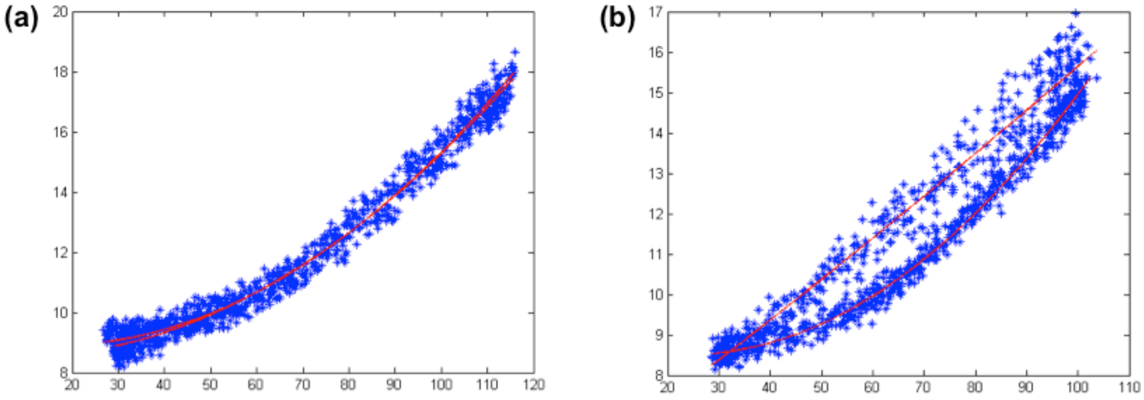

Figure 12. System noise on (a) horizontal camera and (b) vertical camera.

Dark noise is the standard deviation value that even no light on the camera, thus it is the offset value at the left start point in both figures. The shot noise is proportional to square root of intensity thus linearly proportional to the power measured. RIN is proportional to the square of the measured power. In Figure 12 (a) and (b), the shot noise corresponds to the linear portion in the curves and RIN corresponds to the non-linear portion. Both curves were fitted with second order linear regression. The differences between the fitted shot noise and RIN on both cameras were calculated, which showed a higher RIN than shot noise. This stated that the system noise is not shot noise dominated.

Intensity images

As stated in previous section, the intensity image was constructed by firstly interpolating the acquired spectrum with pre-calibrated wavelength on each pixel. This is followed with performing a Fourier transform to the spectrum to get a depth profile. Intensity values from both cameras were calculated, combined and converted into dB values. The last step was gray-scale encoding to obtain 8-bit color map (0-255). A finger nail fold was imaged *in vivo* with intensity image shown in Figure 13 (a). The image size is 4mm in in width and 2mm in height. Figure 13 (b) and (c) are anatomy of human finger nail fold [67].

The structures of the nail fold in OCT intensity image was recognized by comparing with nail anatomy shown in Figure 13 (b). The nail body, cuticle, nail root, nail bed, nail matrix, epidermis and dermis of skin were observed. The structures observed here match well with the OCT image of finger nail fold reported by other study [51].

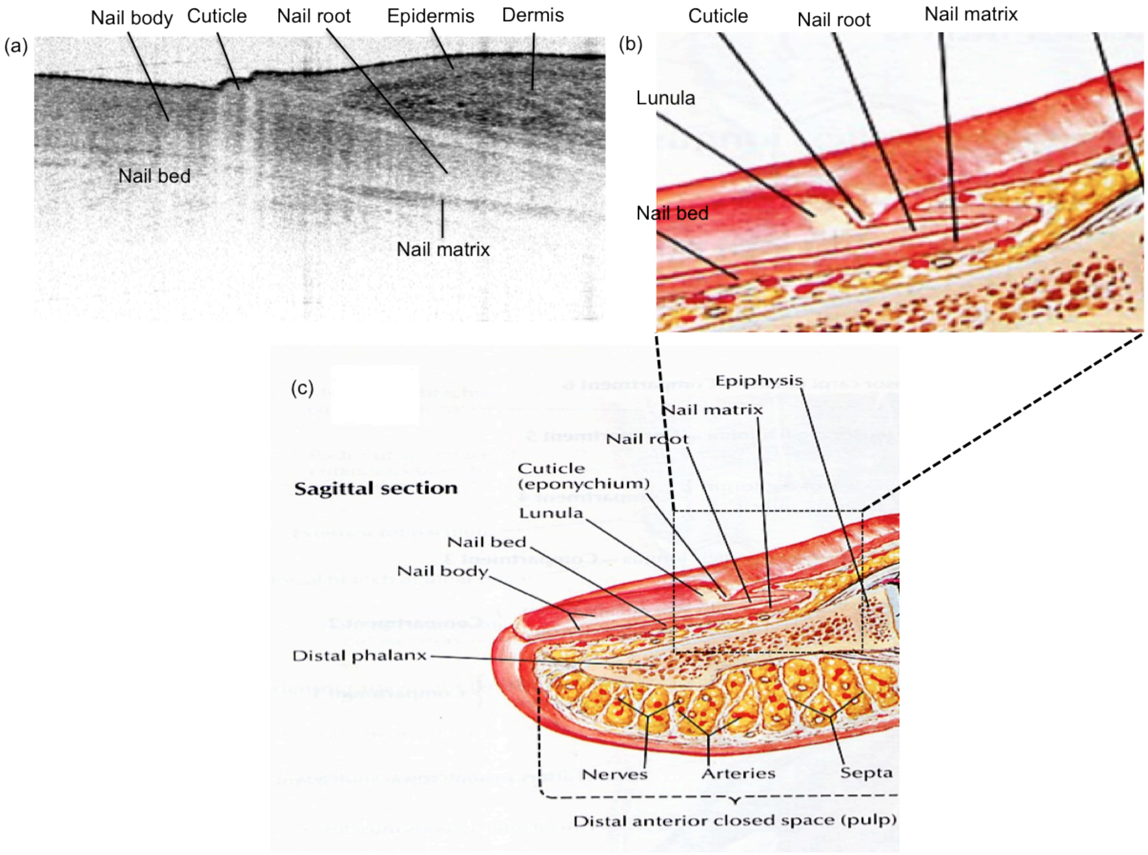

Figure 13. Structure of fingernail fold (a) OCT intensity image; (b) and (c) anatomy of fingernail fold [67]

Flow and phase stability

The minimum detectable phase difference is fundamentally limited by the SNR and fraction of beam width. The overall phase noise is [46]:

$$\sigma_{phase} = \sqrt{\sigma_{\Delta\phi}^2 + \sigma_{\Delta x}^2} \tag{32}$$

where phase noise caused by lateral scanning is [46]:

$$\sigma_{\Delta x} = \sqrt{\frac{4\pi}{3}\left(1 - \exp\left(-2\left(\frac{\Delta x}{d}\right)^2\right)\right)} \tag{33}$$

where Δx is the lateral distance moved, and d is the beam width at the focus. For 2048 A-scans per image, usually the scanning range is larger than 1mm for biological tissue, the beam width at focus is 10 micro meter, resulted phase noise is 0.14 radians. Increasing the scanning range to be 2 mm will increase phase noise to be 0.26 radians. The beam width fraction should be within 10% to maintain phase stability. The SNR dependent phase noise is [46]:

$$\sigma_{\Delta\phi} = \sqrt{2\sigma_{\phi'}^2} = (SNR)^{-1/2} \tag{34}$$

A coverslip was imaged as the sample without lateral scanning to determine the SNR dependent $\Delta\phi$ of the system. A variable neutral density filter was used to change the sample light power thus SNR. The phase difference was calculated from the front and back surfaces of the cover slip. Phase noise $\Delta\phi$ was calculated as the standard deviation of phase difference. The phase noise as a factor of SNR is shown in Figure 14. The above analysis is based on the hypothesis that the system is shot-noise limited. The deviation of the measured phase noise from the calculated noise exists because the actual system is not running at shot-noise limited range.

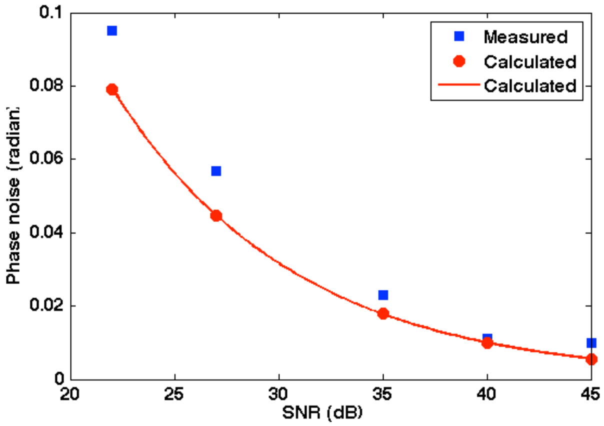

Figure 14. Phase noise calculated from a cover slip as a factor of SNR

In a word, the minimum flow thus overall phase noise is fundamentally governed by the fraction of beam width and SNR. The relationship between the flow velocity with phase difference is determined as [12]:

$$V = \frac{\Delta\phi}{4\pi\cos\theta}\frac{\lambda_0}{T} \tag{35}$$

The minimum detectable phase difference is $\Delta\phi = 0.01$ at SNR=45. The time between two successive A-scans is $T = 22.2\mu s$ when running cameras at 45kHz. In the case of the angle between the light beam and the flow direction is 0, the minimum detectable flow velocity calculated is 46 $\mu m/s$. As shown from above equation, decreasing camera speed to increase the time between two depth profiles would result in a smaller minimum detectable flow velocity. Decreasing SNR would increase the minimum detectable flow velocity.

Birefringence and PS-OCT characterization

An electro-optic modulator (EOM) was used to alternate the polarization states of light between two orthogonal states on Poincare sphere. The voltage that should be applying on the EOM and the polarization noise were characterized. The measurement of phase retardation, optic axis and diattenuation were also described below.

(a) Polarization noise of the system

The EOM is consisted of two lithium niobate crystals that are electro-optic crystal. An electric field applied to the crystal induces a change in the indices of refraction (both ordinary and extraordinary) giving rise to an electric field dependent birefringence. The electro-optic crystal acts as a variable waveplate with retardance linearly dependent on the applied voltage. The voltages that can alternate the incident polarized light by 90 degree on Poincaré sphere is +7V and -7V, this is amplified by a 20 times voltage amplifier. The two alternate polarization states of imaging a mirror with 2048A-scans within the frame is shown in Figure 15. The measured angle between two polarization states (red, blue) on the Poincaré sphere representation is 89.6 degree. The polarization noise (variation of each polarization state) is 0.15 radian. This means only phase retardation value larger than 0.15 radian can be discerned from this system.

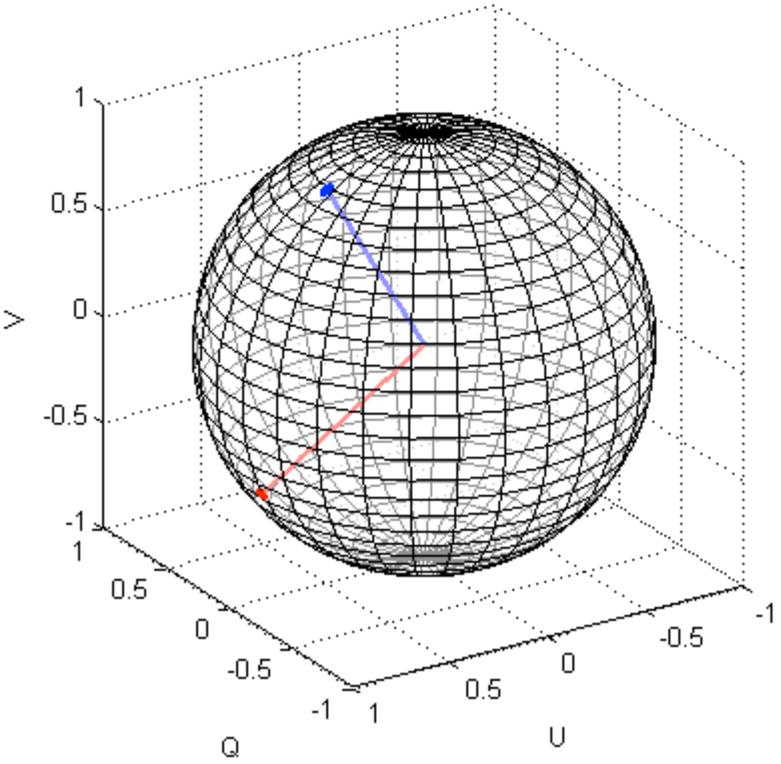

Figure 15. Two light polarization states altered by polarization modulator expressed on the Poincaré sphere, the angle between the two states is 89.6 degree.

(b) Computation of phase retardation

Stokes vector based approach is more computationally efficient thus it was implemented in the acquisition software described in Chapter 2. The general appearance of PS-OCT images were compared to a more rigorous Jones matrix-based method in post-processing. This Jones matrix approach has the advantage of determining relative optic axis, phase retardation, and diattenuation simultaneously [46,55]. Characterization data was obtained using a polarizing film for diattenuation and a wave plate for phase retardation. The polarizing film had a diattenuation of 1 and the wave plate had a round-trip phase retardation of 166° at 1300nm. The round-trip diattenuation and phase retardation were calculated for these two samples separately using the Jones matrix method. The measured round-trip diattenuation using one polarizing film at different set orientations is 0.98±0.002 (Figure. 16(a), red dots, PF1). The measured round-trip phase retardation of the wave plate is 167.5±2.5° (Figure 16(b), red dots, WP). The measured optic axis orientation is shown in Figure 16(c) with red dots. The measured round-trip diattenuation, round-trip phase retardation and optic axis orientation match the theoretical values. A polarizing film with diattenuation of 0.15 (measured as 0.15±0.022 shown in Figure 16(a), blue squares, PF2) was placed on top of the same wave plate with their optic axes aligned. Measured round-trip phase retardation and diattenuation after placing the polarizing film are 167.4±5.2° (Figure 16(b), blue squares, PFWP) and 0.179±0.085 (Figure 16(a), black triangles, PFWP) respectively. The measured optic axis is shown in Figure 16(c) with blue squares. Both sets of measurements (the separate samples and combined sample) agree well with theoretical values. A combined sample comprised of a polarizing film and a wave plate demonstrates that phase retardation, diattenuation, and optic axis can be measured using the Jones matrix method.

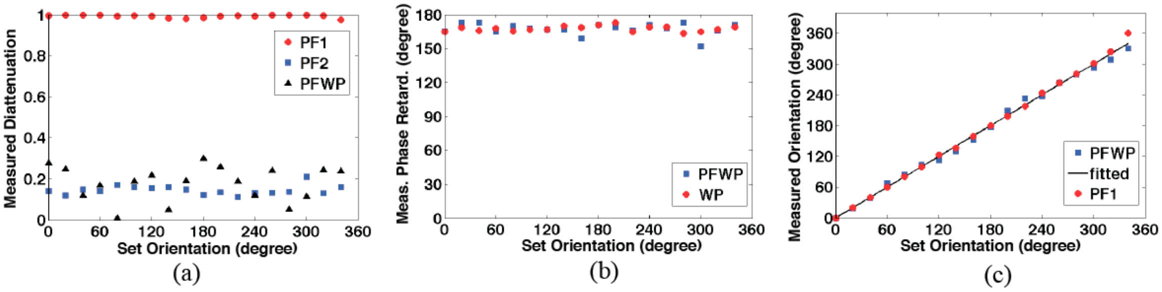

Figure 16. Characterization of phase retardation, optic axis, and diattenuation. (a) Measured round-trip diattenuation of polarizing films; (b) measured round-trip phase retardation of a single wave plate and combined sample with a polarizing film; (c) measured optic orientation of single polarizing film and combined sample with a polarizing film atop of wave plate.

It is known that muscle tissue is highly birefringent and adipose tissue is not [68-69]. Chicken muscle and adipose were imaged under PS-OCT. Post processed intensity and PS-OCT images of adipose and muscle tissue are shown in Figure 17. It is clear that adipose tissue is not birefringent and muscle is highly birefringent, as demonstrated by the striped pattern in the PS-OCT image. Phase retardation was quantified by averaging the phase retardation over regions of muscle and adipose tissue starting from sample surface. A linear fit was applied to the resulting curve and the slope extracted as a measurement of phase retardation per unit depth. The averaged slope for adipose and muscle are shown in Figure 17(g) and (h). The phase retardation per unit depth is 0.8821±0.045°/µm for muscle tissue and -0.026±0.08°/µm for adipose tissue. As proof that the above characterization can accurately extract phase retardation amidst the existence of diattenuation, the polarizing film with diattenuation of 0.15 was put on top of the sample of chicken muscle and imaged as a single sample. Extraction of phase retardation requires identical eigenvectors determined from the Jones matrices of the sample and film. The polarizing film was carefully put atop of the chicken muscle with their optic axes aligned in the same direction.

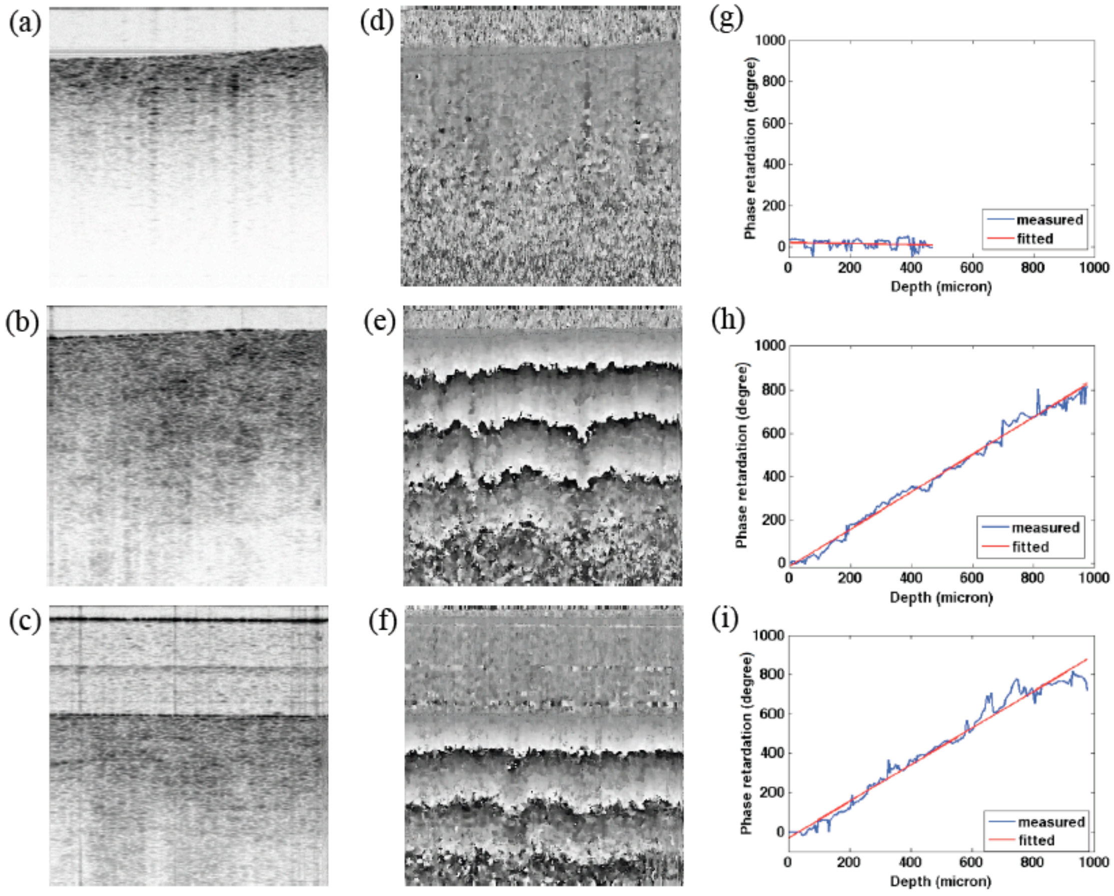

Figure 17. Intensity, PS-OCT images, and averaged phase retardation along depth for chicken adipose tissue (a, d, g), muscle (b, g, h) and a polarizing film putting on top of the same muscle (c, f, i).

Figure 17(c), (f) and (i) show the intensity image, PS-OCT image and averaged phase retardation per unit depth. The measured average phase retardation per unit depth is 0.907±0.07°/μm, which agrees well with the previous measurement. The PS-OCT characterization and imaging results demonstrate the ability of our multi-functional SD-OCT system to maintain good sensitivity while operating the cameras at their maximum line rate of 45 kHz.

A mouse bifurcated sciatic nerves were exposed and imaged in vitro. Figure 18(a) is 2D cross-sectional intensity image with bifurcated nerves indicated by arrows. Nerves showed higher scattering than surrounding connective tissue and muscle. Figure 18(b) is cross sectional accumulative phase retardation image. Muscle tissue is very birefringent that shows black and white banding. The two nerves were indicated by arrows with the non-birefringent. The connective tissue lying on top and in between the nerves was not birefringent and showed as color of black. Figure 18(c) is the *en face* view of the 3D PS-OCT image volume at 200 um below the nerve surface. The nerve bifurcation was obviously shown in the figure. Bands of Fontana were observed on the left bifurcation indicated by arrows, similar to our previous publication [70].

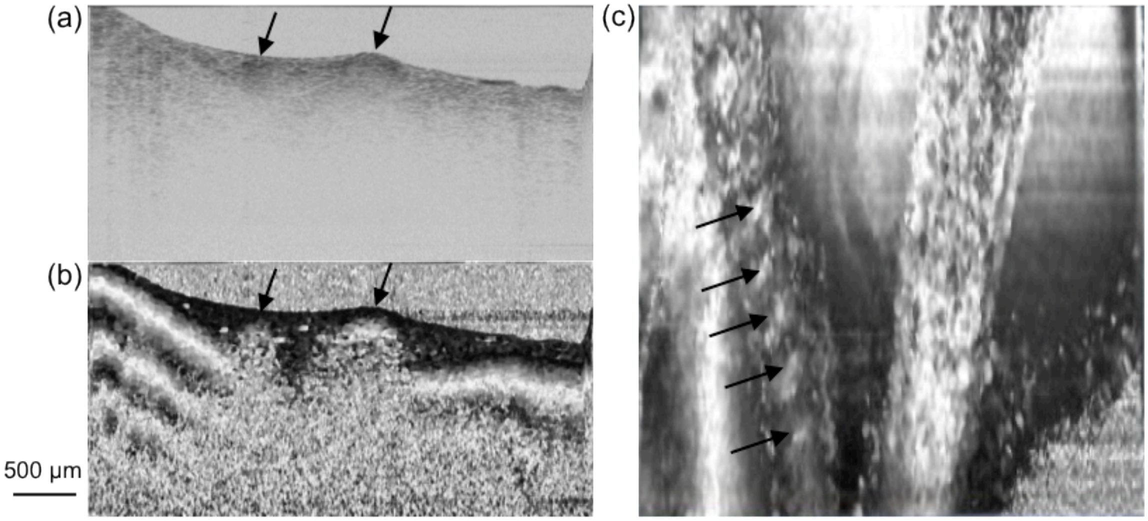

Figure 18. Intensity and polarization images of bifurcated sciatic nerves of mouse hind leg: (a) Cross-sectional intensity image; (b) Cross-sectional polarization image; (c) *En face* polarization image at 200 um below the nerve surface.

Multi-functional SD-OCT imaging result

A mouse hind leg was exposed for imaging the femoral artery, vein and nerve. Femoral artery, vein and nerve are enclosed in femoral sheath and lying on top of muscle tissue.

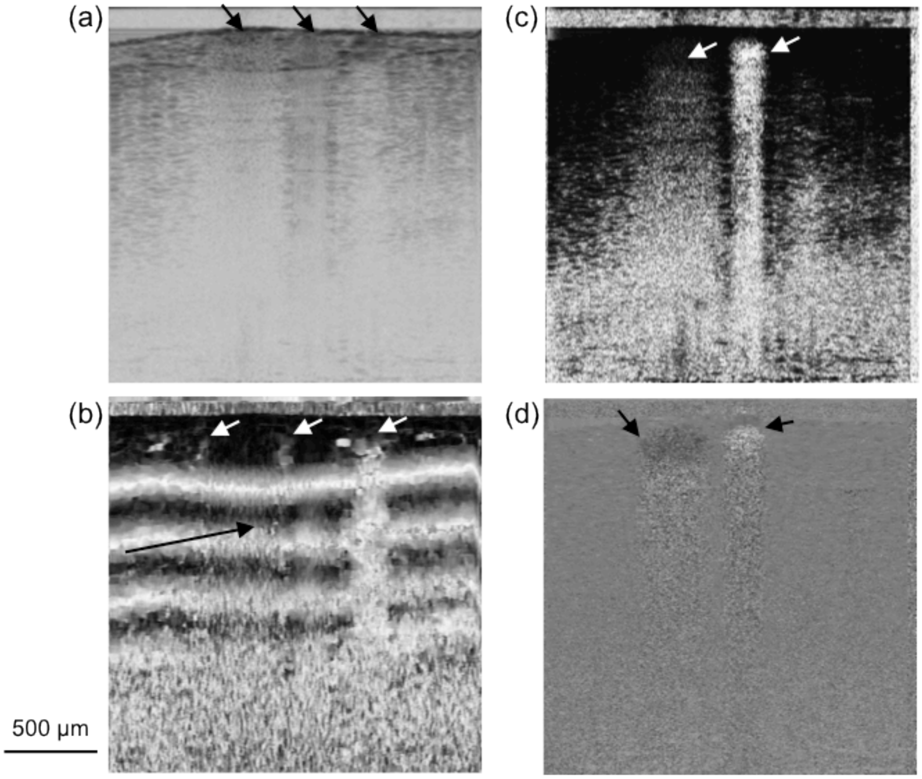

Figure 19. *In vivo* imaging of mouse hind leg with femoral artery, vein and nerve in imaging region (a) intensity image; (b) accumulative phase retardation image; (c) phase variance flow; (d) bi-directional flow.

The structure image in Figure 19(a) showed that blood vessels and nerve (indicated by arrows) exhibit higher scattering than other tissue. There are two blood vessels pointed out in phase variance image in Figure 19(c) that they have different flow speed. Bi-directional flow image in Figure 19(d) informs that the two blood flows were in opposite directions with darker and lighter colors. The leg muscle shows large area of black and white banding in accumulative phase retardation image in Figure 19(b). The birefringent tissues on top of muscle were identified as blood vessel walls and nerve by comparing with intensity and flow images. This multi-functional SD-OCT system allows simultaneously obtaining the intensity, polarization and flow images.

Discussions

A multi-functional SD-OCT system was constructed, calibrated and characterized. The system has an axial resolution of 8-10 microns, imaging depth of 3mm, sensitivity drop-off less than 10dB within 1.5mm in air, spectrometer quantum efficiency of 63%. The computation of phase retardation, optic axis and diattenuation was characterized by quarter wave plate and polarizing film. In a SD-OCT system, the axial resolution is decided by the light source center wavelength and bandwidth.

The axial resolution is inversely proportional to the light source bandwidth, if combining more SLDs into the source would result in better axial resolution too. The lateral resolution depends on the numerical aperture (NA) of last focus lens or objective, increasing the NA would bring a better lateral resolution but at the mean time decrease depth of focus. Thus there is a tradeoff between the lateral resolution and depth of focus. The imaging depth of most OCT systems is limited to 2-3mm because of limited penetration depth of light, and endoscope can be utilized to reach the tissue deeper than the imaging range. The line scan camera speed in 1300nm range is limited by the camera material which is InGaSn. At the time we started building the system, the fastest line scan camera we could get was 46kHz from Goodrich, the most updated camera has line rate up to 92 kHz from the same company.

The imaging results described in this chapter were all processed using MATLAB. The data processing to get intensity, polarization and flow images from the raw data using MATLAB is very time consuming. The data acquisition time of a volume with 2048 A-scans and 200 B-scans when running cameras at 45kHz is about 10 seconds. While it takes about 15minutes to process and get intensity, polarization and flow images in MATLAB. It is very time consuming if taking the data and process offline, then get back to imaging to adjust the ROIs. A real-time data acquisition and processing program would make it easier to adjust the ROIs during imaging with real-time image display. In the second chapter, the computation acceleration in the real-time program to reach real-time image display is introduced.

Chapter 2: GPU accelerated computation in the multi-functional spectral-domain optical coherence tomography system

Abstract

Real clinical scenario usually requires real-time image acquisition, processing and display. This brings a need for fast computation speed to process acquired data and display images in real-time. Image processing in an OCT system is usually time consuming because of the large amount of data acquired, this takes even longer time in a multi-functional SD-OCT system. Graphics processing unit (GPU) technology has been applied on acceleration of image processing in medical imaging techniques these years. The many numbers of stream processors and its intrinsic computation parallelism allows fast data computation speed acceleration by a GPU card. In this chapter, GPU was incorporated into the multi-functional SD-OCT system described in Chapter 1. CUDA C++ code was implemented into the real-time acquisition and processing program to process the intensity, polarization and flow images. The first GPU card incorporated into the system was NVIDIA Tesla C1060 released in 2008. This increased the image computation speed by 5 times. A second GPU card NVIDIA Tesla K20 released in November of 2012 was upgraded into the system to further increase the computation speed by another 20 times. This resulted in a total computation speed increase of 100 times compared to the previous CPU computation.

Introduction

With the advances in hardware, the line acquisition rates of spectrometer based OCT system has been increased to be 500 kHz [71], and swept-source OCT system has reached to 2.5 million Hz [43]. However, the heavy computational load required to process the acquired data stream limits the realization of real-time OCT, especially multi-functional OCT imaging which not only processes intensity image but also functional images such as flow and polarization. Rapid visualization allows for quick identification of different features of biological samples in any of the three image types (intensity, Doppler, and polarization-sensitive) during acquisition. Beyond OCT intensity image processing, which involves spectral resampling, interpolation and a fast Fourier transform (FFT), performing multi-functional OCT imaging demands additional processing for reconstruction of both PS-OCT and Doppler OCT images, further increasing the total processing time [42-46].

It has been demonstrated of using a single field programmable gate array (FPGA) integrated circuit and custom electronics board to realize real-time display [35-38]. The A-scan processing rate was 27,648 A-scans/second for a SD-OCT system [37], and 54,000 A-scans/second for swept-source OCT system [38]. However, its cost on hardware is expensive and the customization requires specific expertise in FPGA technology, which needs logic gate design and programming in Verilog.

In recent decade, GPU technology has been developed to perform high speed computation at a low cost. A GPU has many stream processors that allows programmers to exploit the inherent parallelism. It has been demonstrated previously that an A-line processing rate of 680,000 A-scan/s can be achieved using GPU implementations of linear spline interpolation and the FFT [41]. A processing rate of 720,000 A-scan/s could be achieved by using GPU paged memory to render data in the GPU rather than copying back to CPU [42], and MHz A-scan processing rate by utilizing additional hardware FPGA in a swept-source OCT system [43]. GPU has also been utilized to reach real-time data processing of Doppler OCT [72-73]. However, GPU implementation of PS-OCT processing algorithms has yet to be demonstrated. A multi-functional OCT imaging system would allow rapid visualization of biological samples with enhanced contrast, allowing the user to scan samples quickly for features of interest to image.

Graphics Processing Unit

A GPU is specially designed electronic circuit for rapidly manipulating and altering memory to accelerate the building of images. The term GPU was popularized by NVIDIA in 1999, who marketed the GeForce 256. Figure 20 is an illustration of the difference between CPU and GPU [74]. A CPU is composed of only a few cores with lots of cache memory that can handle a few software threads at a time. While, a GPU is composed of hundreds or even thousands of cores that can handle threads simultaneously. GPU is specialized for compute-intensive and highly parallel computation. A GPU is designed to include more transistors for data processing rather than data caching and flow control like a CPU card.

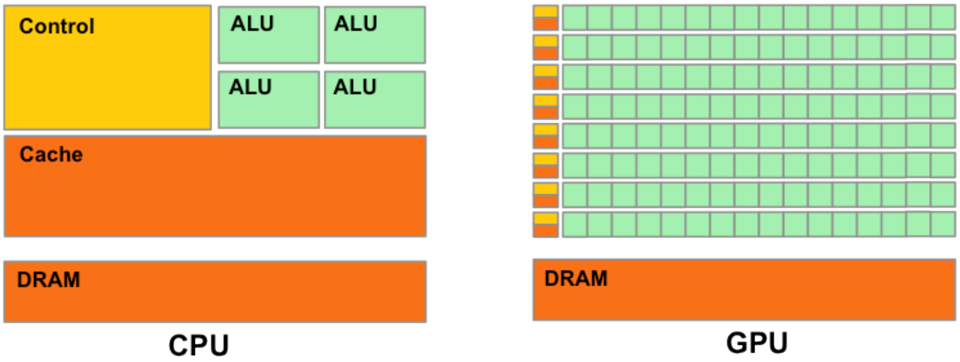

Figure 20. Structure differences between CPU and GPU. DRAM: memory; cache: for data caching; control: for flow control; ALU (arithmetic-logic unit): for data processing; GPU devotes more transistors to data processing. [74]

CUDA Architecture and memory hierarchy

CUDA is a parallel computing platform and programming model invented by NVIDIA that enable developers to use C as a high-level programming language on GPU [74]. The computation on the GPU card is executed by a kernel function, as shown in Figure 21. The data being computed is assigned to a grid composing many blocks and each block contains up to 1024 threads. Threads can be organized into one-dimensional, two-dimensional, and three-dimensional blocks of threads. Similarly, blocks can be organized into one-dimensional, two-dimensional, three-dimensional grid of thread blocks. The total number of threads within a grid equals to number of threads per block times number of blocks per grid. The total number of threads can be used is decided by the number of stream processors in the hardware. The actual number of threads needed for data processing depends on the data size.

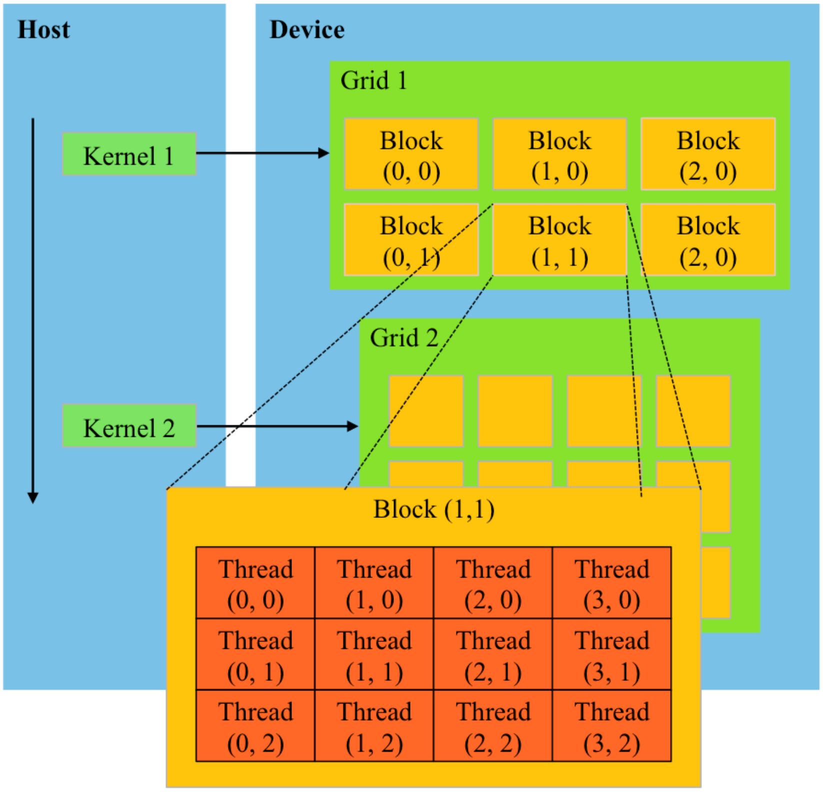

Figure 21. Kernel execution on CUDA, structure of grid, block and thread [74]

There are multiple memory spaces that CUDA threads may access data from during their execution. As shown in Figure 22, each thread has private local and registers memory. Each thread block has shared memory accessible to all threads of the block. All threads have access to the same global, texture and constant memory. The global, constant, and texture memory spaces are optimized for different memory usages. Constant and texture memory are read-only memory spaces. Texture memory also offers different addressing modes, as well as data filtering, for some specific data formats [74].

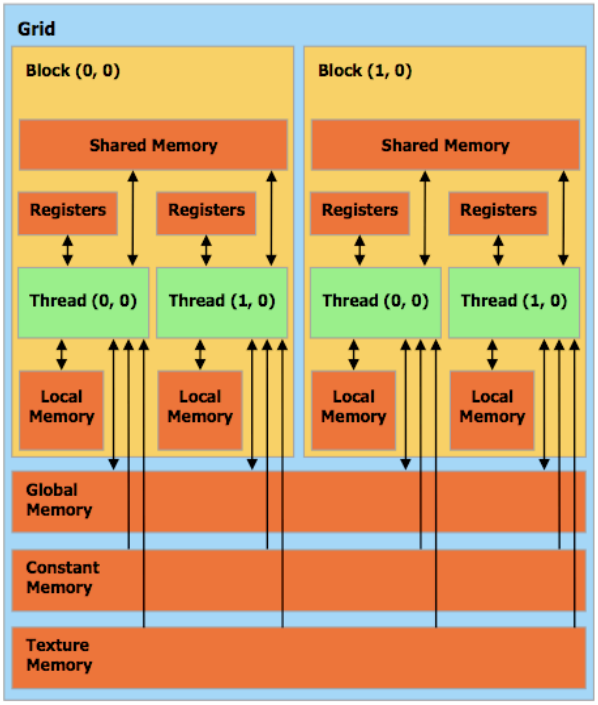

Figure 22. Memory hierarchy on CUDA [74]

Registers memory is fastest while only accessible by a thread. Ideally all local variables of a thread reside in registers on chip. However, this is limited by resource per multi-processor (several thousand with 32 bit each) and number of concurrent threads. Shared memory is living on chip that is extremely fast up to TB/s that is highly parallel and restricted to a block. Global memory is typically implemented in DRAM that has finite access bandwidth up to 177GB/s. Texture memory is written by the host and read by the device which lie in global memory. It is optimized for certain common read operations and is usually slightly faster than global memory. Constant memory is also accessible from everywhere with very limited device resource (a few dozen KB). It can also be written by host and read by the device. It is fully cached on chip so that can be accessed as fast as registers. Knowledge of the GPU memory hierarchy is very critical to maximize the computation performance. As global memory is slowest to access to that it should be reduced in usage as much as possible. A common way to reduce memory reads is to use shared memory to pre-load all data for a block. The shared memory was used in the computation that needs to read data for multiple times within a block. This will be stated more in detail in Methods section in this chapter. Texture memory was used for volume rendering that will be discussed in Chapter 3.

Incorporating CUDA C++ in Microsoft Visual Studio

In order to incorporate CUDA C++ computation code in a Microsoft Visual Studio program, there are multiple steps to include CUDA paths and make the program project compatible to the CUDA. First, the GPU card should be connected to the computer through PCIexpress slot. Related GPU driver, CUDA toolkit and SDK should be installed properly. Secondly, the customer build rules should be changed to cuda.rules in the Microsoft Visual Studio C++ program. Thirdly, in the VC++ directories under Tools in the C++ program, the directories of BIN, INCLUDE and LIB need to be changed through corresponding paths of CUDA toolkit. Furthermore, CUDART.lib and CUTIL32D.lib should be added to the Additional Dependencies under the C++ program project properties. After above changes and rebuilding the whole program, the program should be ready to include CUDA C++ code. The CUDA headers should be included into the file that allocate GPU memories and call the GPU execution code. The computation on

CUDA C++ is executed by kernel function, which needs to be defined that can be called for multiple times.

Acquired data is saved by default on host memory (CPU). The CUDA C++ computation is on the device memory (GPU), which requires data on the host memory to be copied to device memory. Executing computation on GPU includes: GPU memory allocation, data copy from CPU to GPU, kernel execution, data copy from GPU to CPU, free GPU memory. Below is a simple example of adding two arrays with N elements A and B into a third array C using C++ and CUDA C++ respectively.

The example CPU code is:

```
int main()
{
        size_t size = N * sizeof(float);
        for (n=0; n< N; n++){
            C[n] = A[n] + B[n];
        }
}
```

This requires N times of adding an element in A with an element in B into C. The consumption of time increases with size of arrays. Below is an example of doing the same computation using parallel computation on CUDA C++. First, GPU memories were allocated for all three arrays. Secondly, the data residing in arrays A and B were copied from host to device memory. The grid size was assigned with one dimensional grid and one dimensional block. The number of threads per block was defined as 256. The number of blocks was data size N divided by block size which is N/256. Each element in arrays A and B was assigned to a parallel thread in the grid for parallel computation. This is followed by execution of kernel function VecAdd that was separately defined. The kernel does the computation of adding each element in A and B into C all simultaneously. The last step was copying the result from device memory to host memory.

```
int main(){
        size_t size = N*sizeof(float);
        float* d_A, *d_B, *d_C;
        cudaMalloc(void**)&d_A, size);
        cudaMalloc(void**)&d_B, size);
        cudaMalloc(void**)&d_C, size);
        cudaMemcpy(d_A, h_A, size, cudaMemcpyHostToDevice);
        cudaMemcpy(d_B, h_B, size, cudaMemcpyHostToDevice);
        int threadsPerBlock=256;
        int blocksPerGrid = N/threadsPerBlock;
        VecAdd<<<blocksPerGrid, threadsPerBlock>>>(d_A, d_B, d_C);
        cudaMemcpy(h_C, d_C, size, cudaMemcpyDeviceToHost);
        cudaFree(d_A);
        cudaFree(d_B);
```

```
        cudaFree(d_C);
    }
```

The kernel function VecAdd being called was defined as:

```
    __global__ void VecAdd(float* A, float* B, float* C)
    {
        int i = blockIdx.x * blockDim.x + threadIdx.x;
        if (i<N){
            C[i] = A[i] + B[i];
        }
    }
```

Memory allocations on GPU and data copy between CPU and GPU are necessary for GPU computation. It is more advantageous to do computation on GPU with larger data size and more computation load. Newer GPU cards with Fermi or Kepler structure allow zero copy time between CPU and GPU by using pinned memory which will be discussed in Results section in this Chapter.

Materials and Methods

An NVIDIA Tesla C1060 card (GPU; 240 cores, 1.296 GHz clock speed, 4GB physical memory with 800MHz speed) is connected to the motherboard via PCI-Express 2.0 x16 interface, as shown in Figure 23. The synchronized trigger signals were sent via two BNC boards (BNC 2110 and 2120) and one data acquisition card National Instrument PCIe 6259) to the two cameras, two-axes scanner (GX and GY), and an electric-optic modulator (EOM). The raw data acquired from the two line scan cameras (lsc) was sent to the motherboard via two frame grabbers (National Instrument, PCIe 1429). The computer unified device architecture (CUDA) version 4.0 developed by NVIDIA was used for computation on GPU.

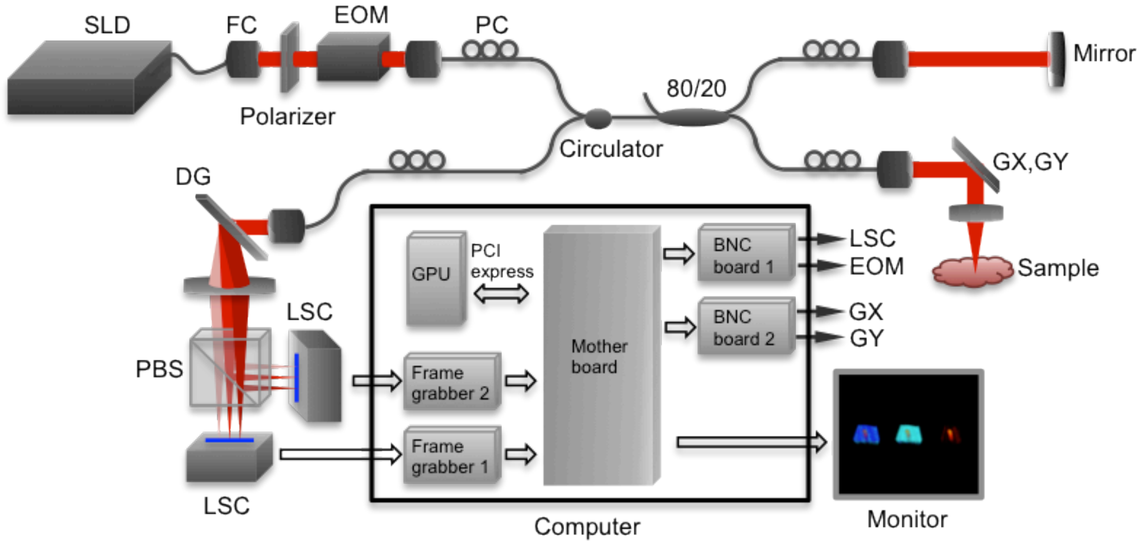

Figure 23. Set-up of the multi-functional SD-OCT system with GPU

The real-time acquisition program was written in Visual C++ in Microsoft Visual Studio 2008, similar to the program written in previous SD-OCT system [ref], but with significant modifications to the basic thread structure to accommodate GPU processing. Figure 24 is a flowchart of the multi-threaded data acquisition and processing program. It includes three main tasks that are data acquisition, processing and saving. The multi-threaded program sends synchronized control signal to the cameras, galvanometer-mounted-mirrors and polarization modulator. In the meantime, the raw data acquired from ring buffer is copied to data nodes in acquisition thread. Saving thread saves all the acquired data into a specified folder while processing thread processes the raw data and displays the appropriate images on the different views in the graphical user interface (GUI). Processing thread controls the data transfer to and from the GPU, as well as the kernel invocations required for GPU processing of the different views (intensity, Doppler, and polarization-sensitive imaging). The overall system speed is dependent on these three threads. Camera acquisition speed decides the data acquisition speed, which is 45kHz here. The data saving speed depends on the writing speed of computer hard drive. The data processing speed relies on the computation speed of CPU or GPU as well as amount of computation load. Among all these three main tasks, the slowest step is data processing thread. This is because there are two channels of data for computation. More significantly, extracting the flow and polarization information is more computation intensive than intensity image only, thus it slows down the computation speed. The CUDA C++ code was incorporated into the processing thread to accelerate the computation speed.

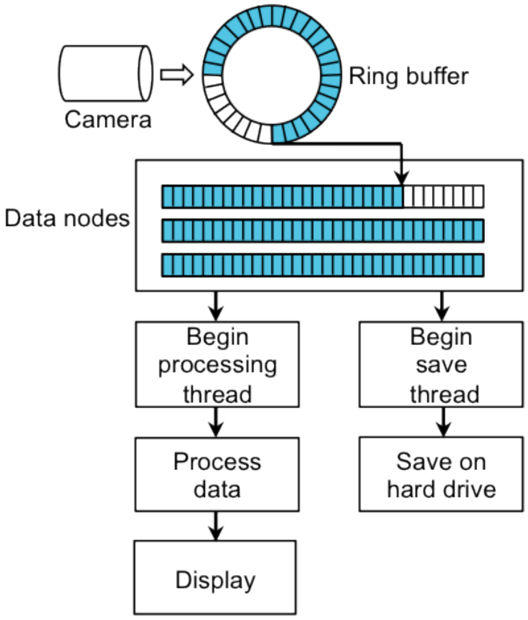

Figure 24. Flowchart of the data acquisition and processing program

Figure 25 is a flowchart of the data flow through the hybrid CPU-GPU processing scheme in the acquisition software. Pre-calculation for wavelength-to-wavenumber resampling and loading of the calibration files for this interpolation are both done during software initialization on the CPU. Raw data with size of 1024 pixels by 2048 A-lines was converted from 16 bit unsigned integers into 32 bit floats on the CPU, and then copied to the GPU for processing. In GPU memory, the averaged spectrum was first calculated for each polarization state and then subtracted from the appropriate spectra. Next, linear interpolation was performed. Interpolation parameters differ between the two polarization channels. The gray boxes in Figure 25 from the “resampled k” to “interpolation” steps indicate that two instances of the same thread logic with these different parameters were run separately. FFT operation was implemented using the CUFFT library provided by NVIDIA identically for both channels [75]. The data from these two channels was combined in a secondary processing step, which consisted of dB conversion and gray-scale encoding for intensity image display. The phase encoded by the complex result after FFT was used to calculate both phase retardation and flow.

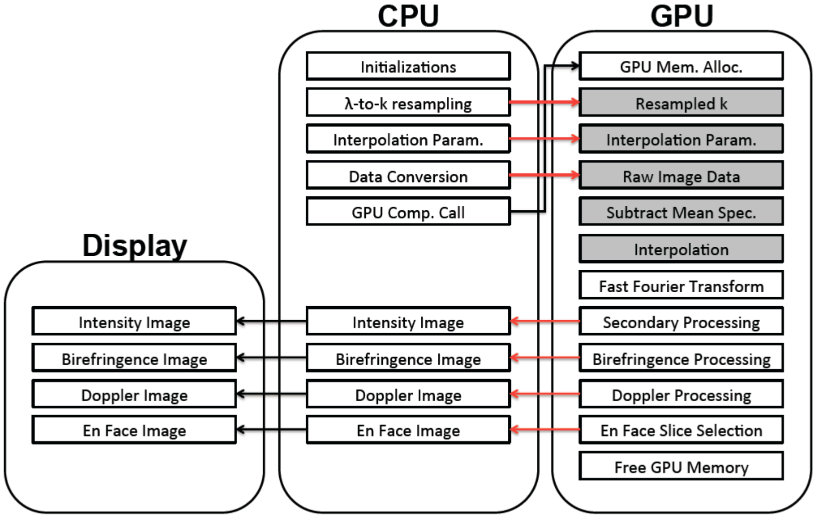

Figure 25. Flowchart of the computation and image display of the hybrid CPU/GPU processing scheme in the program.

The first step of computing phase retardation is to calculate the Stokes vectors (I, Q, U, V) from the complex data post FFT. The Stokes vectors were averaged in a box size of 3 by 5 to reduce the influence of noise. This step is extremely time consuming in the CPU program. This is much faster in CUDA C++ with the usage of shared memory. Then the Q, U, V components of Stokes vectors were normalized by the intensity I to be -1 to 1. The computation of phase retardation requires defining the sample surface as well as optic axis orientation. The sample surface was obtained by setting a threshold to each depth profile such that the first element that has intensity value above the threshold is taken as surface of that depth profile. This threshold value was computed in a relationship with maximum and minimum value of each A-line as well as threshold ratio. Parallel reduction was used in the process of searching extremes. The optic axis was calculated from surface and depth states of neighboring A-scans. Knowing the optic axis, the rotation angle from surface to depth within each A-scan for each polarization state is calculated. Then an overall weighted rotation angle is calculated from neighboring different polarization states taking account in the intensity weight. Lastly, bitmap encoding of phase retardation was performed into an 8-bit gray scale color map, in which 0 and 180 degrees are represented by black and white respectively.

The complex results post FFT includes the amplitude and phase that are readily to calculate flow information. The first step to calculate flow values is calculating the phase difference of neighboring A-scans. Since the polarization modulator alternates the polarization state by every other A-scan, so the phase difference was calculated from every other A-scans. The averaged phase difference within one A-scan was calculated by using shared memory and parallel reduction. Then the averaged phase difference is subtracted from the phase difference. As there are two channels of data here so the overall flow was calculated from the two channels with intensity weight. Lastly, the flow phase variance values are encoded in a similar color map, with zero and π^2 represented by black and white respectively.

Finally, an *en face* image is generated based on the desired image type (intensity, phase retardation or flow) by choosing a depth in an image and fetching the appropriate data from that depth in sequentially acquired cross-sectional images. The intensity (512 pixels by 2048 A-lines), phase retardation (512 pixels by 1024 A-lines), flow (512 pixels by 2046 A-lines) and *en face* (100 images by 2048 A-lines) bitmaps are then all copied back from GPU memory to CPU memory for display. Choosing the type of *en face* image and depth is done via a mouse click on any of the cross-sectional viewing frames in the GUI.

The GUI is comprised of five views with a sixth panel that shows program status (Figure 26). The spectra of the two cameras are shown at the bottom left (the red and green spectra distinguish the two cameras), top middle and bottom middle display the intensity image and the phase retardation image respectively, and the top right and bottom right display the flow image and *en face* reconstruction. The red spots in the intensity image indicate regions in which the SNR exceeds a pre-specified range, the yellow line in intensity, polarization and flow images indicate the depth of *en face* reconstruction, which can be toggled between the different views. The pixel number and approximate physical depth of the *en face* view is also shown in upper left corner of *en face* view. The sizes of the image views on the GUI were scaled reflect the physical size of the scanned region of the sample (2mm by 2mm). The position and size of the four image views can be adjusted depending on lateral scan width and user preference. The imaged sample in Figure 26 was a mouse brain with a thin skull preparation (2048A-lines × 200 frames × 512 points in depth, 2mm × 2mm × 2mm).

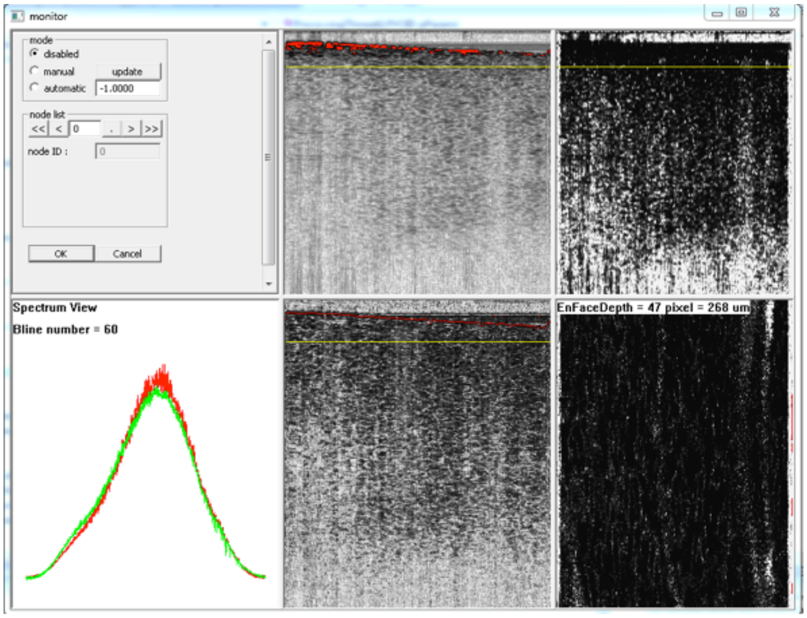

Spectrum View

Bline number = 60

EnFaceDepth = 47 pixel = 268 um

Figure 26. Snap-shot of the GUI of the real-time data acquisition program during imaging of a mouse brain with a thin skull preparation.

All image frames have 512 pixels in depth. The intensity, phase retardation and flow images have 2048, 1024 and 2046 A-lines respectively. The update rate for all the displays using strictly CPU processing is 2 frames per second. In the previous CPU version multi-threaded program, a main processing thread computed intensity image, then sent data after FFT done by using Intel Performance Primitives (IPP) to two threads to compute phase retardation and flow information separately. We see a 5x increase in the update rate to 10 frames per second when processing is performed on the GPU on the same computer.

A breakdown of the processing times for CPU and GPU processing is displayed in Table 1. It is clear that using a GPU to perform the computation necessary to reconstruct the three image types is faster compared to CPU processing. The total GPU processing and display time is 5 times faster than its CPU counterpart, despite the fact that 20% of the total time is used to transfer the data to and from the GPU. The effective A-line processing rate for intensity imaging only is 61 kHz. A significant improvement is demonstrated here using GPU-CPU hybrid processing compared to CPU processing.

Table 1. Time comparison of CPU and GPU calculation

Task	CPU time (ms)	GPU time (ms)
Copy from buffer to CPU	12	12
Copy between CPU and GPU	0	22
Calculate intensity	55	10
Calculate phase retardation	392	25
Calculate flow	549	12
Display	25	25
Total	549	106

To determine the minimum number of A-lines per image required to see an improvement using GPU to process intensity only and multi-functional images, we compared the total time to process and display a single frame using the purely CPU and CPU-GPU hybrid programs respectively, while varying the number of A-lines (Figure 27). The time difference between CPU and CPU-GPU processing of only intensity images increases as number of A-lines increases, indicating that GPU processing has an obvious advantage when processing larger amounts of data. The bulk of the GPU processing advantage come from the parallel implementation of the FFT. The time required to perform the FFT does not significantly increase with data size due to the efficient parallezation of different A-lines over the GPU cores. The time difference of computing all intensity, phase retardation and flow images by purely CPU and CPU-GPU hybrid programs increases even more rapidly with number of A-lines. When the number of A-lines increases to be 2048, the total time to process multi-functional images using GPU program is smaller than the time of computing intensity image only by purely CPU program.

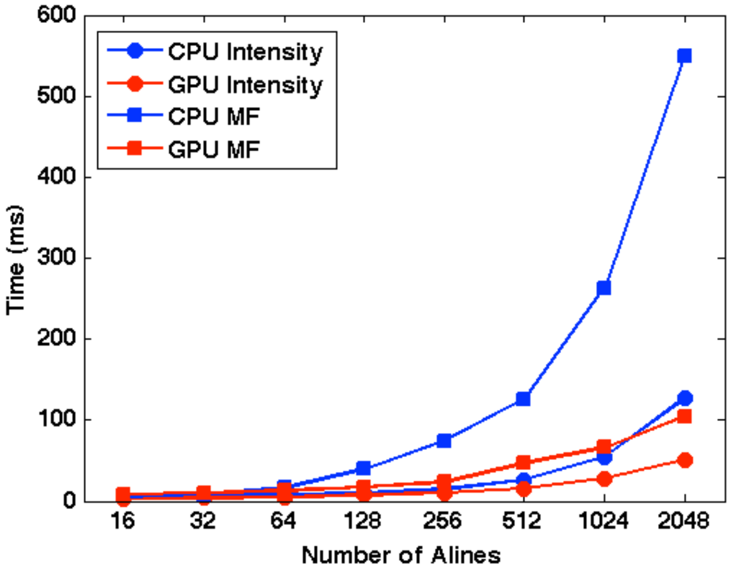

Figure 27. Time comparison of CPU and GPU computation of intensity image only and multi-functional images at different number of A-lines.

Results

Imaging and video recording of a Horseshoe crab eye

A live horseshoe crab eye was imaged *in vivo* using the hybrid CPU-GPU acquisition program. A horseshoe crab lateral compound eye is comprised of hundreds or even thousands of small segments called ommatidia. The compound eye was scanned in a volume of $0.8\times0.8\times2$ mm^3. Only the cross-sectional intensity and its *en face* images were calculated and displayed to test the processing program, every frame acquired was processed and displayed. Three different volume sizes were tested, which are: $256\times50\times512$ (12,800 A-lines/volume), $512\times50\times512$ (25,600 A-lines/volume), $1024\times50\times512$(51,200 A-lines/volume). These volumes were acquired and visualized at 3volumes/second, 3volumes/2seconds, 4volumes/5seconds, respectively.

The representative frames of videos recorded for above volume sizes are shown in Figure 28 (a), (b), (c) respectively. The *en face* depth was 380 μm from eye surface. Figure 28 (c) shows a representative frame of video for volume size of $512\times50\times512$ with *en face* depth 70 μm deeper. The intensity cross-sectional image is on the left and *en face* image on the right in each frame. In Figure 28(a), arrows in cross-sectional image point to crystal cone walls of ommatidia, and arrows in *en face* image indicate hexagonal ommatidia. The arrows in cross-sectional image of Figure 28(b) show the membrane fenestrate at the end of ommatidia. Moving 70 μm deeper in Figure 28(d), more ommatidia are seen on right section of *en face* image as indicated by arrows. A single ommatidium has a diameter of about 200 μm from the *en face* image.

The intensity images were updated on a frame-to-frame basis, and the *en face* image was updated simultaneously line by line. The program is capable of processing and updating image frames quickly enough for the *en face* image of the volume to be updated at a rate of 3 volumes/second for voxel size of $256\times 50\times 512$.

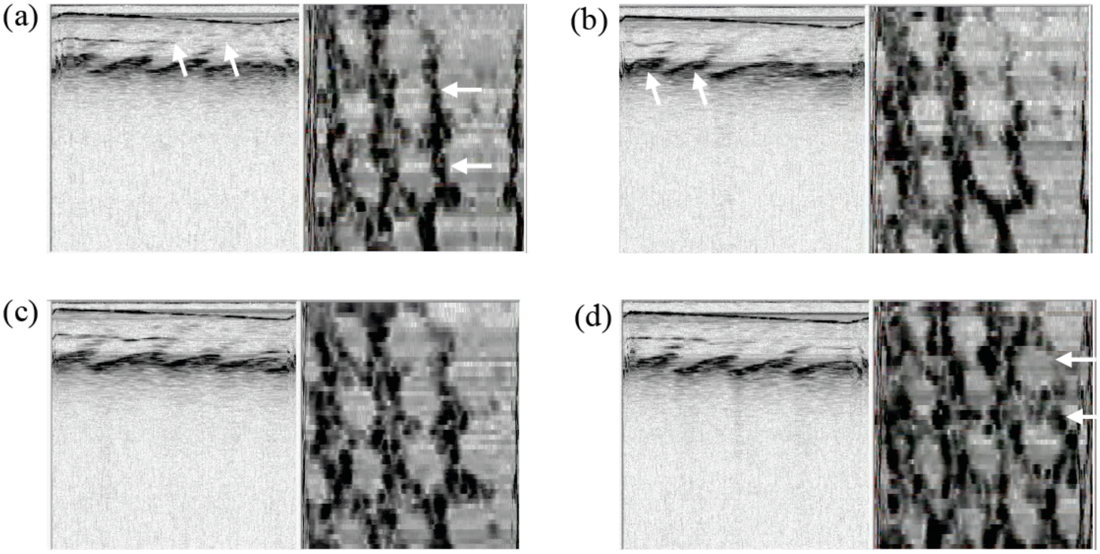

Figure 28. Live imaging of a horseshoe crab lateral compound eye, cross-sectional intensity image (0.8mm in width and 2mm in height) is on left and *en face* image (both width and height are 0.8mm) is on right. (a) $256\times 50\times 512$ voxels: *en face* depth is about 380 μm deep from eye surface; (b) $512\times 50\times 512$ voxels: same *en face* depth with (a); (c) $1024\times 50\times 512$ voxels (media 3): same *en face* depth with (a); (d) $512\times 50\times 512$ voxels, *en face* depth is 450 μm from eye surface.

Imaging and video recording of chicken muscle

In order to test the phase retardation computation of the CPU-GPU hybrid acquisition program, a piece of chicken muscle was imaged as heat was applied to the top right corner of imaging area. The scanned volume size is $1.3 \times 1.3 \times 2\text{mm}^3$ ($256 \times 50 \times 512$).

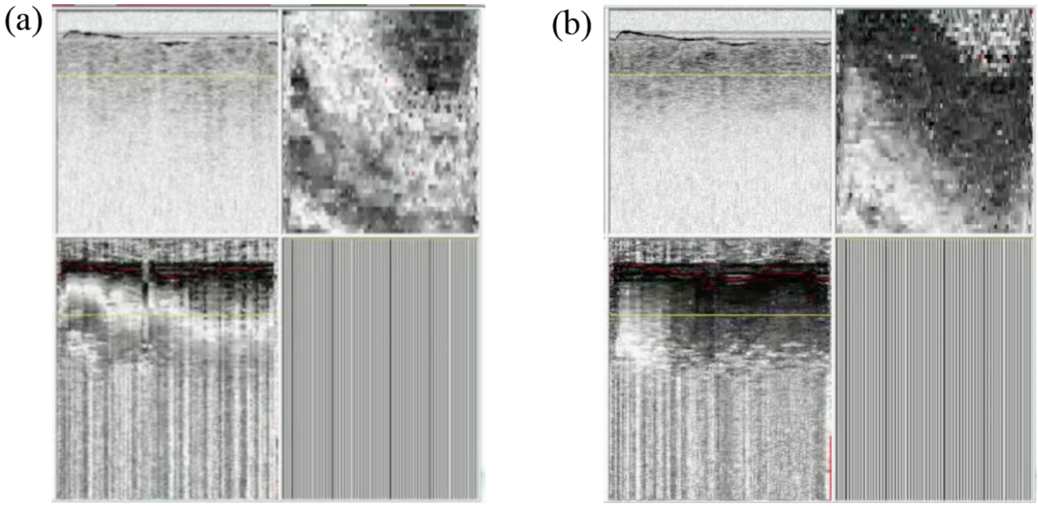

Figure 29. Imaging and video recording of chicken muscle, with heated applied to a lateral position corresponding to the top right corner: (a) A representative frame of the video when heat started transmitting from top right corner; (b) A representative frame when heat propagated to surrounding area.

The fast computation speed (1.7 seconds/volume) allowed visualization of the birefringence changes during propagation of thermal injury in the volume. Figure 29(a) and (b) are two representative frames of chicken muscle during heating process. In each frame, the image views are cross-sectional intensity (top left), phase retardation (bottom left), and *en face* phase retardation (bottom right) images. The yellow lines in the cross-sectional images indicate the depth of *en face* image. The cumulative phase retardation in *en face* image at chosen depth is roughly equal at the start of the recording as the sample was uniformly birefringent. As localized heat was applied to one corner, the cumulative phase retardation at the *en face* depth visualized changes non-uniformly as shown in Figure 29(a). In the cross-sectional phase retardation image, right half started losing more birefringence than left. As heat continued propagating to surrounding area, chicken in heated area gradually lost birefringence. In Figure 29 (b), the *en face* image showed a larger area of black, indicated low levels of cumulative phase retardation; this is reflected in the cross-sectional images, as the portion of the sample with less applied heat retained greater amount of birefringence than that where the heat was applied.

Imaging and video recording of microfluid flow

A microfluidic device was imaged in order to test flow computation (phase variance) of the CPU-GPU hybrid program. The program was set to process every other frame (1028 A-lines by 512 pixel) acquired such that while 200 frames/volume were acquired, only 100 frames/volume were processed and displayed in the GUI. The scanned volume size was $1.8\text{mm}\times1.8\text{mm}\times2\text{mm}$ ($1028\times100\times512$), and it took 5 seconds to update one volume. As shown in Figure 30(a), a micro channel with 600 μm in diameter was carved on a polydimethylsiloxane (PDMS) sheet and fixed to a glass slide with 1.1 mm thickness. One end of the micro channel was connected to a syringe through a plastic tube and a needle, the other end of the micro channel was connected to a petri dish containing diluted intralipid through a tube. The syringe could pump in and out diluted intralipid through the micro channel by pushing or pulling the syringe. The microfluidic device was imaged with glass slide surface close to the incident beam. Figure 30(b) is a representative frame of the video recording fluid change, the four views are cross-sectional intensity image (top left, 1.8mm × 2mm), *en face* flow image (top right, 1.8mm × 1.8mm), cross-sectional flow image (bottom right, 1.8mm × 2mm), cross-sectional phase retardation image (bottom left, blocked during video recording). In order to focus the light at the microfluidic channel, the glass slide was slightly shifted towards to the complex positions to portray a more intense image of the microfluidic channel on the display. The top surface of the glass slide was indicated by arrow 1 in Figure 30(b), and arrow 2 showed bottom layer of glass slide sticking with PDMS. In cross-sectional flow image, the white region shows the spatial position where there was flow change, the black rings indicate phase wrapping as phase change went beyond pi. Turbulent flow was observed shown as two regions of flow, similar to the observation by Bonesi [76].

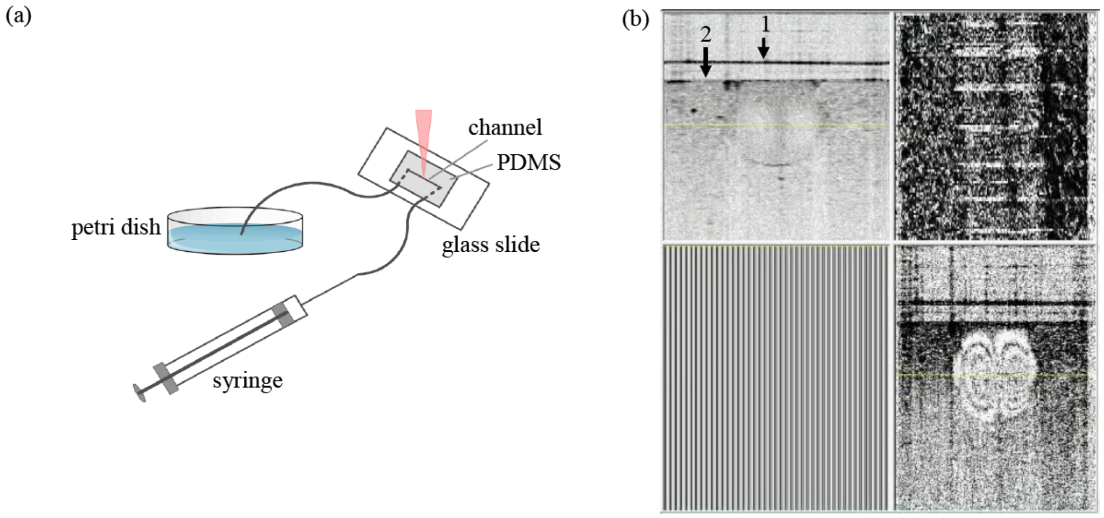

Figure 30. (a) Set-up of the microfluidic device: the micro channel with 600 μm diameter was carved on a PDMS sheet and fixed to a glass slide. (b) A representative frame of imaging flow change in the microfluidic device (media 6).

Multi-functional imaging of a mouse brain

A mouse brain with a thin skull preparation was imaged *in vivo* by using this multi-functional SD-OCT system. The CPU-GPU hybrid processing program is capable of processing and displaying every other image frame (512 pixel by 2048 A-lines) and update the intensity, phase retardation and flow images, as well as the *en face* image of the selected image type at the selected depth (10 frames per second). The scanning volume was composed of 400 frames, processing every other image frame results in 200 frames displaying in the volume ($2mm \times 2mm \times 2mm$, $2048 \times 200 \times 512$).

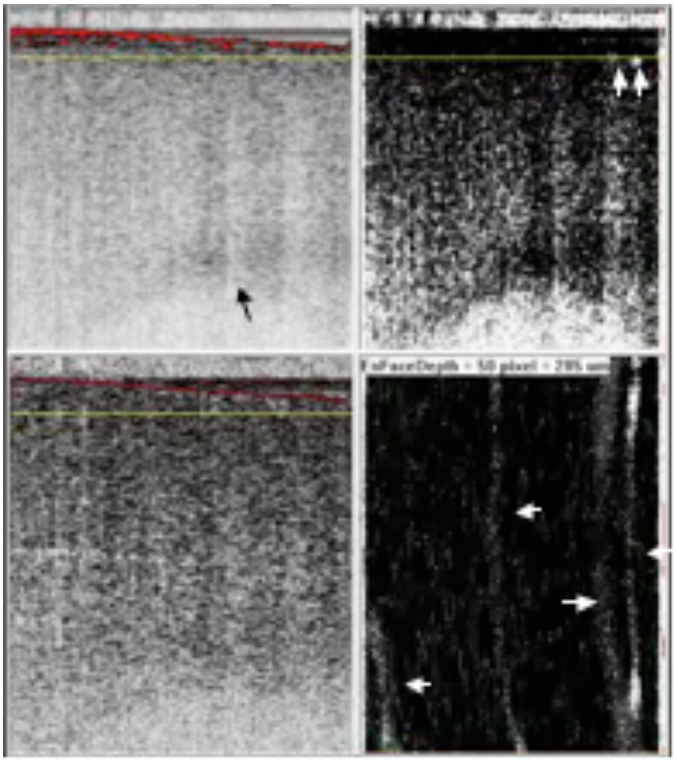

Figure 31. A representative frame of *in vivo* imaging a mouse brain with thin skull (media 7): cross-sectional intensity image (top left), cross-sectional flow image (top right), cross-sectional phase retardation image (bottom left) and *en face* flow image (bottom right). The image sizes are all 2mm by 2mm.

Figure 31 shows a snapshot of the 4 image views of the GUI during *in vivo* imaging of a mouse brain with a thin skull preparation. The four views are cross-sectional intensity image (top left), flow image (top right), phase retardation image (bottom left), and *en face* flow image (bottom right) respectively, the image sizes are all 2mm × 2mm. The red spots in intensity image indicate signal saturation at the surface, the red line in polarization image shows the surface of the sample. The yellow line in intensity, flow and phase retardation indicates the depth of *en face* image in volume. This depth was also shown in *en face* image as number of pixels and microns. In the intensity image, corpus callosum was visible with higher scattering indicated by arrow. The gray matter was weakly birefringent thus it showed generally dark in phase retardation image. The cross-sectional flow image captured the spatial cross-section positions of two blood vessels in this frame indicated by arrows. In the *en face* flow image after finishing scanning the whole volume, four blood vessels were visible at the chosen *en face* depth. As the blood vessels did not lie exactly on the same *en face* plane, that flow signal was weaker or stronger for part of blood vessels at this specific depth.

Optimization of computation program

The hybrid CPU-GPU program has 5 times increase in computational speed compared to the previous CPU version of the program. This program was further improved to additionally increase the computation speed by 20 times faster. The optimization included upgrading with a more powerful GPU card with newer computation architecture as well as better improvement on the programming code. The changes are stated as below:

(1) Upgrading GPU card

With the advancement and innovation on GPU development, newer versions of GPU cards have more number of processor cores as well as larger memory and memory clock speed. More importantly, newer generation of CUDA architectures such as Fermi and even newer Kepler enable significantly more efficient computation. The first GPU card NVIDIA Tesla C1060 (released in 2008) was replaced by NVIDIA Tesla K20 (released in November 2012). Table 2 is a comparison of specifications between the two GPU cards:

Table 2. Comparing specifications of two GPU cards

Specifications	Tesla C1060	Tesla K20
Number of processor cores	240	2496
Processor core clock	1.296 GHz	706 MHz
Memory	4 GB	5 GB
Memory clock	800 MHz	2.6 GHz
Architecture	No Fermi	Kepler

(2) Reducing data copy time by pinned memory

As we discussed previously, data transfer between GPU and CPU takes significant amount of time comparing to the total time (~20%). This is a common issue by using earlier versions of GPU cards. The new GPU card has Kepler architecture thus allows zero copy time between CPU and GPU using pinned memory [42].

(3) Reduction in memory usage

Decreasing the amount of memory for computation would reduce the computation time in both CPU and GPU. The temporary memories that used for containing polarization data and flow data share the same memory size. This largely decreased the usage of memory thus saved overall computation time.

(4) Subtraction of reference spectrum

The interference signal received by the detector has three terms as stated in Eq. (2), the light power from sample is about 1% of reference light. The sample information is mainly stored in the interference term that is amplified by reference light. The reference spectrum needs to be subtracted to leave only the interference term to extract sample information. The reference spectrum can be acquired taking the reference light spectrum while blocking the sample arm. Another way to save this extra step is taking the average of all the depth profiles as the reference spectrum for subtraction. This is because averaging many depth profiles would wash out the fringes and get close to reference spectrum. Subtracting the averaged spectrum was used in our first hybrid CPU-GPU program. Calculating the average spectrum was observed to take relatively long time thus this was replaced by taking reference spectrum directly. This was improved by placing a pinhole with shutter in the sample arm to block the sample light for reference spectrum acquisition.

The current hybrid CPU-GPU program was improved to be 20 times faster than previous hybrid CPU-GPU program and 100 times faster than the CPU program. Table 3 is a time comparison among three versions of programs. The image display time is also hiding by putting image display in another thread that running parallel with data processing. The image computation time is largely saved by better manipulation on the codes as discussed above. Thus the overall computation speed by the new program has been improved by 100 times faster than the CPU program and 20 times faster than previous GPU program by Tesla C1060.

Table 3. Time comparison of three versions of programs

Task	**CPU time (ms)**	**Tesla C1060 (ms)**	**Tesla K20 (ms)**
Buffer->CPU	12	12	0
CPU<->GPU	0	22	0
Intensity	55	10	1.2
Polarization	392	25	2.7
Flow	549	12	1.5
Display	25	25	0
Total	549	106	5.4

To compare the computation time of the three versions of program and data acquisition time, the time was plotted in bar graphs for direct view shown in Figure 32. The CPU computation time is way longer than the data acquisition time which limits real-time image processing and display. The first version of GPU program by Tesla C1060 largely increased computation speed and reduced data computation time by five times but still longer than data acquisition time. The new program by Tesla K20 with Kepler architecture tremendously increased computation speed and reduced the computation time to be much shorter than acquisition time, thus data computation does not limit the overall speed anymore.

The new GPU program can process A-scan rate at 379,259 A-scans/second, which is eight times faster than data acquisition speed. So the image update rate is not limited by data computation but camera acquisition rate now, this leaves space for future potential upgrading of faster cameras.

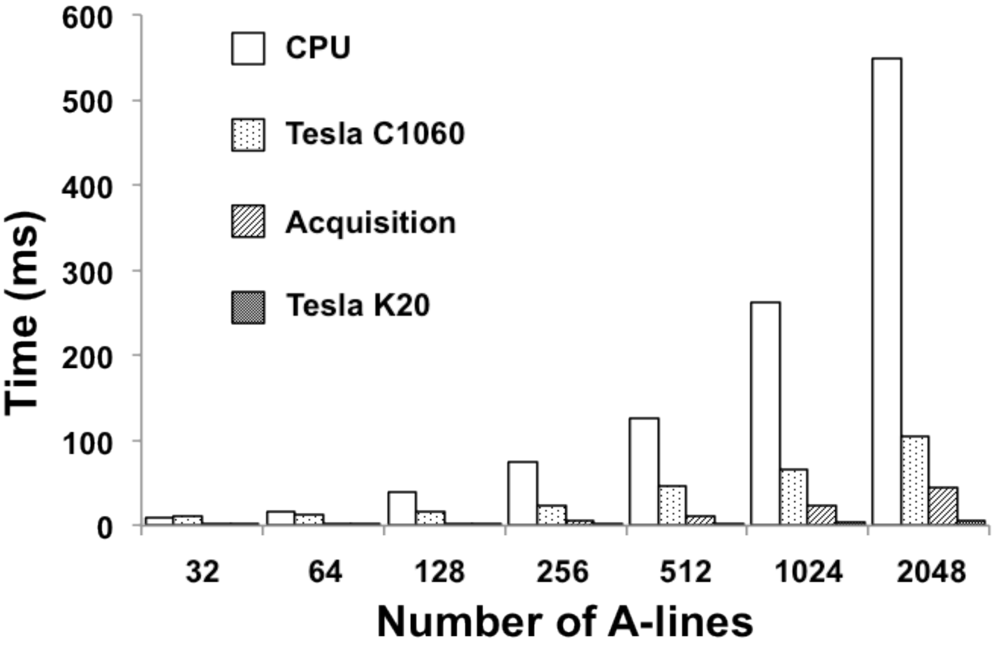

Figure 32. Comparison of computation time by CPU program, previous GPU by Tesla C1060, current GPU program by Tesla K20 and data acquisition time.

A human hand palm was imaged *in vivo* to demonstrate the update rate of this program, Figure 33 is a snapshot of video recording while imaging with a volume size is 4mm x 4mm x 2mm (2048 A-scans x 200 B-scans x 512 pixels). Top left is intensity image, top right is flow image, bottom left is polarization image, and bottom right is *en face* view of the polarization images in the scanned volume. The blue line in intensity, flow and polarization images indicate the depth of the *en face* image.

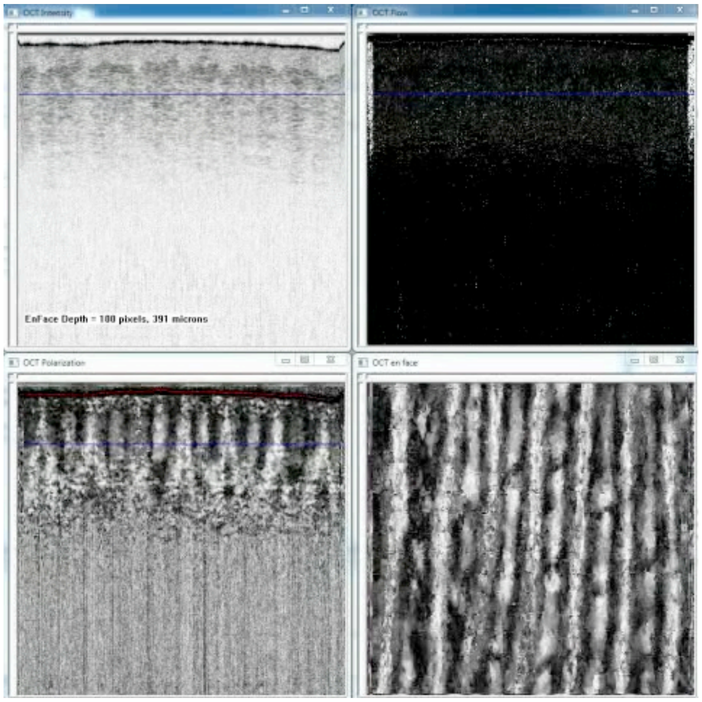

Figure 33. *In vivo* imaging of human hand palm with volume size of 4mm x 4mm x 2mm (2048 A-scans x 200 B-scans x 512 pixels). The four views are cross sectional intensity (top left), flow (top right), polarization (bottom left) and *en face* polarization (bottom right) images.

From the intensity image, epidermis and dermis layers are distinguished that epidermis layer is at surface with lower scattering and dermis layer is below the epidermis with higher scattering. As there were no blood vessels within the imaging range and depth that no blood flow appears in flow image. In the cross sectional polarization image, the collagen tissue in the dermal layer shows birefringence. The orientation and structure of collagenous tissue are more easily to be observed in the *en face* polarization image. The program was updating at 22 frames/second, which is limited by the camera acquisition speed. The actual processing capability is 185 frames per second.

Discussions

A GPU card and CUDA C++ code was incorporated into our multi-functional SD-OCT system at 1300nm for accelerated data processing. Using NVIDIA Tesla C1060, the data processing time of the GPU-accelerated program is five times faster than the previous CPU-based processing program. A horseshoe crab eye was imaged *in vivo* and four videos with varying volume sizes (12800, 25600, 51200 A-lines / volume) were recorded which gave volume update rate of 3 volumes / second, 1.5 volumes / second, 4volumes/5seconds, respectively. Structures of ommatidia were observed from the *en face* images and can be identified quickly due to the rapid visualization capability of our system. The fast visualization capability allowed visualization of large-scale birefringence changes due to localized heating of a chicken sample. The *en face* phase retardation image clearly showed the heat propagation from top right corner to surrounding area where showed black color with birefringence loss. A microfluidic device with a channel of 600μm in diameter was used to test the flow computation, the cross-sectional flow image showed the phase variance change, and turbulent flow was observed. The frequency of pushing and pulling syringe to pump diluted intralipid through the micro channel was visible in *en face* image. Finally, a mouse brain with a thin skull preparation was imaged with all image views (intensity, phase retardation, flow, *en face* flow) updating at a rate of 10 frames per second with the *en face* flow view displaying blood vasculature.

With advancement in GPU technology, the newest Tesla GPU card Tesla K20 has the Kepler architecture and more stream processors for faster computation. The computation speed was increased with a factor of 20 by upgrading the GPU card to be Tesla K20 and additionally optimization on the computation code. The line process rate of processing all intensity, polarization and flow images for two channels of data is 379,259 A-scans / second. This is eight times faster than current data acquisition speed which is 45,000 A-scans/second. Then a human hand palm was imaged *in vivo* with volume size of 4mm x 4mm x 2mm (2048 A-scans x 200 B-scans x 512 pixels). The collagenous tissue and the orientation in the skin dermal layer were clearly identified. The image update rate was 22 frames / second which is limited by the camera acquisition speed. The actual processing capability is 185 frames / second.

Current image update rate is not limited by data processing but by camera acquisition rate, which provides space for future potential of upgrading faster cameras. With fast computation speed increase in the 2D image processing, potential opportunity for incorporating volume rendering into the real-time program for volume visualization is also provided. The work of real-time volume visualization will be described Chapter 3.

Chapter 3: Real-time volume rendering of simultaneous intensity, polarization and flow images

Abstract

Real-time imaging and display is becoming more desirable as OCT has been more established and applied in clinical and research fields. Rapid visualization of 3D volume provides more information that is not immediate available in 2D images but requires very heavy computation. In this chapter, real-time volume rendering of simultaneous multi-functional (intensity, polarization, flow) OCT images based on GPU-assisted data processing is demonstrated. OpenGL was used for rendering and displaying volumetric images. The update rate of concurrent intensity, polarization, and flow images was two volumes per second with a volume size of 256 (X) × 64 (Y) × 256 (Z). A human finger nail fold and thermally damaged chicken muscle tissue were imaged to demonstrate the volume rendering of both intensity and polarization functionalities. The progression of the thermal injury in chicken muscle tissues could be clearly visualized in the rendered volumes during imaging. The exposed mouse femoral area was also imaged *in vivo* to capture simultaneous volumes of intensity, polarization, and flow. Finally, chicken muscle tissues with different burn damage were imaged with real-time volume rendering and display. The burn boundaries and depths were clearly defined from the real-time intensity and polarization volume images.

Introduction

3D volume image allows visualization of the information in the volume that is not immediate available in 2D slice images. Volume rendering techniques allow projection of a 3D discretely sampled data set composed of 2D image slices onto a 2D image. Thus viewing the 2D projection image allows visualization of information projected from 3D volume. Volume rendering is commonly used in medical imaging techniques such as CT, MRI, also OCT to display the volume images [77]. The realization of 3D volume image is typically done in a “save and process” mode that 3D data composed of 2D data slices were acquired and processed after data acquisition. Then 2D slice images in the volume were combined to display a 3D volume image. This “offline” volume rendering not only takes much time to visualize one volume image, but also more significantly loses possible activities that could be observed in a real-time manner. This creates a need for real-time volume rendering and displaying the volume image during data acquisition. Volume rendering is very computation comprehensive that can hardly be realized through computation on CPU in real-time. The powerful parallel computation capability of GPU has rapidly increased the 2D image processing by 100 times faster as stated in Chapter 2. Real-time volume rendering of intensity OCT [72] and Doppler OCT [73] was demonstrated with the usage of GPU. However, real-time volume rendering of PS-OCT images have not yet been reported. PS-OCT typically requires double of what is already a significant data stream, as it collects data from two orthogonally-aligned detectors, which further increases the computation load thus limits the speed of volume rendering. In this chapter, we introduce our work of real-time volume rendering of simultaneous intensity, polarization and flow images.

Volume rendering techniques

There are multiple volume rendering techniques that enable visualization of 3D volume image from 2D slice set. Volume ray casting projects the 2D image data set onto a 2D image plane [77]. The color (RGB) and opacity of each pixel on the image plane is calculated from all the pixels on the same eye ray. This gives the best image quality comparing to other volume rendering techniques. Splatting trades quality for speed; every volume element is splatted on to the viewing surface in back to front order. Shear warp is relatively fast in software with the cost of less accurate sampling and potentially worse image quality compared to ray casting. Maximum intensity projection picks out and projects only the voxels with maximum intensity that fall in the way of parallel ways traced from the viewpoint to the plane of projection. The computation is fast while the final 2D results do not provide depth information of the original data. Texture mapping method produces images of reasonable quality, while there is often a noticeable transition when rotating the volume. Another drawback of texture based method is that the sampling distances vary from ray to ray, introducing incoherences in the final image. In contrast, ray casting maintains a constant sampling distances, therefore avoiding visual artifacts. For these reasons, a volume ray casting approach was considered as the volume rendering technique to adding into the program. Its parallel computation architecture is very suitable for computation on a GPU card.

Figure 34 demonstrates how volume ray casting is working. Each pixel of the final image is computed from a single ray casting into the volume. The volume data is sampled at discrete positions along the ray. The contribution of each sample is accumulated to obtain the final color and opacity of the pixel. The ray casting algorithm exhibits an intrinsic parallelism in the form of completely independent light rays thus fits the parallel architecture of the GPU. In GPU ray casting, the volume data is uploaded to the GPU memory as 3D texture.

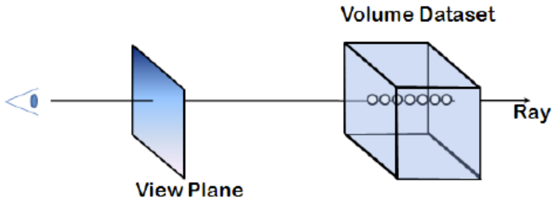

Figure 34. Volume rendering by ray casting: projection of volume data onto 2D image plane, every pixel from 2D image plane is accumulated from all pixels on the same eye ray in the volume data. [79]

The computation of ray casting is based on the equations below. The color and opacity value on the projected 2D plane are calculated from each pixel by recursive back-to-front compositing equation respectively [78]:

$$C(\lambda)_{out}(u_j) = C(\lambda)_{in}(u_j) \cdot (1 - \alpha(x_i)) + C(\lambda)(x_i) \cdot \alpha(x_i) \tag{36}$$

$$\alpha_{out}(u_j) = \alpha_{in}(u_j) \cdot (1 - \alpha(x_i)) + \alpha(x_i) \tag{37}$$

where $C(\lambda)(x_i)$ and $\alpha(x_i)$ are color and opacity values of a single voxel at the spatial position x_i. $C(\lambda)_{out}(u_j), \alpha_{out}(u_j)$ are the color and opacity values of the eye ray out of the voxel. $C(\lambda)_{in}\left(u_j\right)$, $\alpha_{in}\left(u_j\right)$ are color and opacity values of the eye ray into the voxel. u_i is the position on the image plane, x_i is the voxel location in the volume.

Volume ray casting on OpenGL

OpenGL is a multi-platform application programming interface (API) for rendering 2D and 3D computer graphics [80]. The API is typically used to interact with a GPU, to achieve hardware-accelerated rendering. OpenGL has been commonly applied in game development for 2D and 3D image rendering. A few libraries have been designed solely to produce an OpenGL-capable window include GLUT (later superseded by freeglut), GLEE and GLEW. There are about 150 distinct commands that users can specify the objects and operations to produce interactive 3D applications. To incorporate OpenGL into an existing MFC program, the header files that need to be added are “glew.h” and ”freeglut.h”. The libraries “glew32.lib” and “freeglut.lib” also need to be included into the additional library path. The commands would be ready to be used after including the library paths and header files. Below is an example of creating an OpenGL window and drawing a blue rectangular within the window, shown in Figure 35.

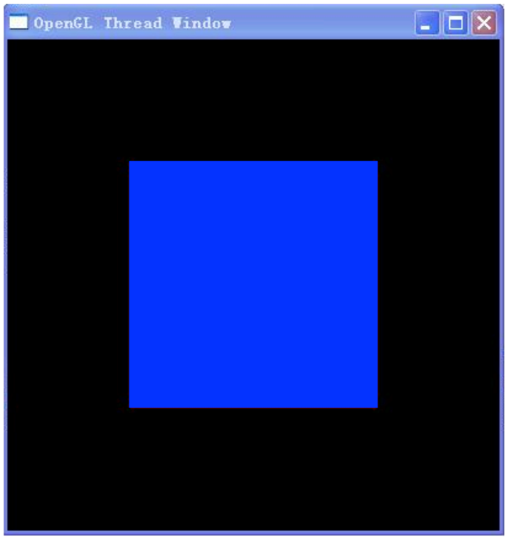

Figure 35. Example of creating an openGL window and draw a blue rectangular box within the window.

The freeglut library can be initialized by the command glutInit. glutInitDisplayMode defines the initial display mode; glutInitWindowPosition sets the center position of the window; glutInitWindowSize initializes the size of window in width and height; glutCreateWindow creates the window in openGL, glutDisplayFunc calls the display function defined separately, glutMainLoop enters the glut main processing loop. These commands are all predefined in glut library that are all ready for use and can be directly called for execution.

```
int main () {
        int argc = 1;
        char *argv[] = {“OpenGL Thread”};
        glutInit(&argc,argv);
        glutInitDisplayMode(GLUT_RGB|GLUT_SINGLE);
        glutInitWindowPosition(200,200);
```

```
    glutInitWindowSize(300,300);
    glutCreateWindow(“OpenGL Thread Window”);
    glutDisplayFunc(&Display);
    glutMainLoop();
}
```

The “Display” function that draws the rectangular shape with blue color is defined as:

```
void Display()
{
    glClear (GL_COLOR_BUFFER_BIT);
    glColor3f(1.0,0.0,0.0);
    glRectf(-0.5f,-0.5f,0.5f,0.5f);
    glFlush();
}
```

OpenGL library has been widely used for 2D image especially 3D volume rendering. The window creation, mouse clicking, image display functions were commands from freeglut library except the volume rendering kernel.

Materials and Methods

OpenGL was used as the platform of rendering 3D volume images. It was incorporated into the hybrid CPU-GPU acquisition and processing program described in Chapter 2. Freeglut library was used for window management including window creation, computer mouse position recognition, and volume display. The OpenGL windows were created in the initialization of data processing thread. Volume images were rendered and updated inside the while loop after a volume of 2D image processing is finished. There are three sub-windows created for displaying intensity, polarization and flow volume images respectively.

The overall flowchart of the hybrid CPU-GPU program for 2D data processing and volume rendering is shown in Figure 36. Acquired data from two cameras was copied from host memory to device memory for data processing. Raw data was converted from 16-bit unsigned integers to 32-bit floats for higher precision computation of both intensity and phase. This is especially important due to the dependency of phase when determining flow and phase retardation. The detected spectrum of one camera was “flipped” to coincide with the detected spectrum of the other camera. The reference spectra of the two channels, which were saved prior to imaging with only light reflecting from reference arm, were subtracted from the detected spectra. This was followed by linear interpolation and fast Fourier transform (FFT) by using CUFFT [75]. The two channels were then combined for dB conversion and gray-scale encoding of intensity image.

The complex results of the two channels after FFT were used to calculate phase retardation using simplified Stokes vector based method and flow using phase variance method. SNR threshold of 10dB was set so that pixels with SNR lower than 10dB will exhibit black color in volume rendering image. Processed 2D images of a volume were copied to 3D texture memory for volume rendering. The final intensity, polarization, and flow volumes were displayed on one OpenGL window containing three sub-windows [80-81].

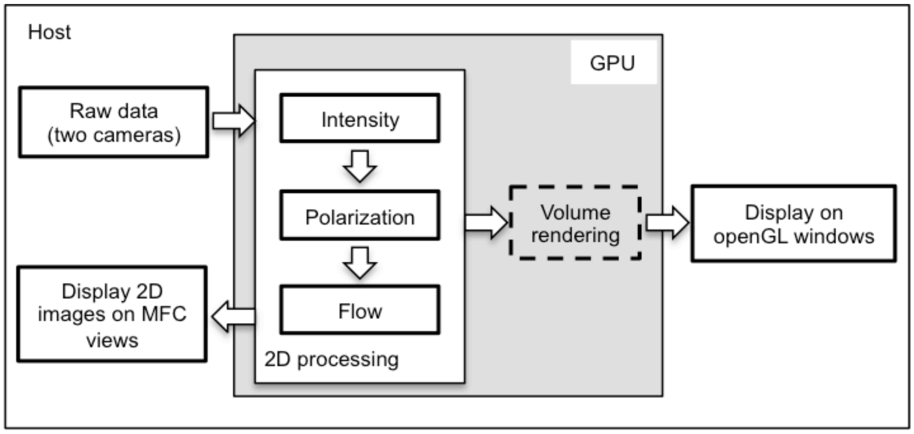

Figure 36. Flow chart of the 2D and 3D image processing

Figure 37 illustrates the flowchart of the volume rendering on OpenGL. Processed 2D images of the scanned volume were mapped to 3D texture memory on the GPU. A preset model-view matrix with size of 4 x 4 was used for ray casting which decided the relative position of the volume data and the image plane. The position changes during the mouse drag on the monitor were calculated to update the translation and rotation of the volumes. This mouse movement and clicks allow the user to change the model-view matrix directly and immediately.

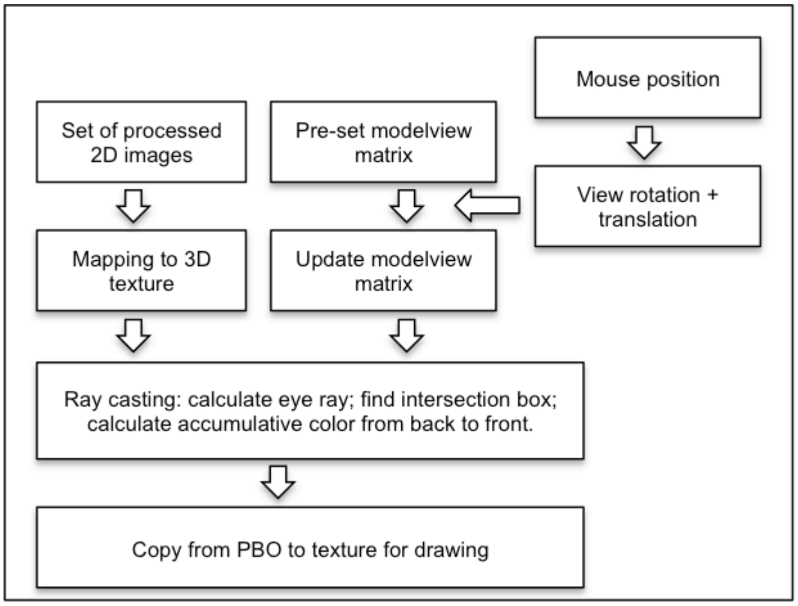

Figure 37. Flowchart of the 3D volume rendering

For 2D slices, model-view matrix and preset RGBA (red, green, blue, alpha) transfer function were used for volume ray casting. The first step of ray casting is calculating the eye rays that casting from volume data to 2D projected plane, then the intersection boxes along the eye rays are determined. The accumulative color value and opacity value of each pixel on the final 2D image are calculated using Eq. (36) and (37). The final volumes were copied from the pixel buffer object (PBO) to texture for display on the OpenGL windows. PBO allows fast pixel data transfer to and from GPU through direct memory access without CPU involved. The volume renderings of intensity, polarization and flow volumes were processed in longitudinal order. All volumes were rendered using the same model-view matrix to display identical volume projections. The intensity, polarization and flow volume image windows share the same model-view matrix.

A mouse dragging on anywhere in the window will simultaneously update the view projection of the three volume images such that the three volume images display complementary information from the same projection of the volume.

Figure 38 is the graphics user interface (GUI) of the real-time 2D and 3D processing program. It includes control panel on top left and camera spectrum display at bottom left. 2D images are displayed with gray scale color map on the top, and 3D volume images are displayed at bottom. For both rows, from left to right are intensity, polarization and flow images. The colormap in the 3D volume images can be changed according to user preference. The volume flow image can also be chosen to overlap on top of the volume intensity and polarization images.

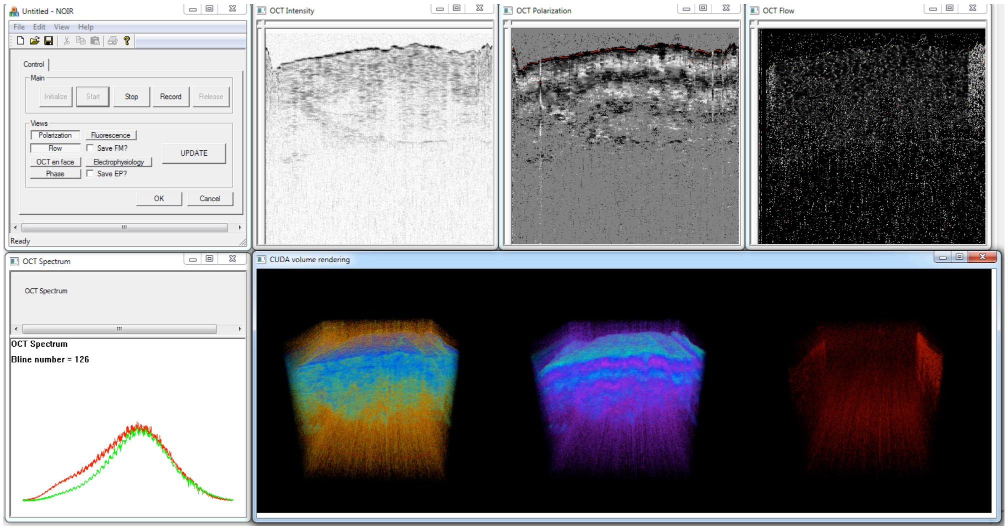

OCT Spectrum
Bline number = 126

Figure 38. Graphics user interface of the 2D and 3D image display. Top left is control panel, bottom left is spectrum display. The image views on top are 2D intensity, polarization and flow images from left to right. The image views at bottom are 3D intensity, polarization and flow images from left to right.

Results

In vivo imaging of human finger nail fold

We tested the volume rendering of intensity and polarization images by imaging a healthy human finger nail fold *in vivo*. The volume size of the sample was 256 A-scans (X) × 64 frames (Y) × 256 pixels (Z) (2.4mm × 2.4mm × 1mm). Figure 39 (a) and (b) include two snapshots from the real-time volume rendering video captured from the monitor using Camstasia Studio 7.0 (TechSmith Corporation). Each frame of processed volumes in y-axis was repeated four times to create volumetric cube (256 × 256 × 256 voxels). The size of the 2D image projected from 3D volume data was 512 × 512 pixels; 512 × 512 eye rays were used in the volume ray casting. User-controlled update of the viewing angle was demonstrated by clicking and dragging the mouse on any position of the volume on the monitor to update the model-view matrix. Structural and birefringence information of the finger nail fold was observed using the intensity and polarization volume renderings. Intensity and polarization views can be seen on the left and right sides, respectively, of each snapshot.

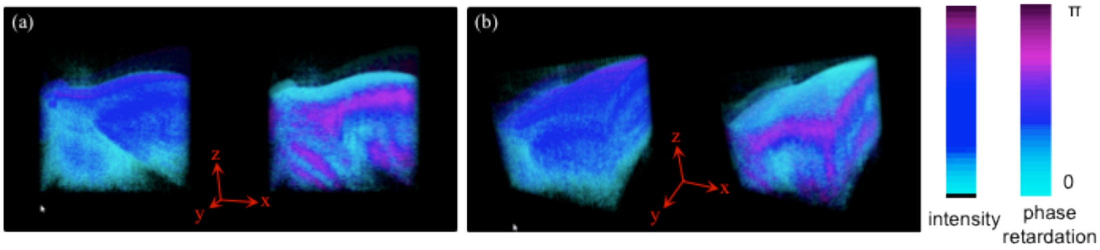

Figure 39. Screenshots of imaging a human finger nail fold *in vivo* with volume size of 256 A-scans (X) × 64 frames (Y) × 256 pixels (Z) (2.4mm × 2.4mm × 1mm).

Imaging of chicken muscle tissue to define burn progression

PS-OCT has the capability of characterizing normal and thermally injured tissue [57-58]. Thermally damaged skin shows a lower birefringence than normal skin. Two chicken muscle tissue samples were heated using a soldering iron tip at 720 °F and imaged with volume sizes of 256 A-scans (X) × 64 B-scans (Y) × 256 pixels (Z) (1.2mm × 1.2mm × 1mm) (Figure 40 (a) and (b), 2 vol/sec) and 512 A-scans (X) × 128 B-scans (Y) × 512 pixels (Z) (1.2mm × 1.2mm × 2mm) (Figure 40 (c) and (d), 0.5 vol/sec), respectively. Intensity volumes are on the left and polarization volumes are on right in the snapshots. In both Figure 40 (a) and (c), normal muscle tissue showed relatively uniform stripes in the polarization volumes and lower scattering in intensity volumes.

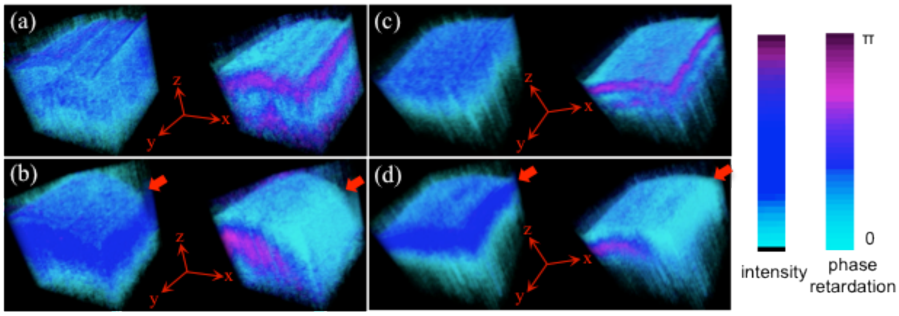

Figure 40. Screenshots of imaging chicken muscle tissue while heating from top right corner by soldering iron tip. (a) and (c) volume size of 256 A-scans (X) × 64 B-scans (Y) × 256 pixels (Z) (1.2mm × 1.2mm × 1mm). (b) and (d) volume size of 512 A-scans (X) × 128 B-scans (Y) × 512 pixels (Z) (1.2mm × 1.2mm × 2mm).

As heat began to propagate from the top right corner of the volume (red arrow in Figure 40 (b) and (d)), the affected tissue started losing birefringence and showed wider stripes in the polarization volume. As the heat continued to propagate, (Figure 40 (b) and (d)), the tissue nearest to the heat source lost all birefringence, which was displayed as cyan both on the surface and within the tissue in the polarization volume. The thermally damaged tissue showed higher scattering in the intensity volume (blue). The fast data processing speed and real-time volume rendering capability of the program enables observation of the burn damage in a volume wide.

Real-time evaluation of burn boundary and depth in chicken muscle tissue

PS-OCT is capable of evaluating skin burn injury as collagen in burn injured tissue denatures thus shows a lower skin birefringence value than normal skin [57-58,82]. However, previously reported studies of using PS-OCT to assess burn injury were all based on the 2D image from the real-time program, or visualization of 3D volume to identify the boundary through post-processed images [57-58,82]. The real-time volume rendering of affected area enables an immediate spatial view to identify the injury boundaries and depths.

Figure 41 are sets of volume images when imaging burn damaged chicken tissue with different burn injuries. Three regions of interest (ROI) of the chicken muscle tissue were thermally damaged using a soldering iron tip at 720 °F to heat for 1, 2, and 3 seconds respectively. The three ROIs were imaged with a volume size of 512 A-scans (X) × 128 B-scans (Y) × 512 pixels (Z) (2.4mm × 2.4mm × 2mm) with a volume update rate of 0.5 vol/sec. Figure 41 shows snapshots of the volume rendered images of the three ROIs with application of injury for 1 (a,b), 2 (c,d) and 3 (e,f) seconds. Figure 41(a), (c) and (e) display transverse views of the thermally damaged areas. Burns are observed with higher scattering in intensity image (blue) and lower birefringence (cyan) in the PS-OCT images. Positioning of the computer mouse to change adjustment of the view allowed optimally visualizing burn depth boundaries of the three ROIs. The increase in time exposure of heat applied onto the chicken muscle tissue resulted in an increase in range and depth of burn areas.

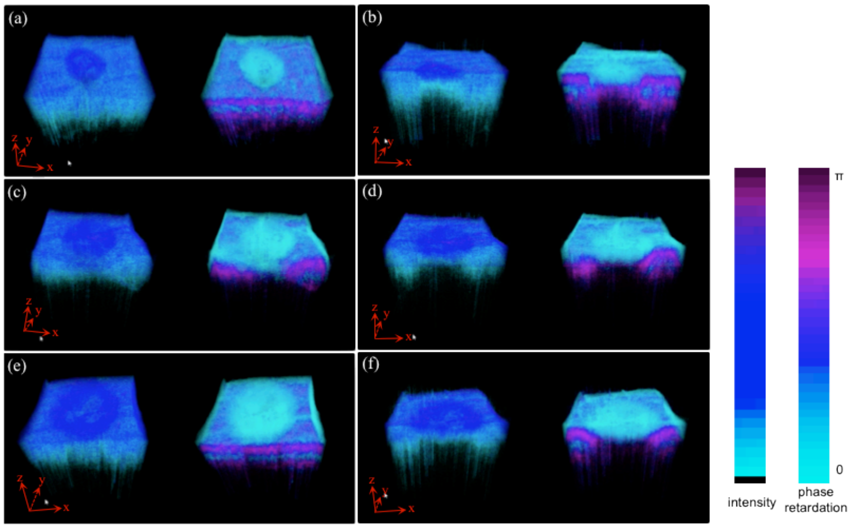

Figure 41. Visualization and identification of burn boundary in 3D volume images. (a) and (b), burn injury for 1 second; (c) and (d), burn injury for 2 seconds; (e) and (f), burn injury for 3 seconds.

Differentiation of arterial and venal flow

Doppler OCT measures blood flow by extracting Doppler frequency shift from the complex results of OCT data post FFT which is stated in detail in Chapter 1. The femoral area of a mouse was exposed for imaging *in vivo*. The mouse was anesthetized with two injections of a ketamine/xylazine combination (80 mg/kg ketamine, 10 mg/kg xylazine). Figure 42(a) and (b) depict two snapshots of the real-time recorded video during the imaging of the femoral artery and accompanying vein, and the surrounding tissues. Figure 42(a) was imaged with volume size of 256 A-scans (X) × 64 frames (Y) × 256 pixels (Z) (0.8mm × 0.8mm × 1mm) with a corresponding volume update rate of 2 vol/sec. Flow was overlaid onto the intensity and polarization images. The femoral artery blood flow (arrow 1) shows pulsation, whereas the femoral vein (arrow 2) has a much slower flow speed and its pulsation was too weak to detect. The blood vessel structures were slightly visible in intensity and polarization volume images (arrow 3,4). Figure 42(b) is a snapshot of the real-time recorded video with size of 512 A-scans (X) × 128 frames (Y) × 512 pixels (Z) (1.2 × 1.2mm × 2mm) with a rate of 0.5 vol/sec, four pulses were observed (arrow 1). The pulse rate of the artery calculated by comparing volume acquisition time, number of pulses and actual distance was 125 beats per minute; lower than that of the pulse rate of an un-anesthetized mouse.

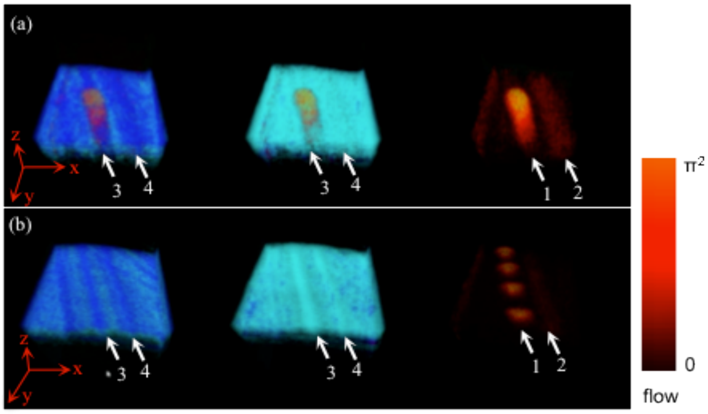

Figure 42. *In vivo* imaging of mouse femoral artery and vein: (a) volume size of 256 (X) × 64 (Y) × 256 (Z) (0.8mm × 0.8mm × 1mm)(media 4); (b) volume size of 512 (X) × 128 (Y) × 512 (Z) (1.2mm × 1.2mm × 2mm) (media 5). From left to right are intensity, polarization and flow volume images in both (a) and (b).

Discussions

Simultaneous volume rendering of intensity, polarization and flow images were demonstrated in our multi-functional SD-OCT system. The 2D processed images of the scanned volume are first copied to texture memory, then volume rendered using OpenGL and freeglut library. The intensity, polarization and flow volume images were displayed in three sub-windows that share the same model-view matrix to display the volumes with the same view perspective. The update rate of simultaneous volume renderings was 2 vol/sec and 0.5 vol/sec for volume sizes of 256 (X) × 64 (Y) × 256 (Z) and 512 (X) × 128 (Y) × 512 (Z), respectively. A human finger nail fold and chicken muscle tissue with thermal damage were imaged to demonstrate the capability of volume rendering of intensity and polarization images. Progression of thermal injury and birefringence loss of chicken muscle tissue was also identified. The femoral artery and vein and surrounding tissues of a mouse were imaged *in vivo* to depict structural information and pulsation flow was observed. Chicken muscle with different burn damage were imaged with burn boundary and depth visualized in the volume images.

Current system has only one GPU card for image processing, and the volume rendering was performed after one volume of data acquisition is done. Adding an additional GPU card to the system just for volume rendering that run parallel with data acquisition would increase the volume update rate. Current cameras acquire data at 45kHz, the volume data acquisition speed is only 2.7

volumes/second for volume size of 256 A-scans by 64 B-scans by 512 pixels. Upgrading the cameras to be the most recent line scan cameras with speed up to 92kHz would double the volume acquisition rate up to 5.4 volumes/second.

Chapter 4: Quantitative assessment of rat sciatic nerve injury using polarization-sensitive optical coherence tomography

Abstract

The necessity for surgical intervention for peripheral nerve damage often depends on the severity of the injury. The overall length of the repaired nerve is critical, and so such surgeries often involve differentiation of viable from damaged nerve by observation of scar formation, intraoperative electrophysiology, or imaging modalities such as computed tomography and magnetic resonance myelography. While these well-established techniques have led to great improvements in the field of acute nerve repair, they are not without flaw; waiting for scar formation introduces a delay before surgical intervention, intraoperative electrophysiology yields only bulk conduction properties of a nerve bundle with no cross-sectional differentiation, and CT and MR myelography can image only gross morphologies. Polarization-sensitive optical coherence tomography (PS-OCT) can provide a non-destructive quantitative optical assessment of nerve myelination by taking advantage of the higher degree of birefringence of myelin compared to the rest of a peripheral nerve. The preliminary study of imaging rat sciatic nerve with crush injury by PS-OCT showed axonal birefringence decreased post injury and increased with nerve repair. To further improve the experiment to reduce the variation caused by different animals, a longitudinal study was initiated and will be described in this chapter.

Introduction

The necessity of surgical intervention for peripheral nerve damage often depends on the severity of the injury. The injured nerve with the regrowth capability is not necessarily involved with surgery. Seddon divided the nerve injury into three grades: neuropraxia, axonotmesis and neurotmesis [83]. A nerve with mild injury can regrow quickly with macrophages to remove the debris [84]. The surrounding architechture like glial cells and Schwann cells provide trophic support for the regrowing axons [85-86]. At the extremely severe condition like at grade axonotmesis, nerve loses its continuity. There is no enough surrounding structure to support the nerve regrowth, such that injured nerve cannot regenerate [83,86]. The nerve graft requires a healthy nerve to be sacrificed and harvested from autologous body [87-88]. The nerve grafts containing viable Schwann cells (fresh nerve grafts) support axonal regeneration more efficiently than nerve grafts composed of basal lamina scaffolds only [87]. Thus minimal length of autologous nerve should be grafted.

In a lab situation, the gold standard for nerve assessment is histopathology, which accurately provides the degree of myelination but is an inherently destructive process. In a normal clinical setting, nerve viability is typically determined using a nerve conduction test, which gives functional grading of nerve injury, but does not provide quantitative information of myelination. Diagnosis of nerve injury at extreme cases of very mild or very severe injury is relatively easy. In the case of an intermediate injury, assessing which portions of an injured nerve require surgical intervention can be difficult and often require observation over some time [87]. The current methods for determining graft length are by observation over time and with intraoperative nerve conduction testing. Intraoperative nerve conduction testing is invasive by itself, it does not provide the quantitative degree of myelination [89]. It can only give difference when nerve injury conditions are very different.

Myelin and demyelination

Myelin acts as an electric insulator for neurons, it increases the membrane resistance and decreases capacitance. Myelin prevents the electrical current from dissipating into the surrounding medium and accelerates signal transmission in the axon. The propagation of action potential along myelinated axon is called salutatory conduction. The action potential ‘’jump’’ from one non-insulated axonal segment known as node of Ranvier to next node of Ranvier. Salutatory conduction largely increases the propagation speed of action potential transmission by 10 to 100 times compared to that of an unmyelinated axon [90-91].

Myelin is a lipid-protein lamellar membranous structure enveloping axons in both the central and peripheral nervous system of vertebrates. In the CNS, myelin is primarily found in white matter. The CNS myelin is produced by oligodendrocytes and is comprised of tightly compacted oligodendrocyte cell membranes, which are wrapped around the axon in a concentric lamellar fashion. In the PNS, the multilamella myelin membrane is formed by the differentiation of the plasma membrane of Schwann cells. Each intermodal segment of PNS myelin is connected to a single Schwann cell, whereas a single oligodentrocyte is connected to several tens of interdonal segments of CNS myelin. The intermodal distances are longer and the lamellar pediodicity is slightly larger in PNS than CNS myelin [92].

Myelin has high lipid-to-protein ratio: isolated myelin contains 70-80% lipids and 20-30% proteins. This relatively high lipid content and the particular characteristics of the lipids present in the sheath, provide the electrically insulating property required for the salutatory propagation of the nervous influx. At least 60% of the total proteins are glycoproteins (protein zero, peripheral myelin protein 22, myelin-associated glycoprotein etc), basic proteins (myelin basic protein, protein P2) occupy about 20-30%, and the rest are other proteins (nucleotide phosphodiesterase, proteolipid protein etc). The lipid portion of myelin is composed of cholesterol, galactolipids and phospholipids [93].

A number of diseases, such as multiple sclerosis and a range of leukodystrophies, are characterized by demyelination, or a loss of the myelin sheath around the axons. Demyelination of the CNS occurs in multiple sclerosis and Alzheimer’s disease [94]. In the PNS, demyelination may cause odd sensation in legs or arms, weakness of arms or legs, difficulty in coordinating movement. Myelin can be quantified either through its thickness or by g-ratio, which is the ratio between the diameter of axon and diameter of overall fiber [95].

Cause of peripheral nerve injury

The necessity of surgical intervention for peripheral nerve damage often depends on the severity of the injury. There are two predominant schemes that have been proposed for classification of peripheral nerve traumatic injuries, the Seddon and the Sunderland. Seddon divided injuries into three types: neurapraxia, axonotmesis and neurotmesis [83]. Neurapraxia is a comparatively mild injury with motor and sensory loss but there is no evidence of Wallerian degeneration, the nerve is intact but cannot transmit impulses. Recovery may occur within hours, days, weeks, or up to a few months. Axonotmesis is commonly seen in crush injuries. The axons and their myelin sheaths are broken, yet the surrounding stroma (i.e. the endoneurium, perineurium, and epineurium) remains partially or fully intact. Wallerian degeneration occurs, but subsequent axonal regrowth may proceed along the intact endoneurial tubes. Neurotmesis is the most severe type, which is seen with sharp injury, massive trauma, or severe traction with nerve rupture. There is loss of nerve trunk continuity with complete disruption of all supporting elements; reinnervation does not occur. Sunderland recognized five degrees of nerve injury. Sunderland’s first, second and fifth degree lesions correspond to Seddon’s neurapraxia, axonotmesis and neurotmesis. Sunderland adds two useful subclasses of axonotmesis. In a third degree lesion there is axonotmesis, with not only axonal but endoneurial discontinuity, while the perineurium is preserved. In a fourth degree lesion the internal structure is completely disrupted, only the epineurium is intact and nerve continuity is maintained purely by scar tissue. Seddon’s classification is more commonly used in the literature.

Wallerian degeneration and nerve regeneration

Wallerian degeneration is one of the most elementary and common reactions of the nervous system which occurs when the continuity of a nerve fiber is interrupted through traumatic, toxic, degenerative, ischemic or metabolic events. Wallerian degeneration concerns the axon, the myelin sheath and the myelin-forming cell, e.g., the Schwann cell, and macrophages in the peripheral nervous system [84]. The typical time course of Wallerian degeneration is as follows. Within 24 hours of injury, the nerve fiber loses its capacity to conduct action potentials as the axonal structures break down and Schwann cell cytoplasm is retracted from myelin sheath. Within 24-96 hours, there is intense Schwann cell differentiation and proliferation. This is accompanied by the disintegration of the myelin sheath, which is initially incorporated by Schwann cells. Hematogenous phagocytes are also recruited, which are thought to be important for facilitating the regrowth of regeneration axons into the distal nerve stump. 3-8 days after injury, degenerated myelin is removed by hematogenous or resident macrophages and Schwann cells. 10-20 days and later, Bungner bands are formed which induce regeneration by connecting the dissected nerve stumps [96].

Methods to assess peripheral nerve injury

In a lab situation, the gold standard for nerve assessment is histopathology, which accurately yields the degree of myelination but is an inherently destructive process. In a normal clinical setting, nerve viability is typically determined using a nerve conduction test, which yields functional grading but not a quantitative measure of myelination [89]. In research situation, scientists have tried to use imaging methods to study nerve myelination. MRI image the nerve myelin through the water content, which does not provide the quantitative information of degree of myelination [92]. J Cheng et al used CARS to image rat sciatic nerve and obtained the degree of myelination *in vivo* [97]. However, this method is prone to sampling error as the imaging field of view for CARS is limited to several axons at a time. Furthermore, the maximal imaging depth is limited to several hundred microns. These restrictions allow for incredibly detailed images of individual axons, but make assessment of a larger nerve problematic. Robert H. Miller et al have recently used PET assisted with florescent myelin-imaging agent termed CIC to detect myelin changes *in vivo* in mouse brain [98]. While this method allows for sensitive detection of neuronal myelin, it still requires introduction of an exogenous contrast agent. There remains a need for a clinically applicable method to non-invasively evaluate nerve viability endogenously and in real-time with sufficient quantitative resolution to predict whether a given section of nerve is capable of spontaneous repair or will require surgical intervention.

Preliminary study of peripheral nerve injury assessment by PS-OCT

A preliminary study of assessing peripheral nerve injury using PS-OCT was performed in Wellman center for Photomedicine by group PI. Sciatic nerve from Sprague Dawley rat (Charles River Laboratory) was used as the animal model. The nerve was imaged at an area of 5mm x 5mm with 2048 A-scans in each frame and 200 frames per volume.

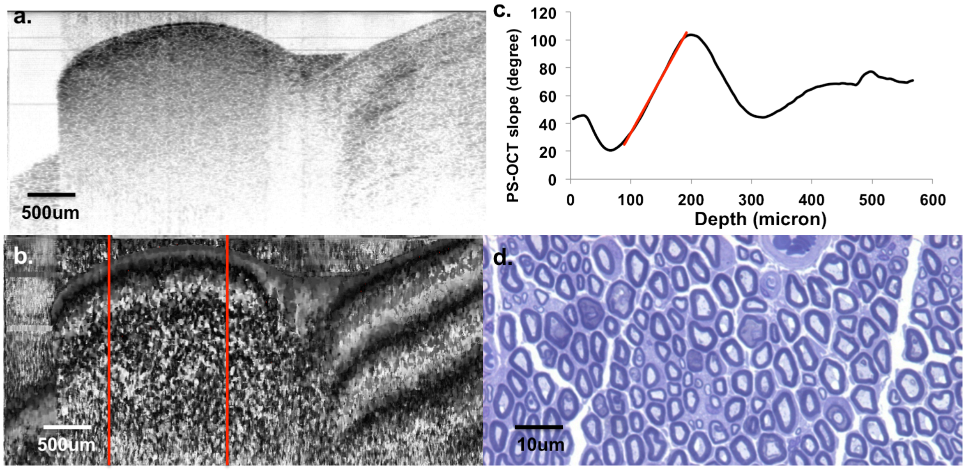

Figure 43. Normal nerve without crush injury (a) intensity image (b) polarization image (c) PS-OCT slope (d) histology result

Figure 43 is representative imaging result of sciatic nerve lying on top of muscle tissue. The images are (a) intensity image (b) accumulative phase retardation image relative to the surface of the sample polarization image (c) PS-OCT slope (d) histology result. The center 50% of each PS-OCT image were averaged to get a depth profile, and an averaged depth profile was computed from 20 2D images, shown in Figure 43 (c). PS-OCT slope was calculated by fitting the depth profile in the nerve region using first order linear regression. The

PS-OCT slope values were averaged within the volume to represent the birefringence of each volume. The averaged PS-OCT slope of the normal nerve shown in Figure 43 was 0.4328°/μm. Myelin was observed as blue circle structures in the histology result in Figure 43 (d).

Figure 44 is result from a transected nerve at two weeks post nerve transection. The nerve was transected and buried into the muscle tissue that nerve has no capability of self-repair. In the PS-OCT image, accumulative phase retardation is very small and nerve image is generally black. The computed PS-OCT slope is of 0.0554°/μm. The histology result shows barely myelin.

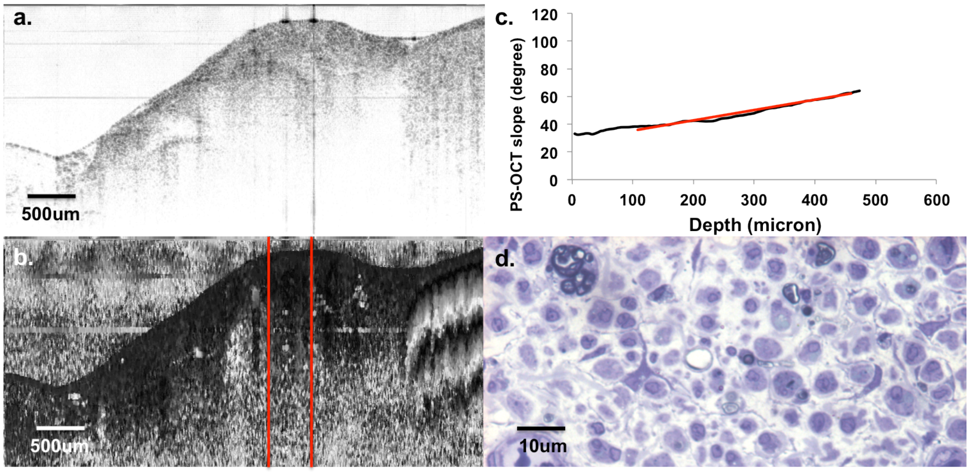

Figure 44. Transected nerve at two weeks (a) intensity image (b) polarization image (c) PS-OCT slope (d) histology result

PS-OCT slope was calculated for all the data set in the same way. Figure 45 is a graph showing PS-OCT slope changing with time post injury. Normal nerve has averaged PS-OCT slope value of 0.5114 degree/micron. The slope decreased to minimum value of 0.083 degree/micron at one week post injury and then gradually increased to averaged value of 0.25 degree/micron.

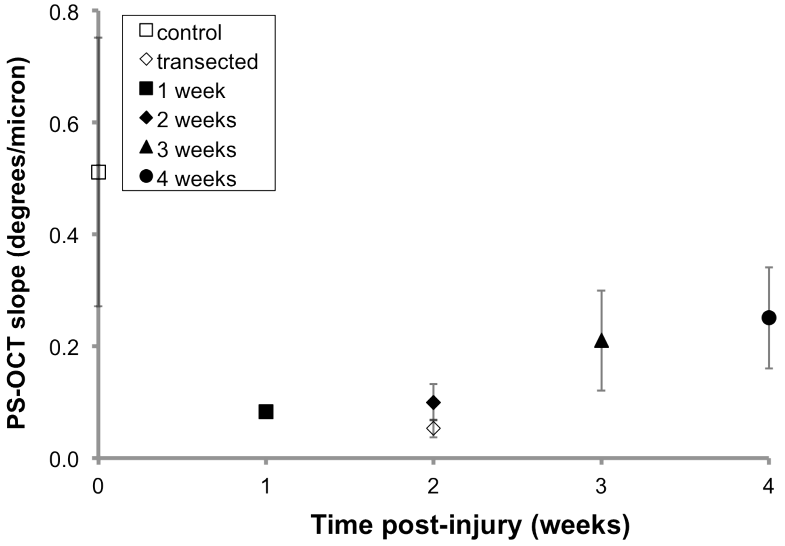

Figure 45. PS-OCT slope with time post crush injury

Table 4 is the p value calculated from different rat groups at different time point by two-sample student t test. The injured nerves (week1 to week4) showed significantly lower PS-OCT slope than that of normal nerves. However, no significant difference was observed in the first two weeks. Nerves had significantly higher birefringence in week 3 compared to week 2. However, it was not significantly different between week 3 and week 4.

Table 4. p value calculated among different animal groups

	Week1 (n1=7)	**Week2 (n2=6)**	**Week3 (n3=5)**	**Week4 (n4=7)**
Control (n=25)	<0.001	<0.0001	0.0002	0.0001
Week1		0.28	0.034	0.0026
Week2			0.0489	0.0037
Week3				0.47

n_1The preliminary study has shown that PS-OCT measured slope value decreased post injury and increased with nerve recovery. However, all the rats recovered from the preliminary study except the group receiving nerve transection. A longitudinal study was performed in order to further study if PS-OCT can have the potential of predict the capability of nerve self repair at earliest time point. There are several improvements proposed to perform the longitudinal study. First of all, the same animals will be imaged before and after injury to reduce the variation caused by different animals. Secondly, different groups of rats will receive different levels of crush injuries so that some of the rats can while some cannot recover from the injury. In this case, an earliest time point that can predict the nerve repair capability will be defined from PS-OCT results. Thirdly, a longitudinal study requires the time of exposing nerve as short as possible to keep a higher animal survival rate. The real-time multi-functional SD-OCT system described in first three chapters will be used to locate the suture marker more accurately.

Materials and Methods

Animal Model

University of California-Riverside Institutional Animal Care and Use Committee (UCR IACUC) approved all procedures described. We used the sciatic nerve of the Sprague Dawley male rat aged between 10 to 12 weeks (Harlan Laboratories, Livermore, CA) as a model for this study. This robust model allows for manipulation of a nerve of similar caliber and size to the human digital nerve and forms the basis of an objective assessment of motor function following injury.

Surgical procedures

The rats were anesthetized with pentobarbital sodium solution 40-50 mg/kg (<50mg/rat) using intraperitoneal (IP) injection. The pentobarbital sodium solution was prepared by diluting the pentobarbital sodium (Sigma Aldrich) with sterile water half an hour before experiment. After checking for absence of hindpaw withdraw reflex via toe pinch, the posterolateral aspect of the right hind limb and the left groin were shaved using electrical clippers. Hair removing lotion was additionally applied to the skin to remove hair thoroughly. Skin was prepared using alternating povido-iodine solution and 70% alcohol scrubs for a minimum of 3 scrubs each prior to start of surgery.

All surgical tools were sterilized using autoclave within 24 hours before experiment. A 5 cm longitudinal skin incision will be made in on the posterolateral aspect of the right hind limb. The muscles were separated to expose 3 cm of the sciatic nerve. Micro-suture marker was applied on the epineurium of nerve using 5-0 Vicryl suture. Figure 46. (a) is a picture of exposed nerve under microscope, the suture marker can be observed as two black dots on the nerve. The nerve was imaged using the multi-functional SD-OCT system. The crush injury was applied by a #5 jewelers forceps 1 cm distal to the exit of the nerve from the pelvis for 30 seconds with force of approximately 10 Newton on the forceps. The wound was washed with sterile saline and closed in layers with 5-0 Vicryl suture after imaging. Figure 46 (b) is a picture of the injury site after suturing. A neck cone was placed around the neck. The animals received buprenorphine (0.1-0.5 mg/kg, <0.5mg/rat) using subcutaneous (SQ) injection every 12 hours for three days for analgesia following the initial procedure. Baytril antibiotic will be also provided for the first three days (2.5mg/kg, <2.5mg/rat, SQ) after initial injury to prevent infection. Animals were monitored for resumption of ambulatory activity after recovery from general anesthesia and were returned to their housing cages.

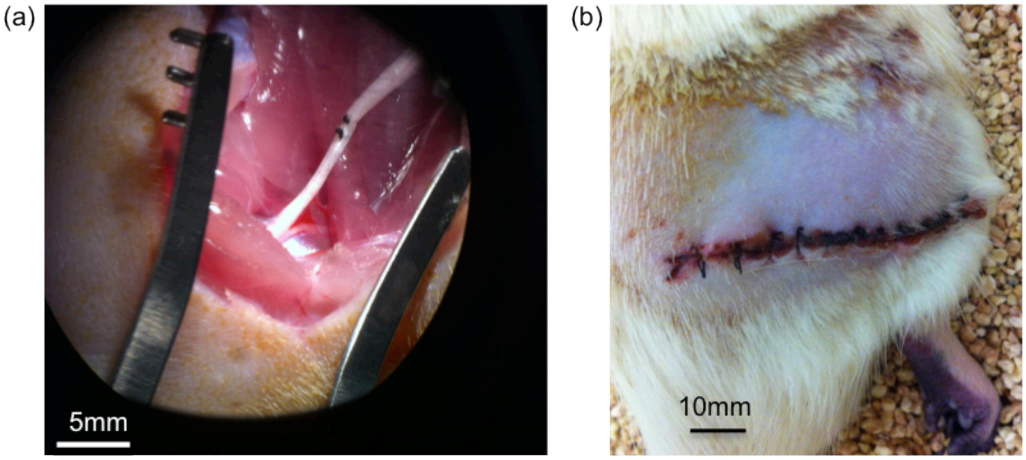

Figure 46. (a) Exposed sciatic nerve with suture marker (b) Injury site after suturing the skin together

Walking track analysis

After a rat was taken from vivarium to research lab, a walking track analysis was first performed before injury. Walking track analysis was performed before and following injury in order to calculate a sciatic function index as described by Bain and Mackinnon [98]. This functional analysis was undertaken to confirm recovery over time following sciatic nerve crush injury. To achieve this, the animal's hind paws were dipped in a dilute India ink solution before the alert animal was placed into a 10 x 100 cm corridor and allowed to walk into a darkened box of 20cm x 20cm as shown in Figure 47. Removable paper lining the corridor recorded each individual print.

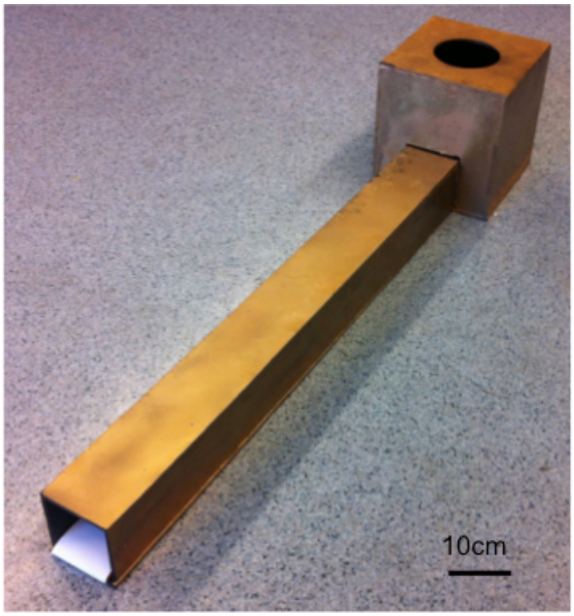

Figure 47. Corridor for walking track analysis

Three separate measurements of print length, toe-spread (distance between first and fifth toes), and intermediary toe-spread (distance between second and fourth toes) were taken from both left and right paws, with the non-operative left paw print used as a control. The sciatic function index was calculated using the formula as described by Bain and Mackinnon, with a value of zero representing normal function and more negative values up to -100, representing sciatic or functional impairment.

Polarization sensitive optical coherence tomography (PS-OCT)

To achieve real time imaging of the normal and injured sciatic nerve, the high-speed multi-functional spectral-domain optical coherence tomography system described in first three chapters was used. This system uses a broadband light source centered at 1.3μm and two InGaAs line scan cameras, with acquisition of individual axial scans up to 45,000 A-scans per second. The real-time volume rendering program presented in Chapter 3 was used for identifying the suture marker applied on the nerve. Data was acquired and visualized with four separate displays of spectrum, intensity, flow and polarization properties of the sample. The fast scanning axis of the sample beam was oriented perpendicular to the length of the nerve, to produce cross-sectional images composed of 2048 depth profiles spanning 2 mm. The imaging depth was 2 mm. A sequence of 200 such images was acquired over a 2 mm length for each imaged sample. Figure 48 is a picture showing while imaging rat sciatic nerve under the hand piece sample arm of the multi-functional SD-OCT system. The rat was placed on a plastic glass stage with heat isolation sheet to keep warm. Beneath the plastic glass stage, a 2D translational stage and two goniometer stages were used to adjust the lateral position and angle of the stage. Surgical tools were used to keep pushing away the muscles to expose nerve for imaging. The whole image session takes less than five minutes after locating the rat and exposing the nerve properly.

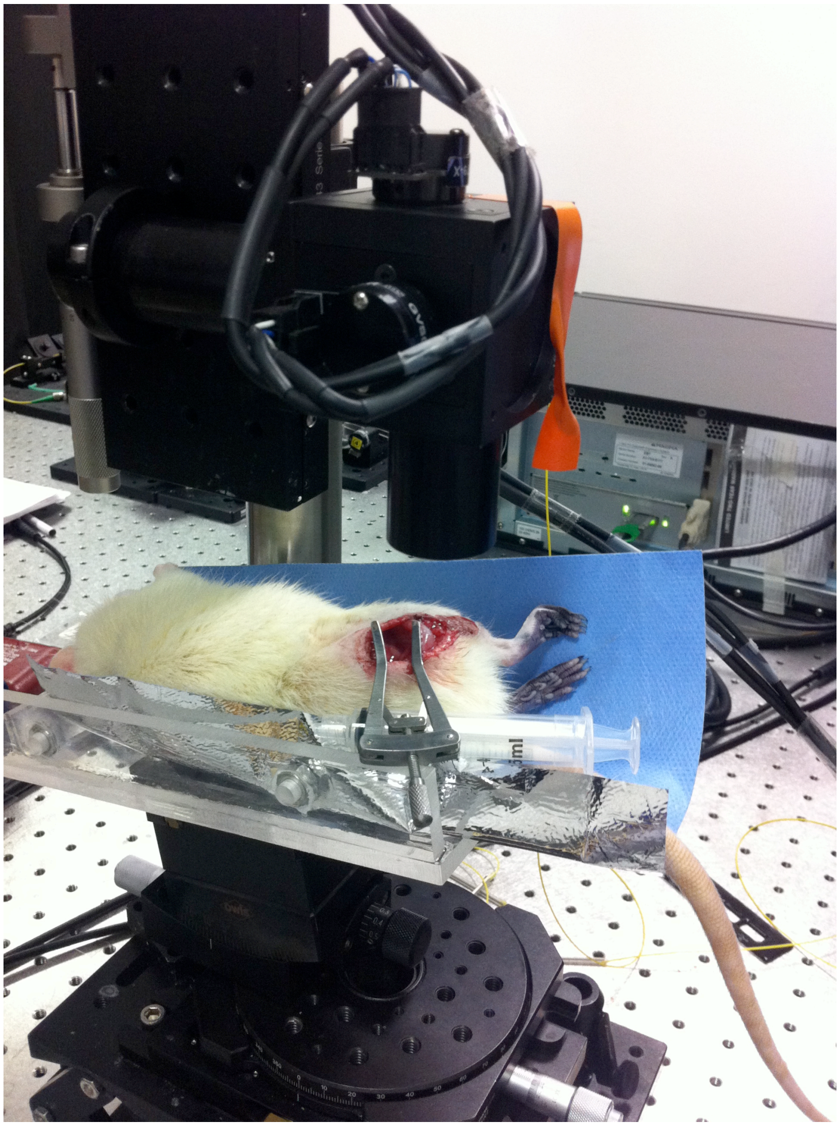

Figure 48. Imaging rat sciatic nerve with OCT system

Results

Functional analysis

The sciatic functional index (SFI) was calculated from print length (PL), toe-spread (TS, distance between first and fifth toes), and intermediary toe-spread (IS, distance between second and fourth toes) of both left (L) and right paws (R). Figure. 49 (a) and (b) are paw prints before and after injury respectively. Left paw print was used as control and crush injury was applied on right sciatic nerve. The factors were calculated as: print length factor (PLF)=(RPL – LPL)/LPL; toe spread factor (TSF)=(RTS – LTS)/LTS; intermediary toe spread factor (ITF)=(RIT – LIT)/LIT. The sciatic functional index (SFI) is calculated as: SFI=-38.3xPLF+109.5xTSF+13.3xITF–8.8.

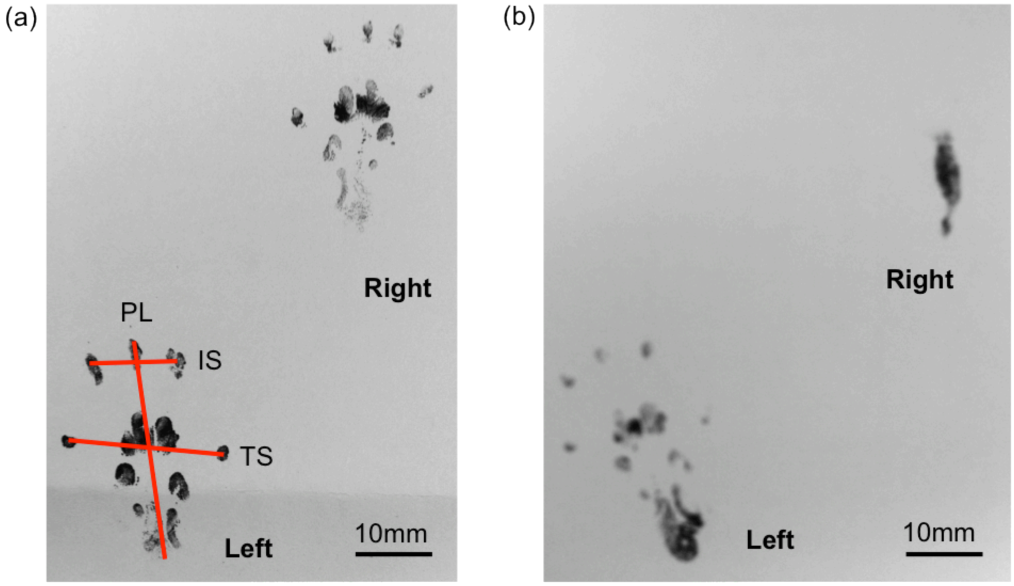

Figure 49. Walking track of a rat (a) before injury and (b) two days post injury

The calculated SFI for normal condition before crush injury was -6, which is close to zero represents normal function. The SFI of the same rat at two days post injury was calculated as -100, representing sciatic or functional impairment.

Real-time 3D volume rendering

The real-time volume rendering program described in Chapter 3 was used to identify the suture marker post injury for locating the injury site more accurately. The volume size was 2.7mm x 2.7mm x 2mm (256 A-scans x 64 B-scans x 256 pixels), resulted in a volume update rate of 2 volumes/second. The real-time volume rendering program allows visualization of nerve structure within the scanning volume instantaneously. The nerve was observed as cylinder structure in Figure 50 (a) and (b). In both screenshots, intensity volume was on the left and polarization volume was on the right.

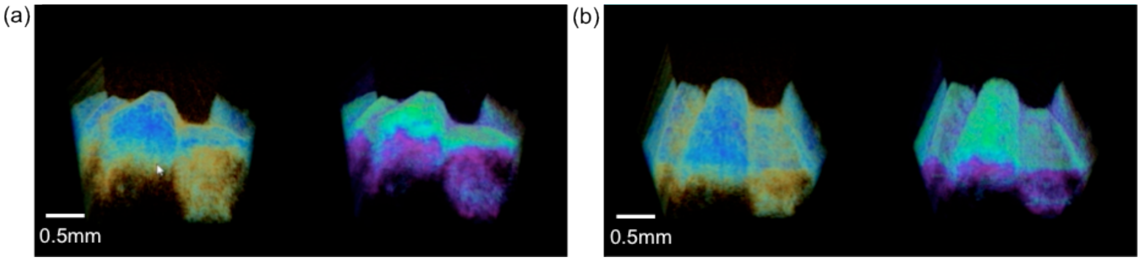

Figure 50. (a) and (b): real-time volume rendering of rat sciatic nerve during *in vivo* imaging.

Figure 50 (a) and (b) are screenshots of real-time volume rendering the nerve with suture marker at different projection views. The volume size was 4.5mm x 4.5mm x 2mm (256 A-scans x 64 B-scans x 256 pixels) with volume update rate of 2 volumes/second. The suture markers were identified in the volume images and indicated by arrows.

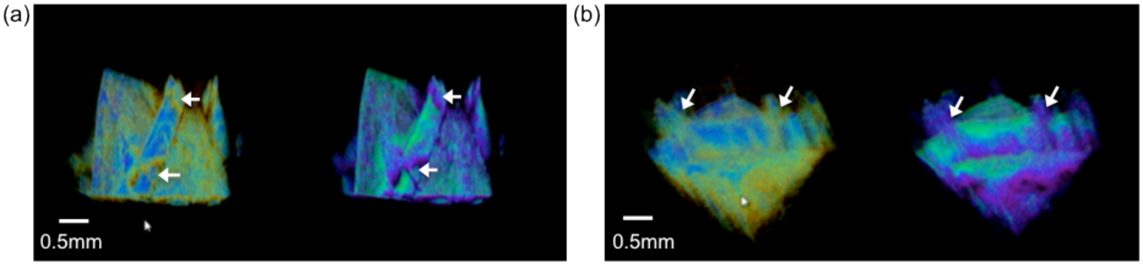

Figure 51. (a) and (b): real-time volume rendering of nerve with suture marker visualized in the volume images

The volume size was set to be 256(X) x 64(Y) x 256(Z) for fast volume rendering to adjust the imaging region and search for the suture marker. After the suture marker was identified from the scanning volume, the volume size was set to be 2048(X) x 200(Y) x 512(Z) to save higher resolution data for post-processing.

PS-OCT results

Birefringent tissue regions are detected in PS-OCT by depth-dependent changes in the cumulative phase retardation experienced by different polarization states of the reflected light. With an increase in tissue birefringence, more rapid changes in both phase retardation and polarization state will be detected. The cumulative phase retardation was expressed as an angle on a gray scale from black (0^o) to white (180^o). These angles were determined using simplified Stokes vector based method described in Chapter 1. The nerve was imaged with 200 2D frames that have 2048 A-scans in horizontally and 512 pixels vertically in each frame. The scanned volume physical size was 2mm x 2mm x 2mm.

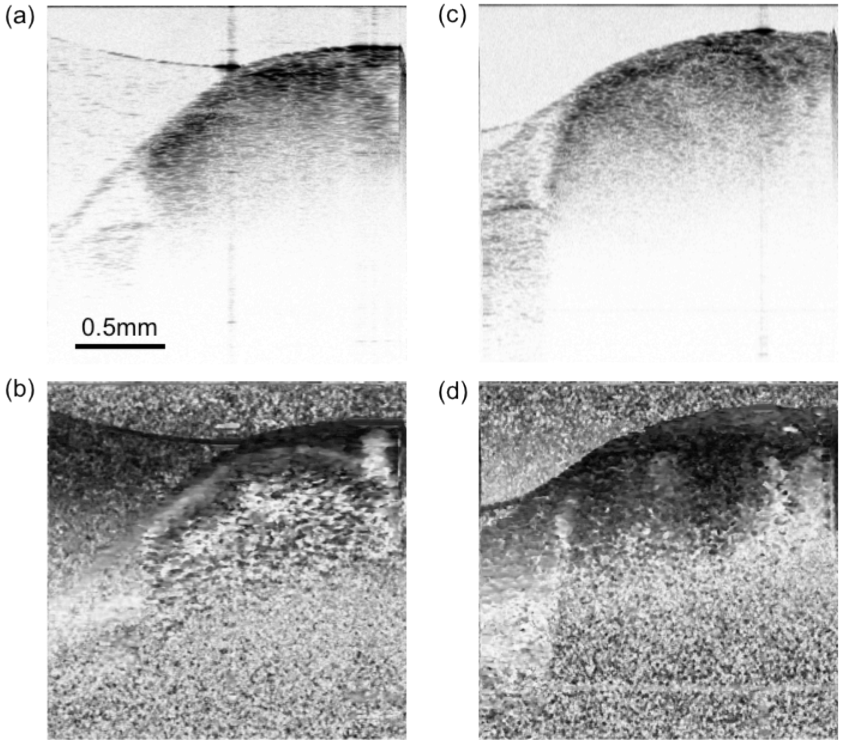

Figure 52. 2D intensity and PS-OCT images of nerve (a) intensity, control nerve; (b) PS-OCT, control nerve; (c) intensity, 2 days post injury; (d) PS-OCT image, 2 days post injury.

Figure 52 (a) and (b) are 2D cross-sectional intensity and phase retardation images of a normal nerve before crush injury was applied. The cumulative phase retardation in the normal nerve had a fast transition from 0^o (black) to 180^o (white). Figure 52 (c) and (d) are intensity and PS-OCT images of the same nerve at two days post injury. In the PS-OCT image, the nerve degenerated post injury and resulted in low birefringence that exhibits generally black color (cumulative phase retardation close to 0^o) in the nerve.

In each individual image, the average phase retardation as a function of depth was determined within the central 50% of regions identified as sciatic nerve. The slope of the corresponding graphs was taken as the birefringence of the nerve. A mean of these values was calculated to provide a single unit of depth-resolved birefringence per volume scanned. This phase retardation depth profile was averaged for every 20 images in the volume.

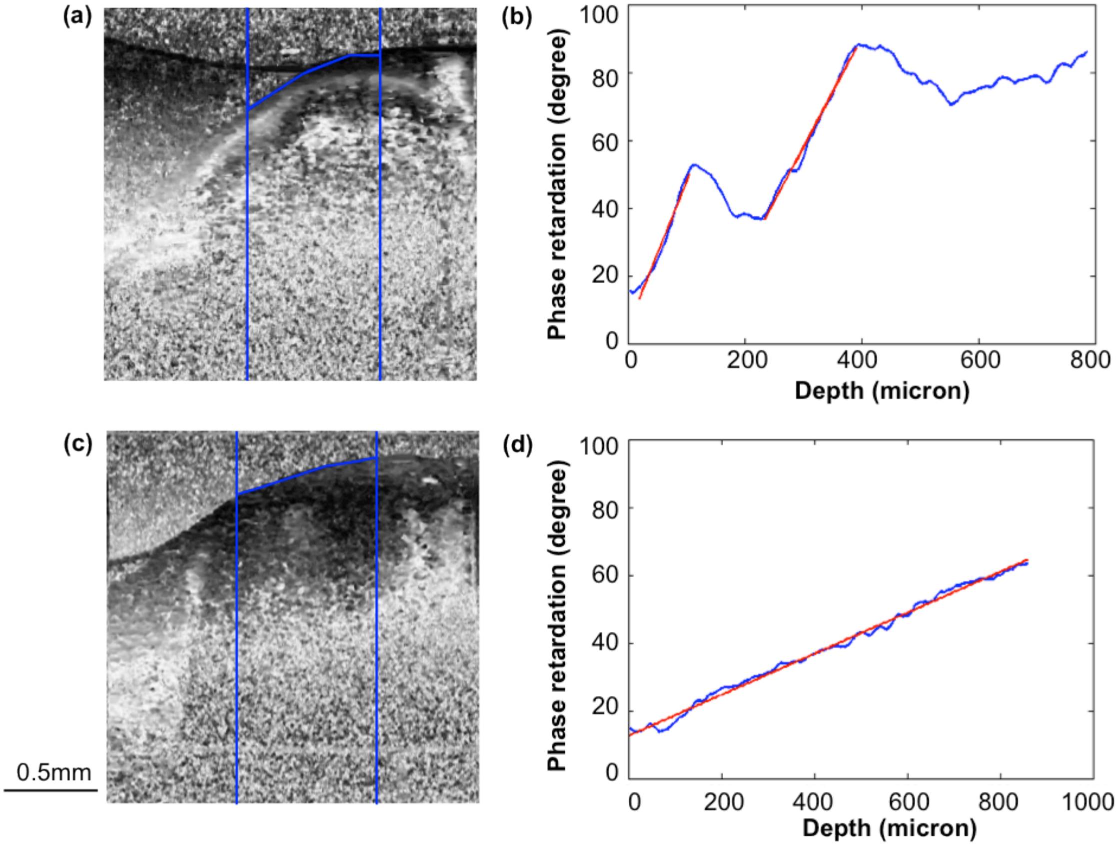

Figure 53. Averaged phase retardation changing along with depth (a) normal nerve (slope1: 0.42 degree/micron; slope 2: 0.32 degree/micron) (b) injured nerve (slope: 0.06 degree/micron)

Figure 53 (a) is 2D PS-OCT image of a normal nerve and (b) is the averaged phase retardation along with depth for 20 images. First order linear regression was used to fit the two increasing slopes, the slopes values were obtained as 0.42 degree/micron and 0.32 degree/micron as the tissue birefringence value in these two regions. Similarly, Figure 52 (d) is the averaged phase retardation along depth from Figure 52 (c) at 2days post injury. An injured nerve has much lower birefringence that is 0.06 degree/micron.

Discussions

The necessity of surgical intervention on an injured nerve can be difficult and often requires observation over time. Currently graft length is determined by observation and with intraoperative nerve conduction testing. Intraoperative nerve conduction testing only finds difference at extreme cases of very mild or very severe injury. Quantitatively evaluating the nerve health (degree of myelination) and predict whether a given section of nerve can repair from surgery or not is of great clinical significance. From the preliminary study performed by the group, the birefringence value calculated from PS-OCT images of normal nerves showed significantly lower value than that of injured nerves. The PS-OCT derived birefringence also increased with nerve repair through time. In order to further study on the peripheral nerve degeneration and regeneration using PS-OCT, a longitudinal study was proposed and initiated.

This longitudinal study was initiated with four rats in this study considering the limited animal training experience of the researcher. Only one rat survived after the initial surgical procedure. The rat sciatic nerve on the right hind leg was exposed with surgery incision on the skin. Suture marker was applied on the epineurium of nerve to mark the position of crush injury. The nerve was imaged before crush injury and 2 days post injury. The real-time volume rendering program was used for identifying the suture marker in real-time volume images to keep consistent imaging site through time. The PS-OCT images of the injured nerve showed lower birefringence (0.06 degree/micron) than before the injury

(0.42 degree/micron). Functional analysis from a walking track analysis showed total impairment at two days post injury. This rat is still being housed in UCR vivarium for longer observation at the time point of writing this thesis.

The future work includes more number of animal samples for longer time observation. Different grades of injuries should be applied on different animals for different recovery rate. Histology will be also incorporated to examine the degree of myelination at different time point.

Chapter 5: Study of human skin photo-aging, factors of age, gender and skin type

Abstract

Intrinsic aging and photo aging are of much significance in science, medical and cosmetic fields. Collagen is very important connective tissue in the skin to keep elasticity. The amount of collagen decreases in the aging process thus results in wrinkles. It is known long period of sun exposure accelerates the skin aging process and reduces the amount of collagen in skin. Tissue with well organized fiber structure such as muscle, collagen and tendon exhibit birefringence, which causes phase retardation that can be measured from a PS-OCT system. The dermal birefringence measured from PS-OCT is directly related to the density and organization of collagen and elastin. This project is to assess the intrinsic aging and photo aging of normal human skin through imaging the sun-exposed area (face) and sun-protected area (inner upper arm) from adult participants with different ages. Two age groups of volunteers were recruited into this study, including younger age group (18-35 years old) and older age group (55 and above). The volunteers were also recruited in gender (male and female), as well as all skin types (Fitzpatrick scale I-VI).

Introduction

Skin aging is a highly complex process that is not fully understood yet. It is of particular interest as increasing expectancy on life, accompanying with booming of skin care and cosmetic industry. Clinical, histological and physiological studies reported that old skin is more vulnerable to environmental injuries and certain diseases [100]. Thus studying the biologic process of aging in the skin is very significant and itself is a major clinical problem. Cutaneous aging includes two independent biological processes, intrinsic aging and photo-aging [101-102].

Intrinsic aging and photo aging

The clinical definition of intrinsically aged skin is atrophic that may result in prominence of vasculature, transparent quality and loss of elasticity [101]. There is considerable decrease in vascularity and dermal thickness. The number and biosynthetic capacity of fibroblasts also decrease that results in delayed wound healing. Fine dermal elastic fibers coarsen with age and then disappear. Intrinsically aged skin is usually found in sun-protected areas. In old sun-protected skin, there are relatively subtle and consist primarily of laxity, fine wrinkling, and a variety of benign neoplasms [102].

Photo-aging is extrinsic aging that primarily arises from long term exposure to UV-light. Approximately 80% of facial skin ageing is attributed to UV-exposure. Other relevant exogenous factors are exposure to tobacco smoke, airborne particulate matter, infrared radiation, ozone and malnutrition [103]. The biological effects of UV-radiation are based on light absorption in chromophores and the subsequent conversion of light energy in chemical reactions. UVA/UVB-radiation contributes to biological effects, resulting in skin ageing and photocarcinogenesis. Short wave UVB is mainly absorbed in the epidermis, generating DNA-damage by forming photocarcinogenic cyclobutane pyrimidine dimers (CPDs) and 6,4-photoproducts. UVA-light is exceptionally relevant in photo aging because of its high penetration depth. It is absorbed by cellular chromophores, such as urocanic acid, melanin precursors and riboflavin. These light-exposed chromophores generates ROS, which damage lipids, proteins and DNA. UVA-light [104].

The study on photo aging is of great dermatologic importance because of the considered cosmetic and psychosocial distress caused to older persons, as well as its presumably etiologic relationship to skin cancer [104]. Photo aging is responsible for the majority of unwanted age-associated changes in the skin's appearance. This includes skin coarseness, wrinkles, sallow color, telangiectasia, irregular pigmentation, and a variety of benign, premalignant, and malignant neoplasms [101-104].

Collagen and elastin change during aging

The connective tissue of the skin is mostly composed of collagen and elastin. Collagen is the primary structural component of the dermis and found to be most abundant protein in human body. Collage makes up 70-80% of the dry weight in the skin and supports the dermis its mechanical and structural integrity [105]. The structural proteins and main components of the skin deteriorate over time, resulting in the cutaneous signs of ageing. In aged skin, collagen is characterized by thickened fibrils, and appears to be in disarray in comparison to the pattern observed in younger skin. In addition, lower numbers of collagen are synthesized in aged skin. In young skin, the skin collagen is composed of 80% collagen type I and 15% of collagen type III. As skin ages, the percentage of collagen type I decreases and percentage of collagen type III increases. The overall collagen content per unit area of skin surface is known to decrease approximately 1%/year. Collagen I levels have been shown to be reduced by 59% in irradiated skin, was found to be linked to the extent of photodamage [106].

Elastin is a minor component of the dermis that accounts for 2-4% of the extracellular matrix, and has an important function of providing skin elasticity [107]. The primary change in the aged dermis is the architecture of the collagen and elastin networks. Both collagen and elastic fibers show marked alterations with age in their three-dimensional arrangements. Elastin gene expression markedly reduces by age and results in progressive disappearance of elastic tissue in the papillary dermis [107]. The individual elastic fibers show signs of elastolysis. UV exposure induces a thickening and coiling of elastic fibers in the papillary dermis. Elastic fibers in UV-exposed skin has revealed a reduction in the number of microfibrils and increases in interfibrillar areas. Skin elasticity is gradually lost with age and thus sagging skin is observed in elderly skin [107].

Non-invasive evaluation of skin aging

Quantitative assessment of the changes associated with chronologic aging and photo aging of human skin is critical. First, it allows informed speculation about the biologic, biochemical, and ultimately genetic mechanisms of aging. Second, the data gathered from studies allows the establishment of age-specific norms and reproducible objective, individual baseline determinations. These measurements, in turn, allow meaningful studies of interventions intended to alter the rate of skin aging [101-102].

It is very significant to evaluate the degree of dermal degeneration non-invasively when it comes across the diagnosis of intrinsic aging and photo aging. Ultrasound tomography, confocal microscopy, two-photon microscopy and optical coherence tomography have been used for non-invasive evaluation of the internal structures of the human skin. Confocal microscopy and two-photon microscopy have higher spatial resolution than OCT, however, their measurable depth range and working distance is limited [2]. Ultrasound tomography has better imaging depth but its spatial resolution and image contrast are not sufficient to distinguish the individual structures of the skin [109]. OCT has better resolution than ultrasound tomography and deeper imaging depth than confocal microscopy and two-photon microscopy. In addition, OCT images have similar size and geometry to that of histology images. The skin structures like stratum corneum, dermal-epidermal junction, infundibula, and follicles are evident in OCT images [1,110-111]. In the dermis, collagen forms strongly oriented fibers that results in birefringence, which can be measured by PS-OCT. PS-OCT has been applied on dermatology to evaluate the collagen denaturation on skin burn injury, scars and wound healing [57-58, 82, 112]. PS-OCT was previously applied on imaging younger skin and older skin which showed a lower birefringence in older skin [113]. However, there were only eleven male subjects with skin type III to IV included in the study. The goal is to include more volunteers with both genders (male and female) as well as all skin types (Fitzpatrick scale I-VI) into the study to obtain statistically significant results.

Materials and Methods

Study protocol and volunteer recruitment

The system that used for this study is the multi-functional SD-OCT system [65]. The incident light from diode lasers at 1300nm has power of 6mW onto the skin, scanning imaging area by 5mm by 5mm contributes to an energy density of 0.024W/cm^2. This is below the maximum permissible exposure (MPE) of 1W/cm^2 required by American Standards for the Safe Use of Lasers (ANSIZ136,1-2000). The protocol of using this system to image human skin was reviewed and approved by UCR laser safety office. A separate protocol of recruiting human subjects on UCR campus for this skin imaging study was documented and approved by UCR human research review board (HRRB). There were two age groups of volunteers recruited into this study, younger age group (18-35 year old) and older age group (55 years old and above). Both male and female subjects were included into these two main groups, including all skin types (Fitzpatrick scale I-VI). There were 37 volunteers recruited and image in this study so far. Each volunteer was imaged on four region of interests (ROIs) including forehead, temple, cheek and inner upper arm.

Imaging system and experimental procedures

The system was described in Chapter 1 in detail. The light source is centered at 1298 nm with 120nm bandwidth and outputting power of 16 mW. A homemade hand-piece scanner is connected to the system by an optic fiber. The sample arm scanner includes a fiber collimator, two Galva mounted mirrors and a 50mm focus lens. The two Galva mounted mirrors scan the light onto the sample laterally in 2 dimensions resulting in scanning area of 5mm by 5mm. The light onto the sample is 6mW and focused by the focus lens. Figure 54 is a demonstration of imaging on the forehead of a volunteer using the system. Each volunteer was required to wear laser goggles to prevent possible light into the eyes. A shutter was placed between the fiber collimator and Galva mounted mirrors to manually block the output light during switching ROIs or not imaging. As described in Chapter 2, this shutter was also used to take a reference spectrum for data processing.

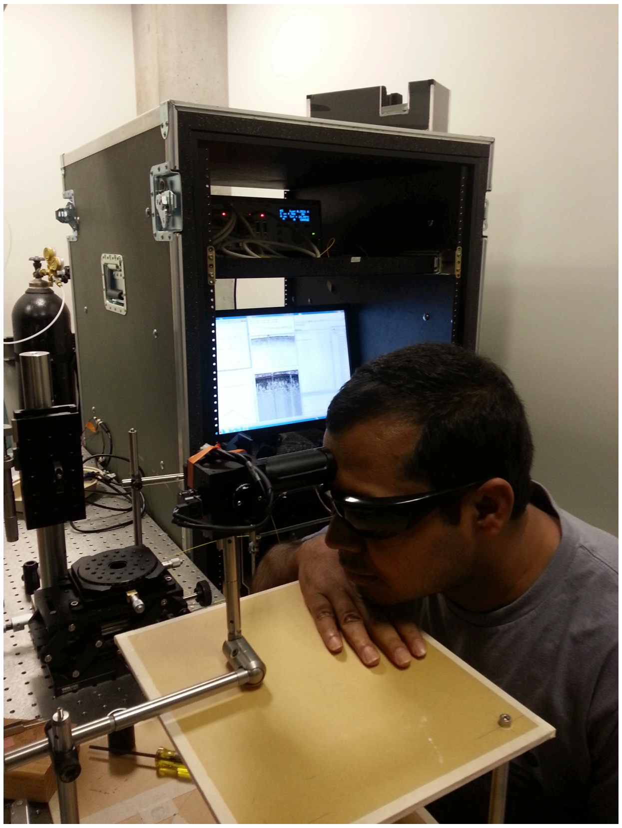

Figure 54. Imaging forehead skin of a volunteer using multi-functional SD-OCT system, the intensity and polarization images of scanned area were displayed on the monitor real-time.

Data acquisition speed was set to be 15kHz in order to get stronger sample signal resulting from longer integration time. Each ROI was imaged as a volume that contains 200 frames and 2048 A-lines per frame. The data acquisition and save time per ROI is 28 seconds. The total data acquisition time of four ROIs per volunteer is less than 5 minutes including the time to change ROIs and file names of saved data. In order to stabilize and ensure the imaging area is at the focus, a ring was placed at the focus plane of the scanner. This ring was sterilized by 70% alcohol pad before imaging each subject. The intensity and polarization images of scanned area were displayed in real-time on the monitor. The real-time image processing and display helps with ensuring the image area within focus as well as looking for homogenous region for imaging.

Participants were confirmed with consent prior to this study. The basic information such as age and daily time exposed sunlight were informed and recorded anonymously. Collected data is digitized and saved into the experimental computer as binary numbers for post-processing. Six ROIs on the arm and forearm were labeled and imaged at different time (morning, evening and next day), as well as before and after applying makeup including moisturizer, foundation and blush. The measured birefringence values have small standard deviation that is less than 10% of average value for above conditions. There were overall 37 volunteers recruited in this study so far, including 24 younger male, 13 younger female, 2 older male and 2 older female subjects.

Results

Intensity and polarization images of each imaging data set were both computed using MATLAB and saved on hard drive. Figure 55 (a) and (b) are representative intensity and polarization images of cheek of an older subject at 60 years old. Figure 55 (c) and (d) are intensity and polarization images of cheek from a younger subject at 23 years old. The intensity image is based on the amount of light back scattered within the skin tissue. The epidermis is observed as a thin layer from intensity image of the younger subject, while it is very thin that is not discernible from dermis in the older subject. This corresponds to other studies that epidermis layer gets thinner during aging process [114]. The younger subject skin shows higher birefringence thus accumulative phase retardation has fast transition in depth. The older subject skin image is generally darker, and fewer areas are birefringent below the skin surface.

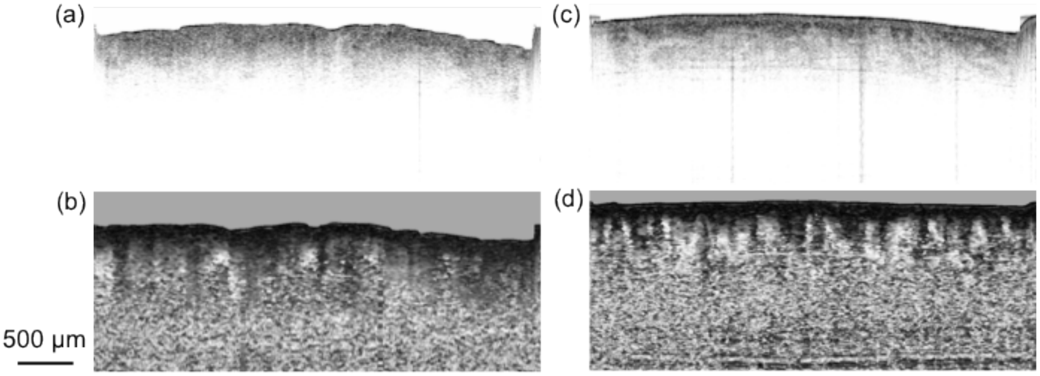

Figure 55. Intensity and polarization images of an older and younger male subjects on the cheek

Figure 56 is 2D cross-sectional polarization images of a 60 years old volunteer (a-d) and a 23 year old male volunteer (e-f). From top to down, the imaging regions are cheek, temple, forehead and inner upper arm. Lower birefringence was clearly observed from the 2D images at sun exposed areas including cheek, temple, and forehead. The difference at sun protected area (inner upper) arm is not as significant as sun exposed area, which is consistent with reported research [113].

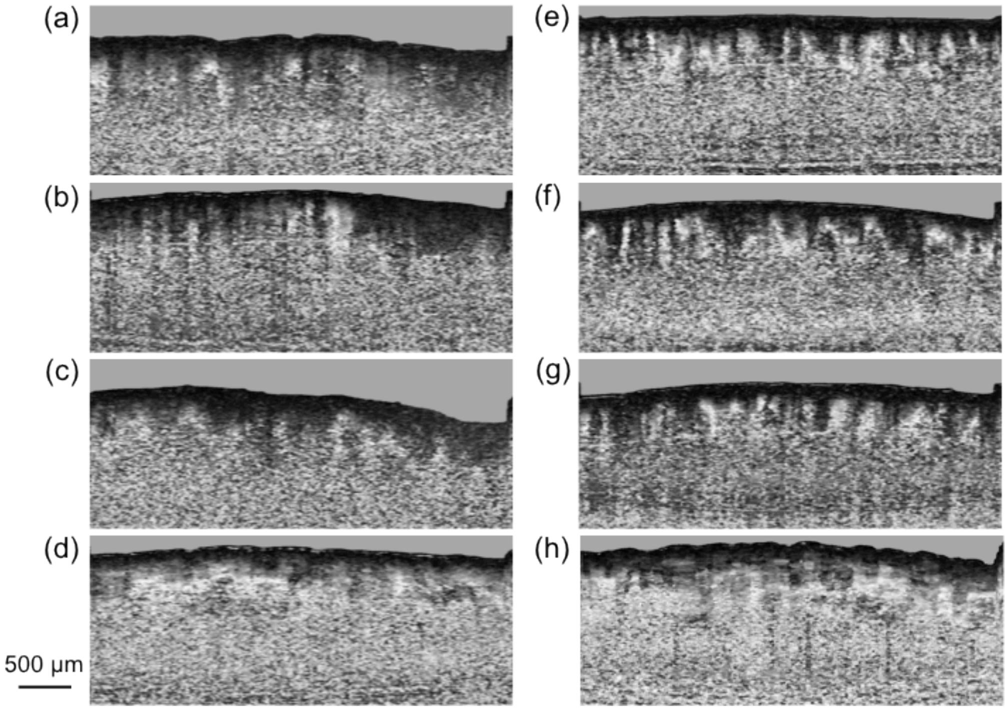

Figure 56. 2D cross-sectional polarization images of (a-d) a 60 year old male person and (e-h) a 23 year old male person. The imaging regions are cheek, temple, forehead, inner upper arm from top to down.

Each imaging area was imaged as a volume composed of 200 frames, and each frame has 2048 A-scans. Visualization of *en face* image would allow us to see the map of birefringence in the volume. Figure 57 shows representative *en* *face* polarization (top) and intensity (bottom) images of cheek area from a young male (a, e), a young female (b, f), an old male (c, g), and an old female (d, h) subjects. The *en face* image depth was about 350 microns below the skin surface. The *en face* polarization images of both younger male and younger female showed highly birefringent tissue around non-birefringent areas. The arrows indicate the non-birefringent tissues that might be hair follicles or holes on the skin. The same spots labeled on polarization images were indicated in intensity images as well where showing lower light scattering. The birefringent and non-birefringent structures are very organized in the polarization images of younger subjects. The *en face* images from the older male and older female subject showed lower birefringence map. The *en face* polarization images from the older subject showed less organization. The boundaries of the holes are not so well-defined and surrounding tissue show less birefringence.

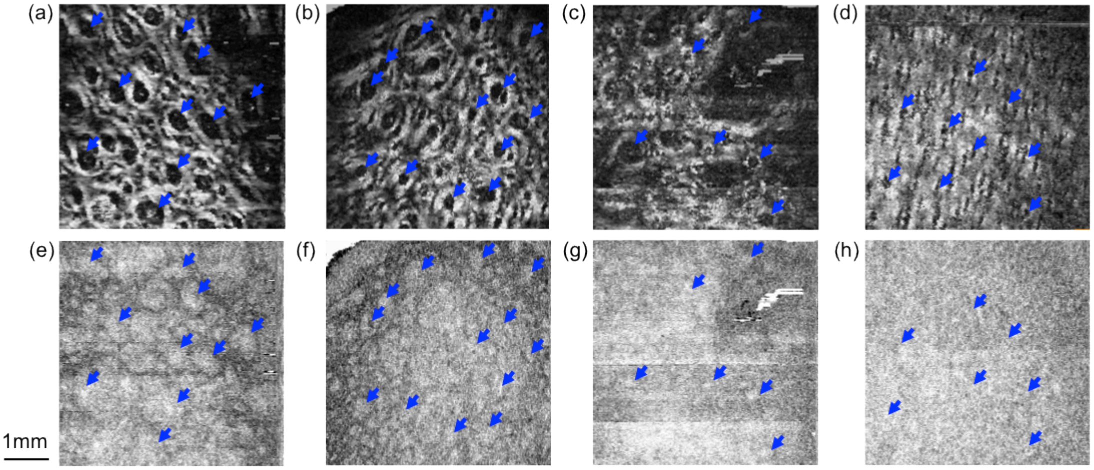

Figure 57. En face polarization (top) and intensity (bottom) images of cheek from young male (a,e), young female (b,f), old male (c,g), and old female (d,h) subjects.

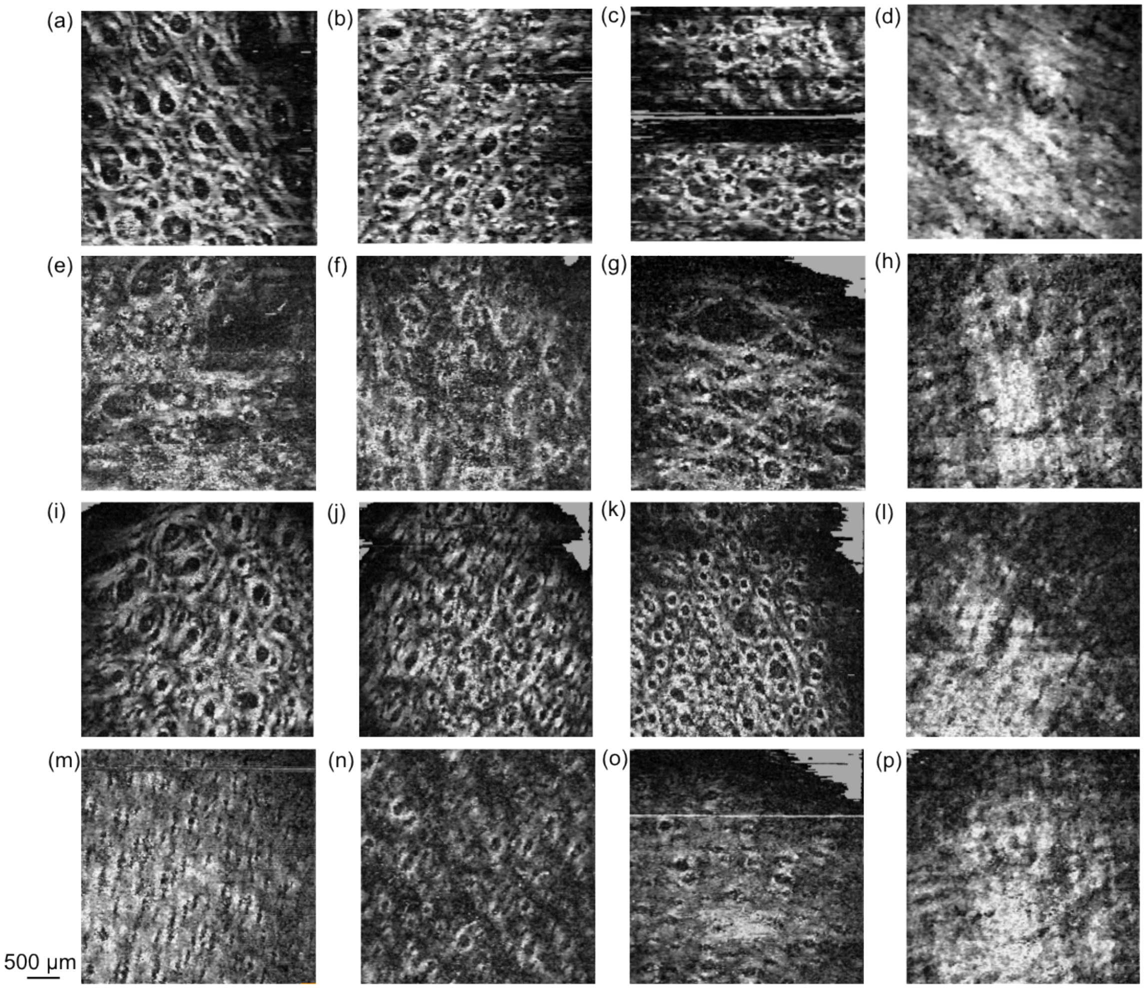

Figure 58. *En face* polarization images of a young male, old male, young female, and old female subjects from top down. From left to right, the imaging regions are cheek, temple, forehead and inner upper arm.

Figure 58 shows comparison of *en face* polarization images of a 23 year old male (a-d), a 60 year old male (e-h), a 28 year old female (i-l) and a 60 year old female (m-p). The imaging areas are cheek, temple, forehead and inner upper arm from left to right. The images from the sun exposed areas (cheek, temple, forehead) of both younger male and younger female showed similar pattern of birefringent tissues around non-birefringent follicles or holes. This kind of well-organized pattern is less evident in the polarization images of the older male and older female subjects which showed generally lower birefringence map. The inner upper arm images from all subjects showed similar homogeneously birefringent map.

Computation of volume birefringence

An averaged phase retardation slope was calculated from the volume of 2D images to quantify the skin birefringence. The accumulative phase retardation along depth is as a factor of tissue birefringence and depth. In other word, skin birefringence is proportional to the slope of phase retardation along depth. Firstly, a depth profile was obtained by averaging all the depth profiles within each 2D frame (Figure 59 (a)) from surface to depth. Additionally averaging 20 of these averaged depth profiles will result in a graph similar to Figure 59 (b). A phase retardation slope can be calculated by fitting the dermal layer with linear regression. Lastly a final phase retardation slope can be averaged through the whole volume.

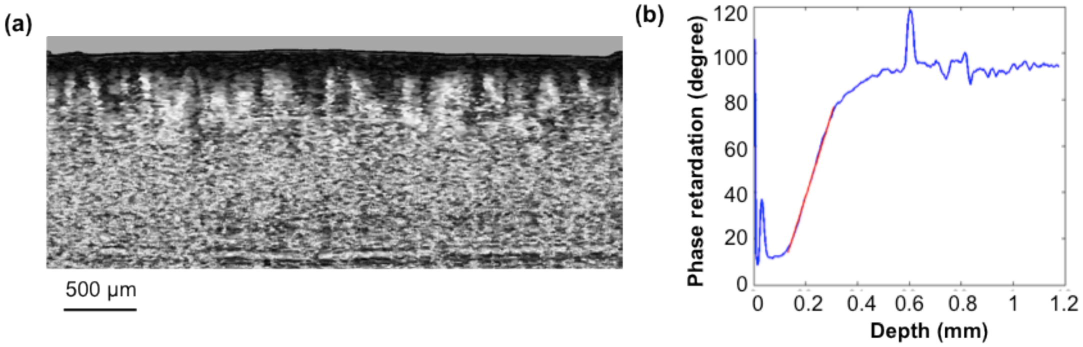

Figure 59. Computation of phase retardation slope from polarization image: (a) a representative 2D polarization image (b) averaged phase retardation depth profile with linear regression fit.

The same method was used to calculate the averaged phase retardation slope of each imaging volume acquired from all participating subjects. Figure 60 is a graph showing the mean volume birefringence value calculated from younger age group (n=33) and older age group (n=4). The averaged birefringence value of the younger group is significantly lower than that of older group ($p<0.05$) in all sun exposed areas (cheek, temple, forehead), while it is not significantly different at inner upper arm.

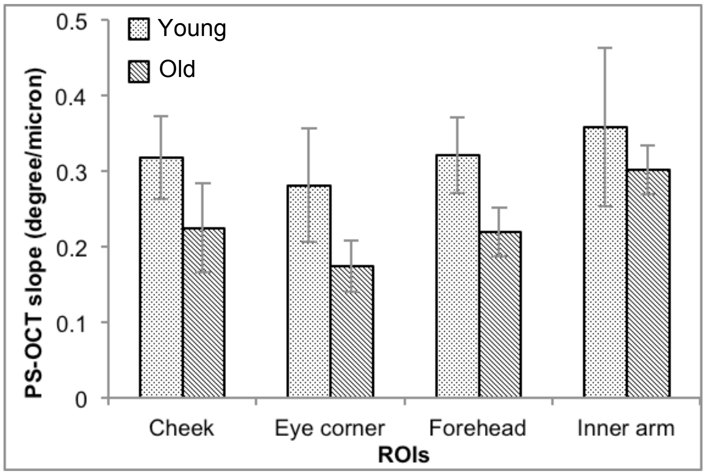

Figure 60. Volume birefringence of young and old age groups at the imaging regions of cheek, eye corner, forehead and inner upper arm.

The results were also compared between male and female for both younger age and older age groups. Figure 61 is a graph showing the averaged slope values of younger male and younger female groups at the four ROIs. Statistics analysis shows no significant difference between these two groups in all the imaging areas.

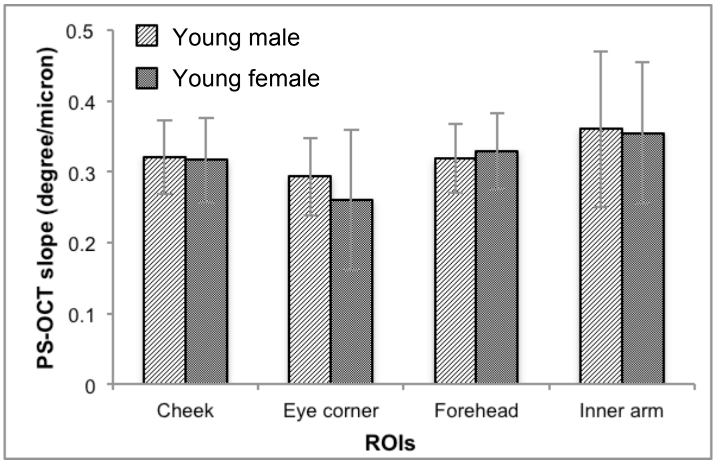

Figure 61. PS-OCT slope of comparing younger male and younger female subject groups at imaging regions of cheek, eye corner, forehead, and inner upper arm

Figure 62 showed the comparison between older male and older female groups in four ROIs. Statistics analysis shows no significant difference between the male and female groups. However, more number of volunteers need to be included into the older aged group for more statistically significant result and analysis.

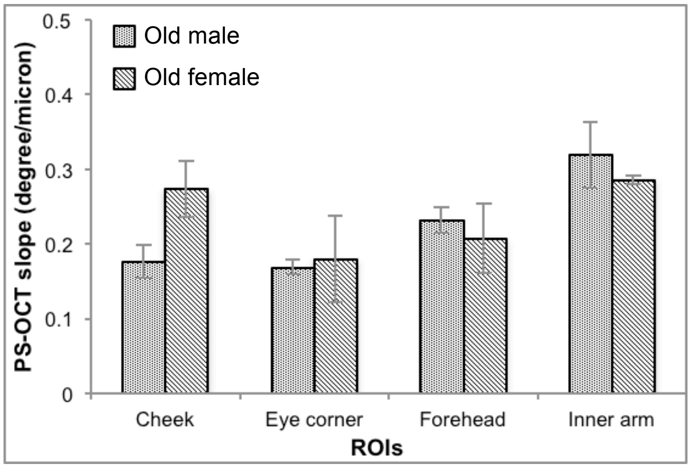

Figure 62. PS-OCT slope of comparing older male and older female subject group at imaging regions of cheek, eye corner, forehead, and inner upper arm

Discussions

Photo aging is the external aging in addition to intrinsic aging that accelerates the degeneration and loss of collagen thus causes wrinkles on the skin. PS-OCT was used to image younger human subjects (18-35) and older human subjects (>55) on the sun exposed areas (cheek, temple, forehead) and sun-protected area (inner upper arm). The results showed a significantly lower skin birefringence from older age group in the sun-exposed areas than that of younger age group. Statistics results showed no significant difference between the two genders within the same age groups. Sun exposure is shown as a significant factor of causing aging thus lower skin birefringence resulted from less amount and disarray of collagen. More volunteers in the older aged group need to be included to further examine the difference between male and female groups in older age, as well as the difference among skin types.

A further potential application of PS-OCT on skin aging study can be quantitative assessment of improvement on collagen content by skin care products. With the continuously increasing interest in the skin aging mechanism and higher expectation of slowing down this process, there have been lots of skin care products launched in the market. Many of them claim to be efficient in improving or promoting the generation of collagen tissue in older skins that are difficult to be quantified without seeing beneath the skin surface. PS-OCT can be potentially used for quantifying the skin collagen and elastin content or organization before and after the treatment.

Conclusion and future work

In this work, a real-time 4D multi-functional SD-OCT system that can simultaneously provide 2D and 3D intensity, polarization and flow images was presented. The axial resolution, lateral resolution, imaging depth, signal sensitivity drop-off, spectrometer efficiency, phase noise, polarization noise, system noise, computation of diattenuation, optic axis, and phase retardation were characterized.

A GPU card was added to the imaging system and CUDA C++ code was incorporated into the real-time acquisition and processing program. Data processing was speeded up by 5 times using our first GPU card NVIDIA Tesla C1060. Upgrading the GPU card to Tesla K20 and optimization on the computation code further increased the computation speed by another 20 times. This resulted in 100 times speed increase in the current hybrid GPU-CPU program. The efficient image processing speed of all intensity, polarization and flow images is 379 kHz, which is 8 times faster than cameras line acquisition rate of 45 kHz.

Furthermore, volume ray casting based on OpenGL was realized in the real-time data acquisition and processing program. Intensity, flow and polarization volume images were simultaneously rendered during data acquisition. This allows instantaneous visualization of the volume images in a real-time manner, which usually is performed by post-processing because of its heavy computation load. The volume update rate of all intensity, polarization and flow volumes is 2 volumes per second for volume size of 256 (X) x 64 (Y) x 256 (Z).

In addition to system work, two applications based on the system were initiated and described in this thesis. The first application was quantitative assessment of peripheral nerve injury by calculating the nerve birefringence from PS-OCT images. A longitudinal study was initiated to further improve the experiment results. The real-time data acquisition program was used for identifying the crush injury site labeled by micro-suture quickly and precisely. The PS-OCT results showed a lower birefringence in the nerve at two days post injury. The rat is still housed in UCR vivarium for longer time observation. More animal samples will be incorporated into this study.

The second application was using PS-OCT to study human skin photo aging by calculating skin birefringence from sun-exposed area (face) and sun-protected area (inner upper arm). From both the 2D and 3D *en face* polarization images, older volunteers showed less skin birefringence than younger volunteers. The skin birefringence value was quantified by calculating an averaged phase retardation slope from polarization volume images. The imaging results from older volunteers exhibit significantly lower skin birefringence than that of younger volunteers. Different gender groups in younger and older age were compared and no significant difference was observed in the same age groups. This study is being carried out and continued with more volunteers included into the study, especially for older volunteers with different skin types.

Future work on the system can include further increasing system speed by upgrading to the fastest cameras, higher power SLDs with broader bandwidth for higher SNR as well as better axial resolution. In terms of system application work, more number of rats with different levels of crush injuries should be studied in a longer time course. Histology analysis should be incorporated into this study for comparison purpose as well. The skin photo aging study also needs more older aged volunteers with all skin types.

References

1. Huang D, Swason EA, Lin CP et al. Optical coherence tomography. Science. 1991; 254(5035):1178–81.
2. Chang S, Mao Y, Flueraru C et al. Optical coherence tomography: technology and applications. Proc. SPIE. 2009; 7156:715606–1
3. Rajadhyaksha M, Grossman M, Esterowitz D et al. In vivo confocal scanning laser microscopy of human skin: melanin provides strong contrast. J Invest Dermatol. 1995; 104:946–52
4. Konig K, Riemann I. High-resolution multiphoton tomography of human skin with subcellular spatial resolution and picosecond time resolution. J Biomed Opt. 2003; 8:432–39.
5. Mitsui T. Dynamic range of optical reflectometry with spectral interferometry. Jap. J. of App. Phy. Part 1-Reg. Pap. Sho. Not. & Rev. Pap. 1999; 38: 6133–37.
6. Leitgeb R, Hitzenberger CK, Fercher AF. Performance of fourier domain vs. time domain optical coherence tomography. Opt. Exp. 2003; 11:889–94.
7. de Boer JF, Cense B, Park BH et al. Improved signal-to-noise ratio in spectral-domain compared with time-domain optical coherence tomography. Optics Letters. 2003; 28:2067–69.
8. Choma MA, Sarunic MV, Yang CH et al. Sensitivity advanrage of swept source and Fourier domain optical coherence tomography. Opt. Exp. 2003; 11:2183–89.
9. Yun S, Tearney G, de Boer J et al. High-speed optical frequency-domain imaging. Opt. Express. 2003; 11:2953-63.
10. Luo W, Marks DL, Ralston TS et al. Three-dimensional optical coherence tomography of the embryonic murine cardiovascular system. J. Biomed. Opt. 2006; 11(2):021014.
11. Chen Z, Milner TE, Dave D et al. Optical Doppler tomographic imaging of fluid flow velocity in highly scattering media. Optics Letters. 1997; 22(1):64–66.
12. Chen Z, Milner TE, Srinivas S et al. Noninvasive imaging of in vivo blood flow velocity using optical Doppler tomography. Optics Letters. 1997; 22(4):1119–21.
13. Ren H, Brecker KM, Ding Z et al. Imaging and quantifying transverse flow velocity with the Doppler bandwidth in a phase-resolved functional optical coherence tomography. Optics Letters. 2002; 27(6):409–11.
14. Izatt JA, Kulkarni MD, Yazdanfar S et al. In vivo bidirectional color Doppler flow imaging of picoliter blood volumes using optical coherence tomography. Optics Letters. 1997; 22(18):1439–41.
15. van Leeuwen TG, Kulkarni MD, Yazdanfar S et al. High-flow-velocity and shear-rate imaging by use of color Doppler optical coherence tomography. Optics Letters. 1999; 24(22):1584–86.

16. Nassif NA, Cense B, Park BH et al. In vivo high-resolution video-rate spectral-domain optical coherence tomography of the human retina and optic nerve. Opt. Express. 2004; 12(3):367–76.
17. Hee MR, Huang D, Swanson EA et al. Polarization-sensitive low-coherence reflectometer for birefringence characterization and ranging. J. Opt. Soc. Am. B. 1992; 9(6):903–9.
18. de Boer JF, Milner TE, van Gemert MJC et al. Two-dimensional birefringence imaging in biological tissue by polarization-sensitive optical coherence tomography. Optics Letters. 1997; 22(12):934–6.
19. de Boer JF, Milner TE, Nelson JS. Determination of the depth-resolved Stokes parameters of light backscattered from turbid media by use of polarization-sensitive optical coherence tomography. Optics Letters. 1999; 24(5):300–2.
20. Chen Y, Milner TE, Wang X et al. Optical Doppler tomography: imaging in vivo blood flow dynamics following pharmacological intervention and photodynamic therapy. Photochemistry and Photobiology. 1998; 67(1):56-60.
21. Jenkins MW, Peterson L, Gu S et al. Measuring hemodynamics in the developing heart tube with four-dimensional gated Doppler optical coherence tomography. Journal of Biomedical Optics. 2010; 15(6):066022.
22. Yasuno Y, Hong Y, Makita S et al. In vivo high-contrast imaging of deep posterior eye by 1-um swept source optical coherence tomography and scattering optical coherence tomography. Optics Express. 2007; 15(10): 6121-39.
23. Cense B, Chen TC, Park BH et al. Thickness and birefringence of healthy retinal nerve fiber layer tissue measured with polarization-sensitive optical coherence tomography. Investigative Ophthalmology and Visual Science. 2004; 45(8):2606-12.
24. Klein AM, Pierce MC, Zeitels SM et al. Imaging the human vocal folds in vivo with optical coherence tomography: a preliminary experience. Annals of Otology. 2006; 115(4):277-84.
25. Hee MR, Izatt JA, Swanson EA et al. Optical coherence tomography of the human retina. Arch. Ophthalmol. 1995; 113(3):325–32.
26. Goldsmith JA, Li Y, Chalita MR et al. Anterior chamber width measurement by high-speed optical coherence tomography. American Academy of Ophthalmology. 2005; 112(2):238–44.
27. Drexler W, Morgner U, Ghanta RK et al. Ultrahigh-resolution ophthalmic optical coherence tomography. Nat. Med. 2001; 7(4):502–7.
28. Wojtkowski M, Leitgeb R, Kowalczyk A et al. In vivo human retinal imaging by Fourier domain optical coherence tomography. J. Biomed. Opt. 2002; 7(3):457–63.
29. Swanson EA, Izatt IA, Hee MR et al. In vivo retinal imaging by optical coherence tomography. Optics Letters. 1993; 18(21):1864–6.

30. Wollstein G, Schuman J, Price LL et al. Optical coherence tomography macular and peripheral retinal nerve fiber layer measurements and automated visual fields. American Journal of Ophthalmology. 2004; 138(2):218–25.
31. Sanchez-Galeana C, Bowl C, Blumenthal EZ et al. Using optical imaging summary data to detect glaucoma. American Academy of Ophthalmology. 2001; 108(10):1812–8.
32. OCTnews org, companies developing OCT systems. http://www.octnews.org/articles/4111178/some-historical-statistics-on-companies-in-the-mar/
33. OCTnews org, ophthalmic OCT market size. http://www.octnews.org/articles/4176266/estimates-of-ophthalmic-oct-market-size-and-the-dr/
34. Markets report, optical imaging market. http://www.marketsandmarkets.com/Market-Reports/optical-imaging-technologies-market-894.html
35. Schaefer AW, Reynolds JJ, Marks DL et al. Real-time digital signal processing-based optical coherence tomography and Doppler optical coherence tomography. IEEE transactions on biomedical engineering. 2004; 51(1):186–90.
36. Jenkins MW, Chughtai SQ, Basavanhally AN et al. In vivo gated 4D imaging of the embryonic heart using optical coherence tomography. Journal of Biomed. Opt. 2007; 12(3):030505.
37. Ustun TE, Iftimia NV, Ferguson RD et al. Real-time processing for Fourier domain optical coherence tomography using a field programmable gate array. Rev. of Sci. Ins. 2008; 79:114301.
38. Desjardins AE, Vakoc BJ, Suter MJ et al. Real-time FPGA processing for high-speed optical frequency domain imaging. IEEE Tran. Med. Ima. 2009; 28:1468–72.
39. Watanabe Y, Itagaki T. Real-time display on Fourier domain optical coherence tomography system using a graphics processing unit. J. Bio. Opt. 2009; 14:060506.
40. der Jeught SV, Bradu A, Podoleanu AGh. Real-time resampling in Fourier domain optical coherence tomography using a graphics processing unit. J. Bio. Opt. 2010; 15:030511.
41. Zhang K, Kang JU. Real-time 4D signal processing and visualization using graphics processing unit on a regular nonlinear-k Fourier-domain OCT system. Opt. Exp. 2010; 18:11772–84.
42. Rasakanthan J, Sugden K, Tomlins PH. Processing and rendering of Fourier domain optical coherence tomography images at a line rate over 524 kHz using a graphics processing unit. J. Bio. Opt. 2011; 16:020505.
43. Choi D, Hiro-Oka H, Shimizu K et al. Spectral domain optical coherence tomography of multi-MHz A-scan rates at 1310nm range and real-time 4D-display up to 41 volumes/second. Biomed. Opt. Express. 2012; 3(12):3067–86.

44. Pierce MC, Park BH, Cense B et al. Simultaneous intensity, birefringence, and flow measurements with high-speed fiber-based optical coherence tomography. Optics Letters. 2002; 27:1534–36.
45. Park BH, Pierce MC, Cense B et al. Real-time multi-functional optical coherence tomography. Opt. Express. 2003; 11:782–93.
46. Park BH, Pierce MC, Cense B et al. Real-time fiber-based multi-functional spectral-domain optical coherence tomography at 1.3 μm. Opt. Express. 2005; 13:3913–44.
47. Tomlins PH, Wang RK. Theory, developments and applications of optical coherence tomography. Journal of Physics D: Applied Physics. 2005; 38:2519–35.
48. Hausler G, Lindner MW. Coherence radar and spectral radar-new tools for dermatological diagnosis. J. Biomed. Opt.1998; 3(1), 21.
49. Zhao Y, Chen Z, Saxer C et al. Phase-resolved optical coherence tomography and optical Doppler tomography for imaging blood flow in human skin with fast scanning speed and high velocity sensitivity. Optics. Letters. 2000; 25(2):114–6.
50. Zhao Y, Chen Z, Saxer C et al. Doppler standard deviation imaging for clinical monitoring of in vivo human skin blood flow. Optics. Letters. 2000; 25(18):1358–60.
51. Park BH. Fiber-based polarization-sensitive optical coherence tomography [Thesis]. Irvine: University of California, Irvine; 2005.
52. de Boer JF, Milner TE. Review of polarization sensitive optical coherence tomography and Stokes vector determination. Journal of Biomedical Optics. 2002; 7(3):359–71.
53. de Boer JF, Milner TE, van Gemert MJC et al. Two-dimensional birefringence imaging in biological tissue by polarization-sensitive optical coherence tomography. Optics Letters. 1997; 22(12):934–6.
54. de Boer JF, Srinivas SM, Malekafzali A et al. Imaging thermally damaged tissue by polarization sensitive optical coherence tomography. Optics Express. 1998; 3(6):212–8.
55. Park BH, Pierce MC, Cense B et al. Jones matrix analysis for a polarization-sensitive optical coherence tomography system using fiber-optic components. Optics Letters. 2004; 29(21):2512–4.
56. Park BH, Pierce MC, Cense B et al. Optic axis determination accuracy for fiber-based polarization-sensitive optical coherence tomography. Optics Letters. 2005; 30(19):2587–9.
57. Park BH, Saxer C, Srinivas SM et al. In vivo burn depth determination by high-speed fiber-based polarization sensitive optical coherence tomography. Journal of Biomedical Optics. 2001; 6(4):474–9.
58. Srinivas SM, de Boer JF, Park BH et al. Determination of burn depth by polarization-sensitive optical coherence tomography. Journal of Biomedical Optics. 2004; 9(1):207–12.

59. Cense B, Chen TC, Park BH et al. In vivo depth-resolved birefringence measurements of the human retinal nerve fiber layer by polarization-sensitive optical coherence tomography. Optics Letters. 2002; 27(18):1610–2.
60. Cense B, Chen TC, Park BH et al. In vivo birefringence and thickness measurements of the human retinal nerve fiber layer using polarization-sensitive optical coherence tomography. Journal of Biomedical Optics. 2004; 9(1):121–5.
61. Mujat M, Park BH, Cense B et al. Autocalibration of spectral-domain optical coherence tomography spectrometers for in vivo quantitative retinal nerve fiber layer birefringence determination. Journal of Biomedical Optics. 2007; 12(4):041205.
62. Fried D, Xie J, Shafi S et al. Imaging caries lesions and lesion progression with polarization sensitive optical coherence tomography. J. Biomed. Opt. 2002; 7(4):618–27.
63. Baumgartner A, Dichtl S, Hitzenberger CK et al. Polarization-sensitive optical coherence tomography of dental structures. Caries Res. 2000; 34(1):59–69.
64. Ren H, Ding Z, Zhao Y et al. Phase-resolved functional optical coherence tomography: simultaneous imaging of in situ tissue structure, blood flow velocity, standard deviation, birefringence, and Stokes vectors in human skin. Optics Letters. 2002; 27:1702–4.
65. Wang Y, Oh CM, Oliveira MC et al. GPU accelerated real-time multi-functional spectral-domain optical coherence tomography system at 1300 nm. Optics Express. 2012; 20(14):14797–813.
66. Drexler W, Fujimoto JG. Optical coherence tomography: technology and applications. Springer Berlin Heidelberg New York; 2008.
    Fingernail fold anatomy http://www8.georgetown.edu/dml/facs/graphics/POP-UPS/pop-upfingernail.html
67. Fischer E. Birefringence and ultrastructure of muscle. Ann. N. Y. Acad. Sci. 1947; 47(6 Art 6):783–97.
68. Cox RW. “Hibernoma”: The lipoma of immature adipose tissue. J. Pathol. Bacteriol. 1954; 68(2):511–8.
69. Islam MS, Oliveira MC, Wang Y et al. Extracting structural features of rat sciatic nerve using polarization-sensitive spectral domain optical coherence tomography. J. Biomed. Opt. 2012; 17(5): 056012.
70. An L, Li P, Shen T et al. High speed spectral domain optical coherence tomography for retinal imaging at 500,000 A-lines per second. Biomed. Opt. Exp. 2011; 2:2770–83.
71. Huang Y, Liu X, Kang J. Real-time 3D and 4D Fourier domain Doppler optical coherence tomography based on dual graphics processing units. Biomed. Opt. Exp. 2012; 3(9):2162–74.
72. Sylwestrzak M, Szlag D, Szkulmowski M et al. Four-dimensional structural and Doppler optical coherence tomography imaging on graphics processing units,” J. Biomed. Opt. 2012; 17(10):100502.

73. NVIDIA. NVIDIA CUDA Compute Unified Device Architecture Programming Guide Version 4.0. 2011.
74. NVIDIA. NVIDIA CUDA CUFFT Library Version 4.0. 2011.
75. Bonesi M, Churmakov DY, Ritchie LJ et al. Turbulence monitoring with Doppler optical coherence tomography. Laser Phys. Lett. 2007; 4:304–7.
76. Kaufman A, Mueller K. Overview of volume rendering. Center for Visual Computing, Computer Science Department, Stony Brook University.
77. Levoy M. Display of surfaces from volume data. IEEE Com. Gra. App. 1988; 8(3):29–37.
78. Marques R, Santos LP, Leskovsky P et al. GPU ray casting. Dep. Informatica, Universidade do Minho, VICOMTech.
79. Shreiner D, Woo M, Neider J et al. OpenGL Programming Guide, Fifth Edition. Addison-Wesley Professional; 2006.
80. NVIDIA. Getting Started With CUDA SKD Samples. 2012.
81. Kim KH, Pierce MC, Maguluri G et al. In vivo imaging of human burn injuries with polarization-sensitive optical coherence tomography. J. Biomed. Opt. 2012; 17(6):066012.
82. Seddon H. Three types of nerve injury. Brain. 1943; 66(4):237–88.
83. Stoll G, Griffin JW, Li CY et al. Wallerian degeneration in the peripheral nervous system: participation of both Schwann cells and macrophages in myelin degradation. Journal of Neurocytology. 1989; 18:671–83.
84. Frostick SP, Yin Q, Kemp GJ et al. Schwann cells, neurotrophic factors, and peripheral nerve regeneration. Microsurgery. 1998; 18:397–405.
85. Terenghi G. Peripheral nerve regeneration and neurotrophic factors. Journal of Anatomy. 1999; 194:1–14.
86. Lundborg G. A 25-year perspective of peripheral nerve surgery: evolving neuroscientific concepts and clinical significance. The Journal of Hand Surgery. 2000; 25A(3):391–414.
87. Spinner R. Surgery for peripheral nerve and brachial plexus injuries or other nerve lesions. Muscle Nerve. 2000; 23:680–95.
88. Robert EG, Happel LT, Kline DG. Intraoperative nerve action potential recordings: technical considerations, problems, and pitfalls. Neurosurgery. 2009; 65(4):A97–104.
89. Tasaki I. The electro-saltatory transmission of the nerve impulse and the effect of narcosis upon the nerve fiber. The American Journal of Physiology. 1939; 127(2):211-27.
90. Huxley AF, Stampfli R. Evidence for Saltatory Conduction in Peripheral Myelinated Nerve Fibres. J Physiol. 1949; 108:315–39.
91. Laule C, Vavasour IM, Kolind SH et al. Magnetic Resonance Imaging of Myelin. The American Society for Experimental Neuro Therapeutics. 2007; 4:460–84.
92. Garbay B, Heape AM, Sargueil F et al. Myelin synthesis in the peripheral nervouse system. Progress in Neurobiology. 2000; 61:267–304.

93. Pouly S, Antel JP. Multiple sclerosis and central nervous system demyelination. Journal of Autoimmunity. 1999; 13:297–306.
94. Fraher J. A quantitative study of anterior root fibres during early myelination. Journal of Anatomy. 1972; 112(1):99–124.
95. Bruck W. The role of macrophages in Wallerian degeneration. Brain Pathology. 1997; 7:741–52.
96. Wang H, Fu Y, Zickmund P et al. Coherent anti-stokes raman scattering imaging of axonal myelin in live spinal tissues. Biophysical Journal. 2005; 89:581–91.
97. Wang Y, Wu C, Caprariello A et al. In vivo quantification of myelin changes in the vertibrate nervous system. The Journal of Neuroscience. 2009; 29(46):14663–9.
98. Hare GM, Evans PJ, Mackinnon SE et al. Walking track analysis: a long-term assessment of peripheral nerve recovery. Plast. Reconst. Surg. 1992; 89(2):251–8.
99. Gilchrest BA. A review of skin ageing and its medical therapy. British Journal of Dermatology. 1996; 135:867–75.
100. Kohl E, Steinbauer J, Landthaler M et al. Skin ageing. Journal of the European Academy of Dermatology and Venereology. 2011; 25:873–84.
101. Kligman AM, Lavker RM. Cutaneous aging: the differences between intrinsic aging and photoaging. J. Cutan. Aging. Cos. Dermatol. 1988; 1:5–12.
102. Bhawan J, Andersen W, Lee J et al. Photoaging versus intrinsic aging: a morphologic assessment of facial skin. J. Cutan. Pathol. 1995; 22:154–9.
103. Fisher GJ, Kang S, Varani J et al. Mechanisms of photoaging and chronological skin aging. Arch Dermatol. 2002; 138:1462–70.
104. Trautinger F. Mechanisms of photodamage of the skin and its functional consequences for skin ageing. Clinical and Experimental Dermatology. 2001; 26:573–7.
105. Uitto J. Biochemistry of the elastic fibers in normal connective tissues and its alterations in disease. J. Invest. Dermat. 1979; 72:1–10.
106. Tzaphlidou M. The role of collagen and elastin in aged skin: an image processing approach. Micron. 2004; 35:173–7.
107. Chung JH, Seo JY, Choi HR et al. Modulation of skin collagen metabolism in aged and photoaged human skin in vivo. J. Invest. Dermatol. 2001; 117:1218–24.
108. Vogt M, Knuttel A, Hoffmann K et al. Comparison of high frequency ultrasound and optical coherence tomography as modalities for high resolution and non invasive skin imaging. Biomed. Tech. 2003; 48:116–21.
109. Welzel J. Optical coherence tomography in dermatology: a review. Skin Res. Technol. 2001; 7:1–9.
110. Pierce MC, Strasswimmer J, Park BH et al. Advances in optical coherence tomography imaging for dermatology. J. Invest. Dermatol. 2004; 123:458–63.

111. Oh JT, Lee SW, Kim YS et al. Quantification of the wound healing using polarization-sensitive optical coherence tomography. J. Biomed. Opt. 2006; 11:041124.
112. Sakai S, Yamanari M, Miyazawa A et al. In vivo Three-dimensional birefringence analysis shows collagen differences between young and old photo-aged human skin. J. Invest. Dermatol. 2008; 128: 1641–7.
113. Gambichler T, Matip R, Moussa G et al. In vivo data of epidermal thickness evaluated by optical coherence tomography: effects of age, gender, skin type, and anatomic site. J. Dermat. Sci. 2006; 44:145–52.
114. Fenske NA, Lober CW. Structural and functional changes of normal aging skin. J Am Acad Dermatol 1986; 15(4, pt1):571–85.